Science Advances
AAAS

Supplementary Materials for

Amphotericin B assembles into seven-molecule ion channels: An NMR and molecular dynamics study

Yuichi Umegawa *et al.*

Corresponding author: Michio Murata, murata@chem.sci.osaka-u.ac.jp; Wataru Shinoda, shinoda@okayama-u.ac.jp

Sci. Adv. **8**, eabo2658 (2022)
DOI: 10.1126/sciadv.abo2658

The PDF file includes:

- Figs. S1 to S47
- Tables S1 to S12
- Legends for videos S1 to S5
- References

Other Supplementary Material for this manuscript includes the following:

- Videos S1 to S5

Additional Materials and Methods

Initial structure of AmB

Table S1. The *xyz* coordinate of the initial structure of AmB the RMSD calculation to construct AmB assembly based on NMR-derived distance constraints

position	x	y	z	position	x	y	z	position	x	y	z
C1	1.809	-0.935	-8.737	C6'	9.528	-4.158	8.36	H22	4.337	-2.007	2.563
C2	1.539	-0.122	-7.497	O(C1)	1.977	-2.107	-8.761	H23	6.78	-0.605	1.392
C3	1.8	-0.916	-6.246	O3	0.826	-1.993	-6.168	H24	4.578	-2.365	0.127
C4	1.568	-0.082	-4.983	O5	1.545	-2.075	-3.562	H25	6.783	-0.603	-1.079
C5	2.047	-0.761	-3.704	O8	0	0	0	H26	4.79	-2.589	-2.347
C6	1.638	0.047	-2.482	O9	1.895	-2.039	1.303	H27	6.736	-0.527	-3.51
C7	2.044	-0.622	-1.174	O11	1.837	-1.968	3.996	H28	4.919	-2.615	-4.866
C8	1.427	0.024	0.051	O13	1.376	-1.827	6.624	H29	6.624	-0.312	-5.933
C9	1.939	-0.601	1.336	O15	1.166	0.973	9.876	H30	4.975	-2.515	-7.319
C10	1.249	-0.053	2.582	O17	3.058	-0.213	6.405	H31	6.52	-0.092	-8.407
C11	1.874	-0.525	3.894	O19	5.34	-2.873	6.897	H32	4.939	-2.344	-9.778
C12	1.128	0.044	5.089	O35	3.454	-0.799	-13.924	H33	6.125	0.269	-10.836
C13	1.663	-0.444	6.439	O37	1.808	-0.173	-9.819	H34	4.691	-2.093	-12.174
C14	1.038	0.311	7.593	Oa(C41)	4.434	0.854	10.768	H35	4.546	0.727	-13.26
C15	1.745	0.073	8.925	Ob(C41)	4.061	-1.28	10.332	H36	3.429	1.094	-11.124
C16	3.257	0.309	8.755	O2'	5.437	-5.564	7.427	H37	2.956	-1.618	-10.926
C17	3.74	-0.582	7.611	O4'	8.268	-5.736	10.505	H38a	0.638	-2.19	-11.191
C18	5.226	-0.469	7.309	O5'	7.328	-3.467	7.791	H38b	0.311	-0.617	-11.956
C19	5.743	-1.583	6.376	N3'	5.482	-6.46	10.039	H38c	1.381	-1.792	-12.759
C20	5.181	-1.586	4.989	H2a	2.186	0.755	-7.489	H39a	1.291	1.669	-11.684
C21	5.809	-1.202	3.878	H2b	0.496	0.196	-7.49	H39b	2.579	2.219	-12.782
C22	5.293	-1.504	2.559	H3	2.855	-1.188	-6.202	H39c	1.511	0.879	-13.263
C23	5.89	-1.218	1.403	H4a	2.103	0.864	-5.068	H40a	5.944	-1.474	-14.183
C24	5.416	-1.684	0.115	H4b	0.502	0.113	-4.867	H40b	6.788	-0.206	-13.263
C25	5.966	-1.309	-1.065	H5	3.13	-0.877	-3.736	H40c	7.011	-1.917	-12.828
C26	5.526	-1.799	-2.345	H6a	2.115	1.027	-2.518	H1'	5.905	-2.607	8.925
C27	5.994	-1.312	-3.511	H6b	0.555	0.171	-2.472	H2'	4.266	-4.449	8.735
C28	5.578	-1.76	-4.831	H7b	1.73	-1.666	-1.187	H3'	5.942	-4.511	10.541
C29	5.97	-1.17	-5.967	H7a	3.127	-0.571	-1.06	H4'	7.653	-6.061	8.556
C30	5.568	-1.613	-7.285	H8	1.594	1.101	0.017	H5'	8.107	-3.28	9.69
C31	5.891	-0.97	-8.437	H9	3.025	-0.516	1.375	H6'a	9.909	-3.195	8.022
C32	5.44	-1.387	-9.743	H10a	1.298	1.036	2.575	H6'b	10.157	-4.534	9.168
C33	5.603	-0.676	-10.866	H10b	0.206	-0.369	2.59	H6'c	9.542	-4.866	7.531
C34	5.107	-1.087	-12.226	H11	2.911	-0.195	3.942	H3OH	0.899	-2.341	-5.278
C35	4.05	-0.128	-12.801	H12a	1.207	1.132	5.083	H5OH	1.755	-2.385	-2.692
C36	2.986	0.358	-11.794	H12b	0.078	-0.243	5.033	H8OH	-0.255	-0.893	0.191
C37	2.264	-0.79	-11.076	H14a	1.074	1.382	7.39	H9OH	1.895	-2.307	2.227
C38	1.063	-1.389	-11.797	H14b	0	0	7.712	H11OH	1.763	-2.161	4.933
C39	2.024	1.351	-12.425	H15	1.549	-0.945	9.264	H13OH	1.547	-2.031	7.533
C40	6.299	-1.177	-13.196	H16	3.44	1.365	8.557	H15OH	1.757	1.03	10.621
C41	3.991	0	10.056	H17	3.499	-1.611	7.876	H35OH	2.883	-0.193	-14.371
C1'	5.945	-3.297	8.082	H18a	5.394	0.503	6.844	H2'OH	5.372	-5.044	6.627
C2'	5.312	-4.612	8.477	H18b	5.758	-0.513	8.259	H4'OH	9.196	-5.672	10.311
C3'	6.056	-5.181	9.689	H19	6.824	-1.454	6.331	HNHa	6.103	-6.913	10.693
C4'	7.532	-5.321	9.346	H20	4.163	-1.943	4.937	HNHb	4.554	-6.323	10.412
C5'	8.097	-3.992	8.865	H21	6.733	-0.646	3.945	HNHc	5.425	-6.961	9.161

Methods of molecular dynamics (MD) simulations

(A) Amphotericin B (AmB)

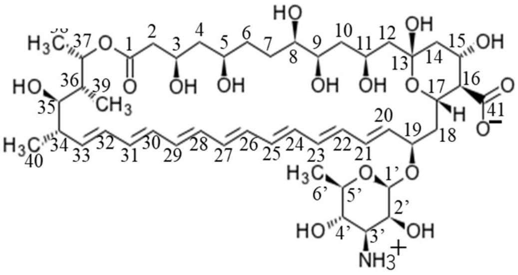

(B) Methyl Ester derivative (AME)

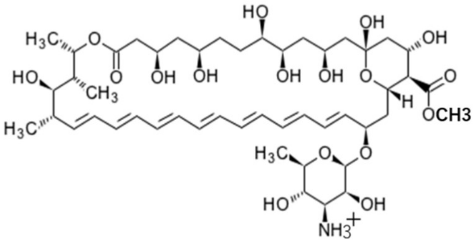

(C) N-acetyl-AmB derivative (AmB-NHCOCH$_3$)

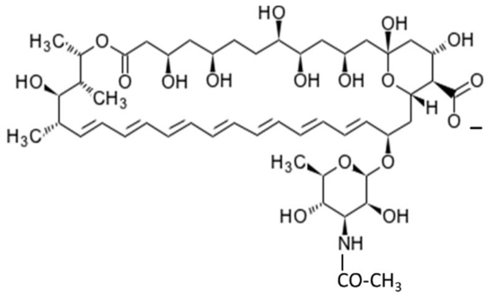

(D) Ergosterol (Erg)

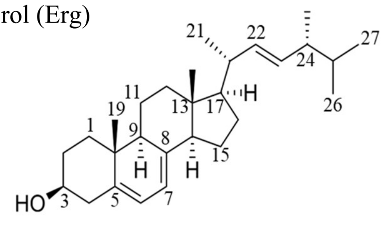

(E) Cholesterol (Cho)

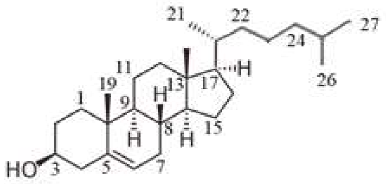

(F) POPC

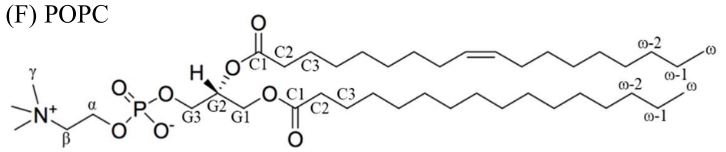

(G) DPhPC

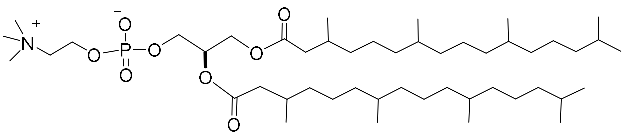

Fig. S1. Chemical structure of (A) Amphotericin B (AmB), (B) Methyl Ester derivative (AME), (C) N-acetyl-AmB derivative (AmB-NHCOCH$_3$), (D) Ergosterol (Erg), (E) Cholesterol (Cho), (F) POPC, and (G) DPhPC.

Table S2. The number of molecules contained in the simulated systems and the simulation times are listed. Ion channels consisting of AmB and Erg are embedded in a POPC or 1,2-diphytanoyl-sn-glycero-3-phosphocholine (DPhPC) lipid bilayer. The system indices, V, VI, VII and VIII, represent the numbers of AmB in a channel made by AmB_5(V), AmB_6(VI), AmB_7(VII), and AmB_8(VIII), respectively.

System ID	AmB	Sterols	Lipids	Water	KCl concentration (mol/liter)	Time (μs) MD with no electric field	Time (μs) MD under electric field
V	5	5 Erg	16 POPC	~2000	0.15	10	0
VI-1	6	6 Erg	16 POPC	~2000	0.15	10	0
VII-1	7	7 Erg	16 POPC	~2000	0.15	10	0
VII-2	7	7 Cho	16 POPC	~2000	0	10	0
VIII-1	8	8 Erg	32 POPC	~4000	0.15	10	0
VII-3	7 (A)	7 Erg	16 POPC	~2000	0.15	10	10
VII-4	7 (B)	7 Erg	16 POPC	~2000	0.15	10	0
VII-5	63	189 Erg	450 POPC	39744	0	4	0
VII-6	112	224 Erg	512 POPC	66592	0	2	0
VI-2	6	103 Erg	192 DPhPC	~14500	2	1	10
VII-7	7	103 Erg	192 DPhPC	~14500	2	1.6	16
VIII-2	8	103 Erg	192 DPhPC	~14500	2	1	10
VII-8	7	7 Erg	64 POPC	~6000	0	10	0
VII-9	7	7 Erg	32 POPC	~4000	0	10	0
VII-10	7	7 Erg	16 POPC	~2000	0	10	0
VIII-3	16	48 Erg	112 POPC	~8500	0	2	0

(A) AmB derivatives as shown in Fig.S1B, (B) AmB derivatives as shown in Fig.S1C.

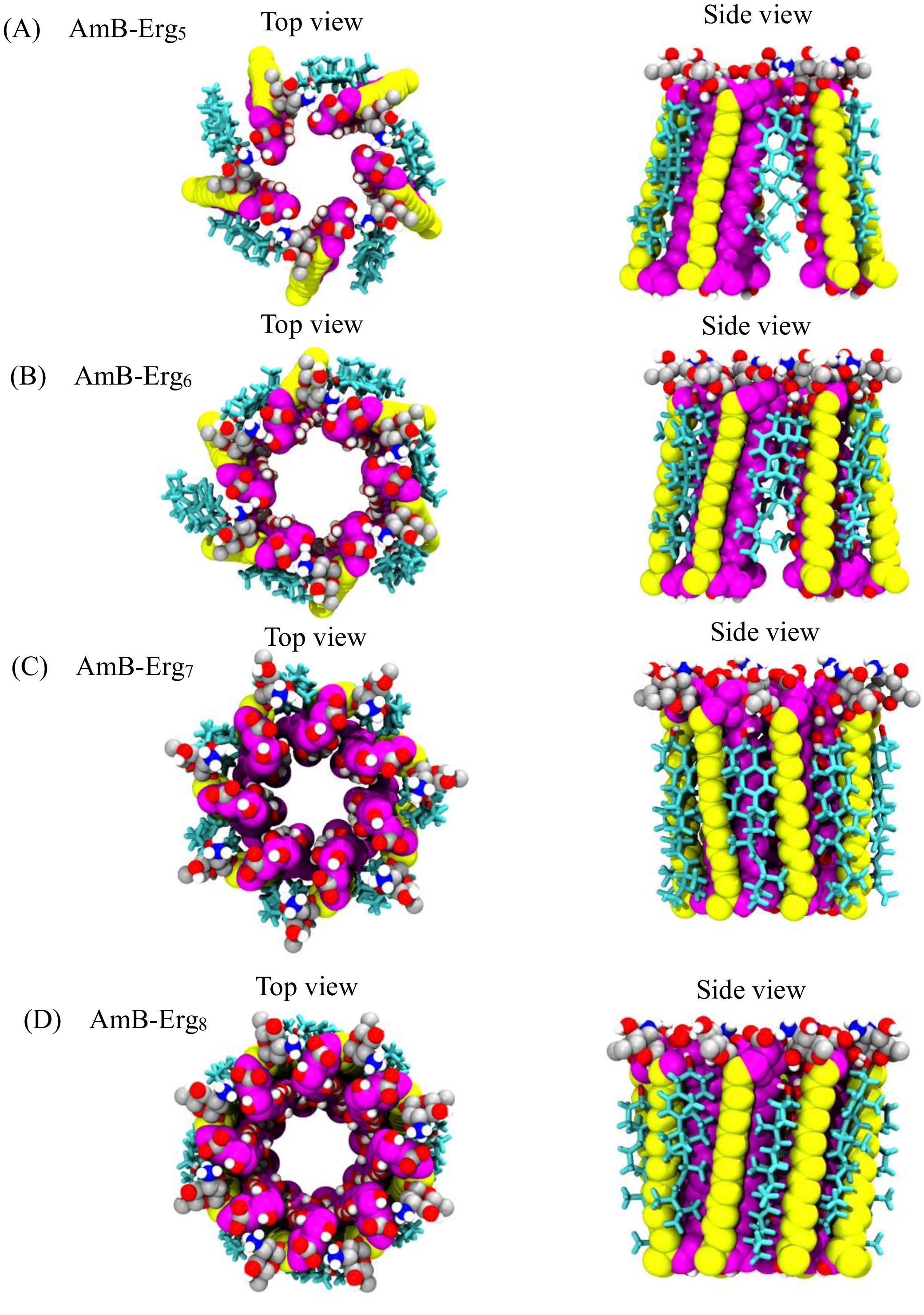

Fig. S2. Constructed AmB-Erg complex channel structures for (A) AmB-Erg$_5$, (B) AmB-Erg$_6$, (C) AmB-Erg$_7$, and (D) AmB-Erg$_8$. The color code is as follows; the carbons in the polyene part of AmB: yellow, polyhydroxy carbons: magenta, oxygen atoms: red, hydrogen atoms: white, carbon atoms of the mycosamine group and carboxylate group: silver, and nitrogen atom: blue. Erg is shown in a cyan wire model with a red oxygen atom on C3.

(A) System-V(AmB_5-Erg_5)

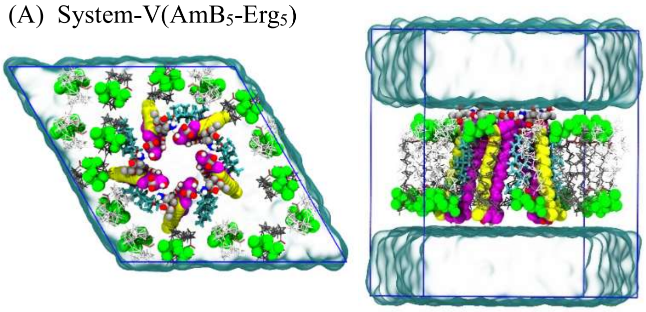

(B) System-VI-1(AmB_6-Erg_6)

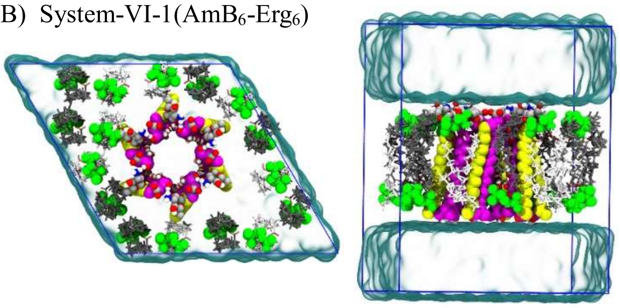

(C) System-VII-1 (AmB_7-Erg_7)

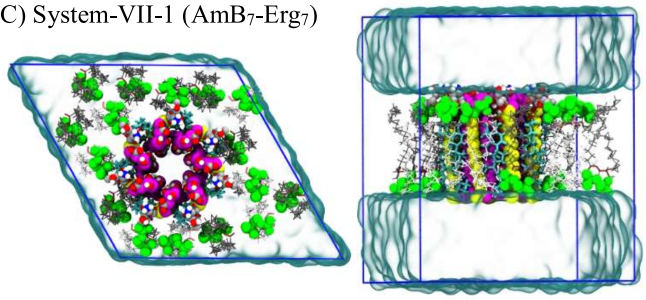

(D) System-VII-2(AmB_7-Cho_7)

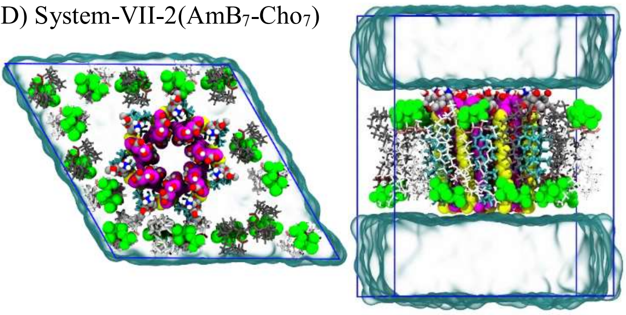

(E) System-VIII-1 (AmB_8-Erg_8)

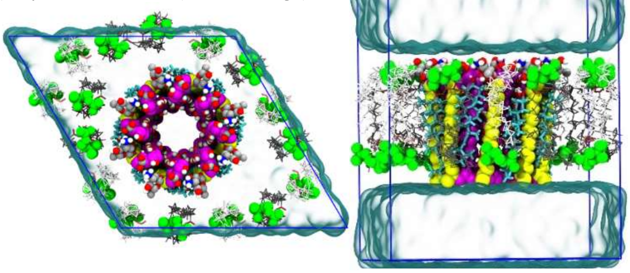

(F) System-VII-3 (AME)

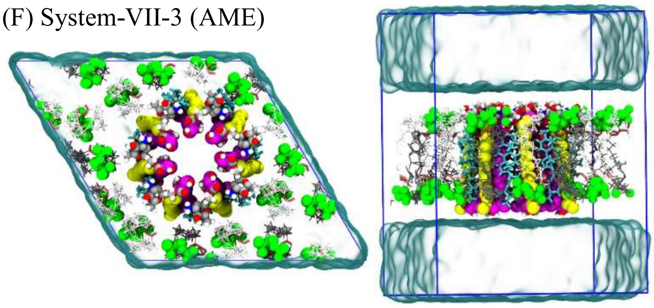

(G) System-VII-4(AmB-$NHCOCH_3$)

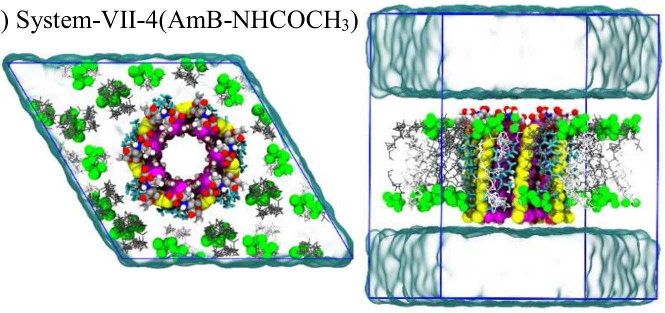

Fig. S3. The initial structures of (A) System-V, (B) System-VI-1, (C) System-VII-1, (D) System-VII-2, (E) System-VIII-1, (F) System-VII-3, and (G) System-VII-4. The color codes for AmB and Erg are the same as in Fig. S2. Headgroups of phospholipid molecules are shown in green, acyl chains of lipids in the upper leaflet are given in gray and in the lower leaflet in white. Transparent volume represents water region.

(A) System-VI-2

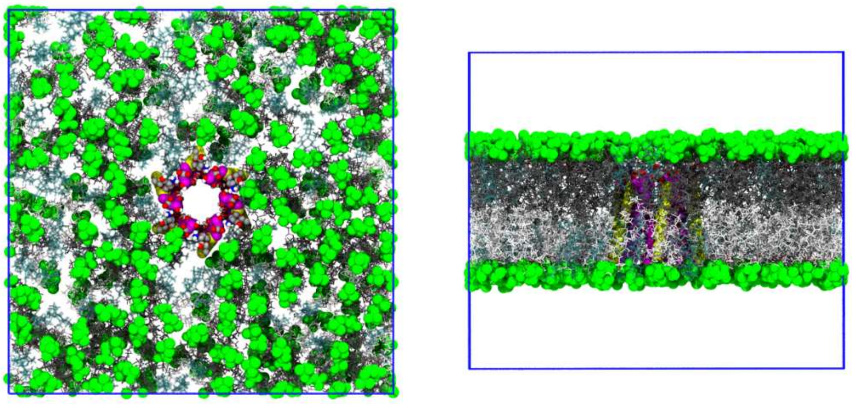

(B) System-VII-7

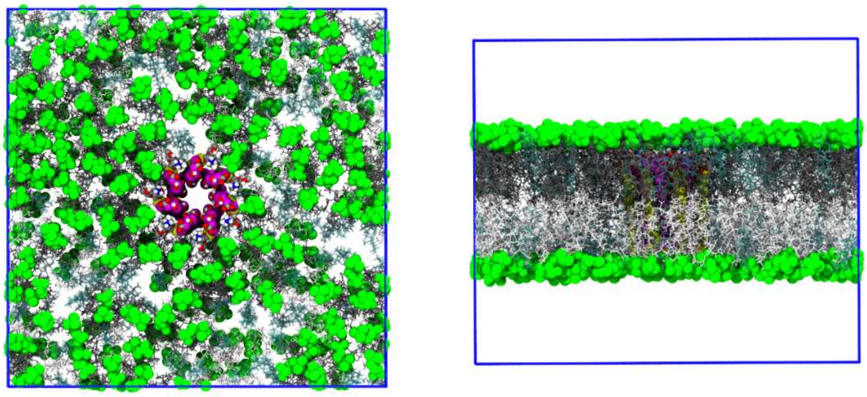

(C) System-VIII-2

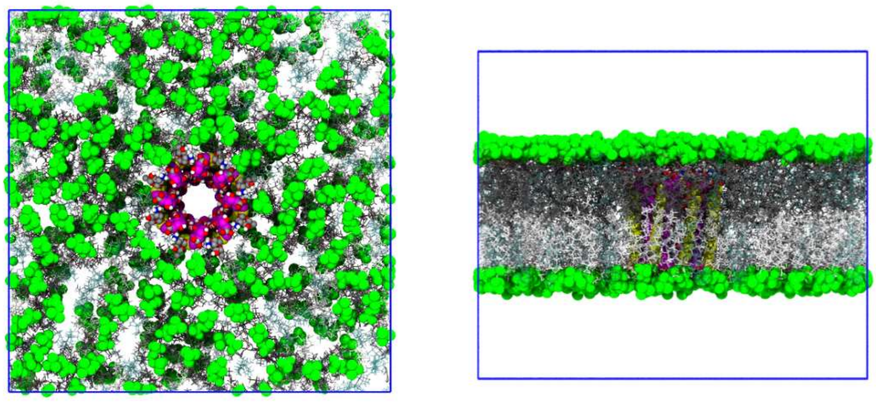

Fig. S4. Initial structure of (A) the System-VI-2, (B) the System-VII-7, and (C) and the System-VIII-2. The color code of AmB/Erg and the presentation are the same as in Fig. S2. Water is not shown for clarity.

Simulation Details

All MD simulations were performed using the GROMACS software package (version 5.1.4)(*51*). Lipids and sterols were modelled with the CHARMM 36 force field (*52, 53*). Parameters of AmB were derived from CGenFF using CGenFF web server (*54-57*), except for the torsion potential of polyene moiety in AmB. We observed that the parameters automatically determined by CGenFF web server tends to give rise to a *cis* conformation in polyene moiety. Thus, we adopted the torsion parameters of polyene moiety from butadiene in the CHARMM 36 FF, which stabilizes *trans* conformation. The TIP3P model was used for water molecules (*58*). The temperature and pressure were set to 310 K and 1 bar, respectively. Nosé-Hoover thermostat (*59, 60*) and Parrinello-Rahman barostat (*61*) were used to control the temperature and pressure, respectively. A semi-isotropic coupling scheme was employed to independently control the pressure of the triclinic simulation box in parallel and normal to the bilayer. Electrostatic interactions were calculated with the particle mesh Ewald method (*62, 63*). Lennard Jones interaction was truncated by applying force switching cutoff in the range of 1.0−1.2 nm. The LINCS algorithm (*64*) was used to constraint all bonds involving hydrogen atoms. A time step of 2 fs was used. Initially, we performed 20 ns MD simulation to relax lipid configuration with a position restraint to an AmB channel. After removing the position restraint, 1 μs equilibration and 10 μs-long production runs were carried out for the System-V, System-VI-1, System-VII-1~4, 8~10, and System-VIII-1 in the NPT ensemble. In the case of system-VIII-3, we have performed 2-μs production runs.

For the System-VII-7, we generated 16 different initial configurations, and we repeatedly performed 100 ns equilibration and 1 μs production MD runs for each system under an applied electric field (E_{applied}) of 0.01 Volt/nm along the bilayer normal (+z-axis) (*65*). In the case of the System-VI-2 and System-VIII-2, started from 10 different initial configurations, we again repeatedly carried out 100 ns equilibration and 1μs production MD runs under E_{applied} of 0.01 V/nm along the +z-axis. For the System-VII-3, 10 different initial structures are generated by replacing water molecules by ions to produce 1 M σalt concentration, and each initial structure was equilibrated for 100 ns and 1 μs production run was carried out in the presence of E_{applied} of 0.01 V/nm.

We investigated the distribution of multiple AmB channels within POPC bilayer. We prepared the system with nine AmB channels embedded in the lipid membrane composed of 450 POPC molecules, which satisfied the present experimental molar ratio (AmB/Erg/POPC, 1: 3: 7) (System-VII-5). We have carried out an MD simulation of the System-VII-5 for 4 μs.

We also examined the aggregation of AmB channels, which were disposed in parallel and anti-parallel arrangements in POPC membrane. We performed 1 μs MD simulations of 4 AmB channels with antiparallel arrangement (Fig. S32). We took final configuration of 4 AmB channels after 1μs and replicated it into *x-y* direction (2 × 2) using GROMACS tool "genconf" and constructed 16 AmB channels with parallel and anti-parallel arrangement and generated the initial configuration for the System-VII-6. The System-VII-6 is composed of 112 AmB, 512 POPC and 224 Erg molecules (Fig. S5). We performed 2 μs production run for the System-VII-6 (Fig. S44).

Top view

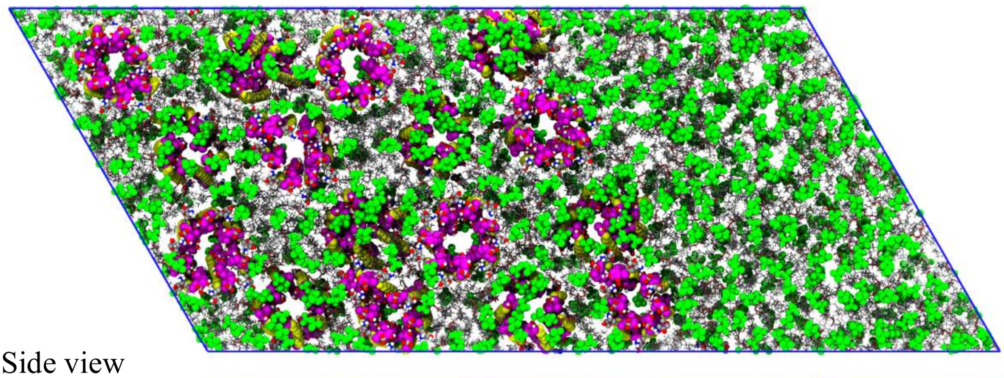

Side view

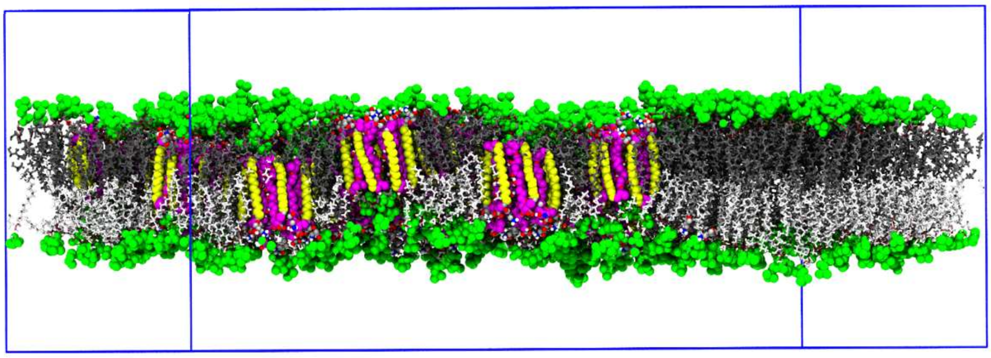

Fig. S5. Initial structure of the System-VII-6. The color code and the presentation are the same as in Figs. S2 and S3. Water is not shown for clarity.

Analysis Method for pore radius profile

For the analysis of the pore radius of AmB channel, we used the HOLE program (*66*). To count the number of ions passing through the channel, we define the passing ion (K^+ and Cl^-) that goes through the two *xy*-planes at the minimum *z*-height of C2 and at the maximum *z*-height of C10 of AmB molecules continuously. The schematic diagram of ions passing through AmB channel is shown in Fig. S6.

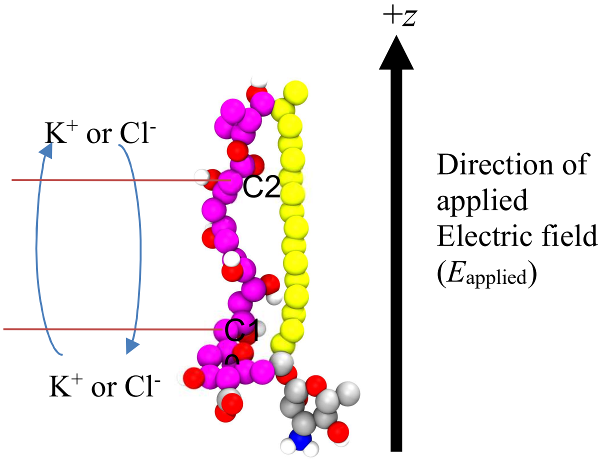

Fig. S6. The scheme to count the number of ions passing through the AmB channel. The color code is as follows; the carbons in the polyene part of AmB: yellow, polyhydroxy carbons: magenta, oxygen atoms: red, hydrogen atoms: white, carbon atoms of mycosamine group and carboxylate group: silver, and nitrogen atom: blue.

Conductance calculations

We studied the ion permeation through the AmB channel in lipid bilayer under a constant applied electric field along the bilayer normal (z) (*65, 67–69*). For charged segments (with the charge of q_i), the additional force, $F_{z,i} = q_i E$, was exerted owing to the applied electric field. Although an applied voltage (V_a) can be computed by $V_a = E\langle L_z \rangle$, where $\langle L_z \rangle$ is the average box length along the z axis, the effective voltage difference is different from V_a. The electrostatic potential across the AmB channel, $V(z)$, was calculated by solving Poisson's equation. Ionic current (I_total) was estimated by counting the number of K^+ and Cl^- ions crossing the AmB channel, using the in-house FORTRAN code (available on request).

The conductance (G) of AmB channel is calculated by using following equation (*65, 67–69*), which is based on accumulated ion crossing number ($N_\mathrm{K/Cl}$) for each ion and Ohm's law,

$$\Delta V = V\left(-\frac{L_z}{2}\right) - V\left(\frac{L_z}{2}\right), \tag{1}$$

$$G = \frac{I_\mathrm{total}}{\Delta V} = \frac{(N_\mathrm{K} - N_\mathrm{Cl})\, q}{\Delta V \tau}, \tag{2}$$

where I_{total} is the total current and q is the charge of a monovalent ion. With N_K and N_Cl in the given time interval, τ, we can calculate the average current carried by each ion. ΔV is the electrostatic potential difference across the AmB channel.

Preparations of labeled AmBs

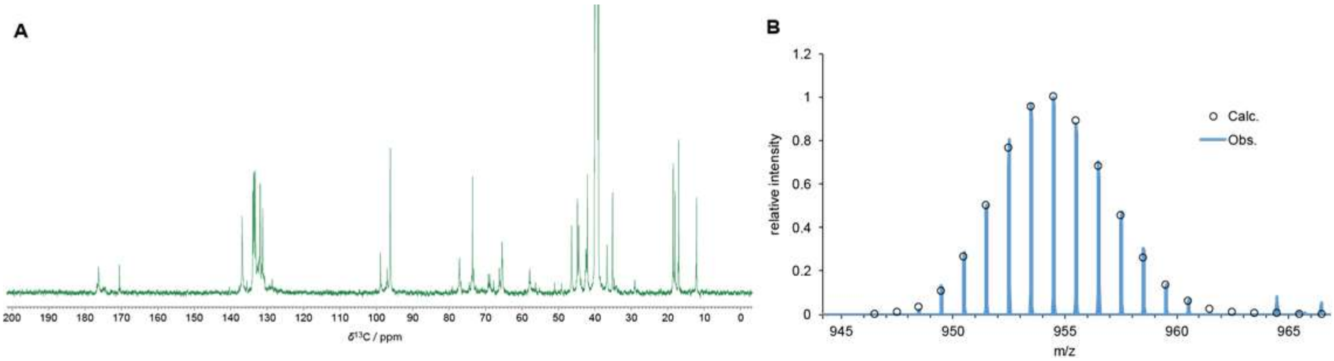

Fig. S7. Solution ^{13}C NMR spectrum in DMSO-d_6 (A) and ESI mass spectrum (B) of skipped-^{13}C-AmB. Based on the biosynthetic route of AmB, ^{13}C labeling at the labeled positions and ^{13}C scrambling to non-labeled positions were calculated to 30% and 6%, respectively (open circle).

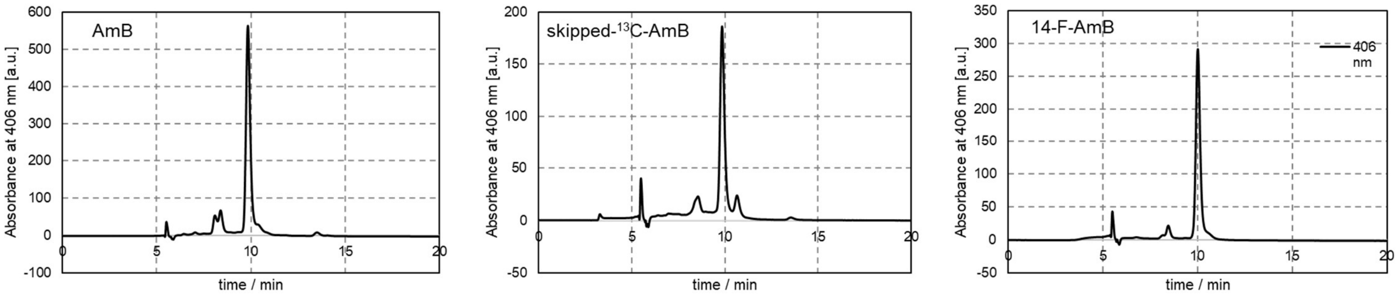

Fig. S8. HPLC chromatograms of AmB, skipped ^{13}C-AmB and 14-F AmB
AmB: Commercially available from Nacalai Tesque (Kyoto, Japan).
HPLC Column: COSMOSIL Packed Column 5C$_{18}$-MS-II, 4.6 mmID x 250 mm (Nacalai Tesque, Inc.). Flow rate: 0.5 mL/min. Eluent: 80% of MeOH and 20% of 3 mM AcONH4 aq. (pH 4.8), isocratic. Temp.: 40°C.

Synthesis of 26, 40-$^{13}C_2$-AmB.

26, 40-$^{13}C_2$-AmB was prepared according to Scheme S1 below.

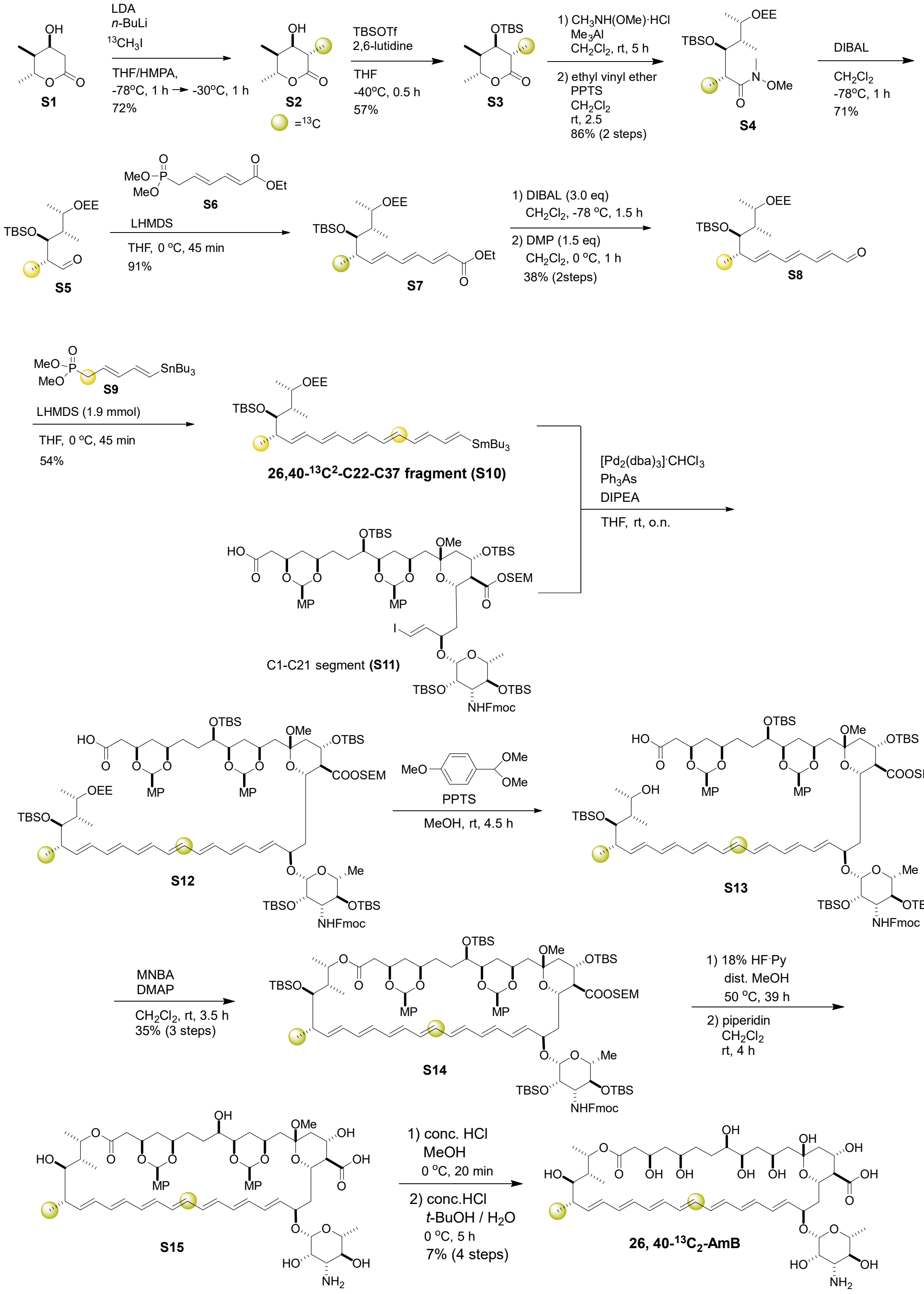

Scheme S1 Preparation of 26, 40-$^{13}C_2$-AmB.

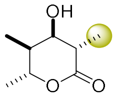

S2

Conversion of S1 to S2. To THF (50 ml) cooled to −78 °C., *n*-BuLi (1.6 M, 33 ml) and diisopurpilmin (7.4 ml, 52 mmol) were added, and the mixture was stirred for 30 minutes. THF (20 ml) and lactone **S1** dissolved in HMPA (20 ml) were slowly added to it with a cannula. After stirring for 30 minutes, *n*-BuLi (1.6 M, 26 ml) was added and the mixture was further stirred for 45 minutes, then $^{13}CH_3I$ (4.0 ml, 62.4 mmol) was slowly added, and the temperature was raised to −30 °C over 1 hour. After stirring for another 2 hours, the reaction was quenched by the addition of acetic acid (15 ml) dissolved in THF (15 ml). After extraction with dichloromethane, the organic layer was washed with water and saturated brine, and dried over sodium sulfate. After distilling off the solvent, the obtained residue was purified by silica gel chromatography (hexane / AcOEt, 4: 1) to give ^{13}C-lactone **S2** (2.1 g, 72%) as a white solid.

R_f = 0.15 (hexane/AcOEt, 2/1); ^1H NMR (500 MHz, $CDCl_3$) δ 4.44 (1H, dq, J = 10.5, 7.0 Hz, H37), 3.71 (1H, dd, J = 3.5, 2.5 Hz, H35), 2.68-2.62 (1H, m, H34), 1.82 (1H, dqd, J = 10.0, 4.0, 3.5 Hz, H36), 1.43 (1.5H, d, J = 6.5 Hz, H40), 1.34 (3H, d, J = 6.5 Hz, H38), 1.18 (1.5H, d, J = 7.0 Hz, H40), 1.04 (3H, d, J = 6.5 Hz, H39); ^{13}C NMR (125 MHz, $CDCl_3$) δ 175.04, 72.73, 43.51, 43.16, 36.87, 26.43, 22.39, 19.42, 15.78, 12.56; MS (ESI) *m*/*z* calcd for $C_7{}^{13}CH_{14}NaO_3$ [M+Na$^+$] 182.0874, found: 182.0872.

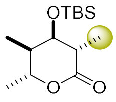

S3

Conversion of S2 to S3. ^{13}C-lactone **S2** (2.0 g, 12.6 mmol) was dissolved in THF (50 ml) and cooled to −40 °C, followed by 2,6-lutidine (2.9 ml, 25.2 mmol) and TBSOTf (. 4.4 ml, 18.9 mmol) was added slowly. After stirring for 30 minutes, the reaction was quenched with saturated aqueous sodium hydrogen carbonate solution. After extraction with dichloromethane, the organic layer was dried over sodium sulfate and the solvent was retained. The obtained residue was purified by silica gel chromatography (hexane / AcOEt, 1: 0 → 10: 1) to obtain TBS ether **S3** (2.0 g, 57%) as colorless crystals.

R_f = 0.87 (silica gel, 1:1-ethyl acetate/hexane); ^1H NMR (500MHz, $CDCl_3$) δ 4.43 (1H, dq, J = 9.5, 6.0 Hz, H37), 3.62 (1H, dd, J = 3.0, 2.0 Hz, H35), 2.62 (1H, qd, J = 8, 3.0 Hz, H34), 1.79 (1H, dqd, J = 12.0, 7.0, 2.5 Hz, H36), 1.37 (1.5H, d, J = 7.5 Hz, H40), 1.32 (3H, d, J = 6.5 Hz, H38), 1.11 (1.5H, d, J = 7.5 Hz, H40), 0.96 (3H, d, J = 7.0 Hz, H39), 0.85 (9H, s, *t*-Bu-Si), 0.04 (6H, s, Me-Si); ^{13}C NMR (125 MHz, $CDCl_3$) δ 174.30, 74.53, 44.34, 44.04, 36.15, 27.07, 25.78, 24.20, 19.93, 16.62, 13.98, −4.42, −4.75; MS (ESI) *m*/*z* calcd for $C_{13}{}^{13}CH_{28}NaO_3Si$ [M+Na$^+$] 296.1739, found: 296.1736.

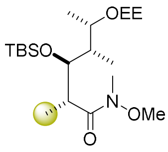

S4

Conversion of S3 to S4. $CH_3NH(OMe) \cdot HCl$ (3.4 g, 34.8 mmol) was dissolved in dichloromethane (40 ml) and cooled to 0 °C. A hexane solution of trimethylaluminum (1.0 M, 45.2 mmol) was slowly added thereto with a dropping funnel. After stirring for 30 minutes, TBS ether **S3** (1.9 g, 6.95 mmol) dissolved in dichloromethane (30 ml) was slowly added with a dropping funnel. After stirring at room temperature for 5 hours, the mixture was cooled to 0 ° C again, saturated aqueous sodium potassium tartrate solution was added, and the mixture was further stirred for 5 hours. Then, the mixture was extracted with ethyl acetate, and the organic layer was dried over sodium sulfate. The solvent was removed, and the resulting residue was dried under vacuum and then dissolved in dichloromethane (70 ml). Ethyl vinyl ether (13.4 ml, 140 mmol) and PPTS (874 mg, 3.48 mmol) were added thereto at room temperature, and the mixture was stirred for 2.5 hours and quenched with saturated aqueous sodium hydrogen carbonate solution. After extraction with dichloromethane, the organic layer was washed with saturated brine and dried over sodium sulfate. The residue obtained by retaining the solvent was purified by silica gel chromatography (hexane / AcOEt, 5: 1) to obtain Weinrebamide **S4** (2.3 g, 86% for 2 steps) as a colorless oil.

R_f = 0.63 (silica gel, 1:2-ethyl acetate/hexane); ^{1}H NMR (500MHz, $CDCl_3$) δ 4.67 (0.5H, q, *J* = 5.0, H37), 4.63 (0.5H, q, *J* = 5.0 Hz, H34), 3.95-3.90 (1.5H, m, H35, H37), 3.78-3.74 (0.5H, m, H37), 3.68 (1.5H, s, N-OMe), 3.67 (1.5H, s, N-OMe), 3.58-3.52 (0.5H, m, EE), 3.47-3.36 (1.5H, m, EE), 3.18-3.12 (3.5H, m, N-Me, H34), 3.05 (0.5H, dq, *J* = 12.5, 5.5 Hz, H34), 1.92-1.89 (0.5H, m, H36), 1.77-1.71 (0.5H, m, H36), 1.26 (3H, d, *J* = 5.5 Hz, EE), 1.22 (1.5H, t, *J* = 7 Hz, H40), 1.16 (3H, t, *J* = 7.0 Hz, EE), 1.11 (1.5H, d, *J* = 6.0 Hz, H38), 1.03 (1.5H, d, *J* = 7.0 Hz, H38), 0.96 (1.5H, d, *J* = 7.5 Hz, H40), 0.89-0.87 (10.5H, m, H39, *t*-Bu-Si), 0.86 (1.5H, d, *J* = 1.5 Hz, H39), 0.04 (6H, m, Me-Si); ^{13}C NMR (125 MHz, $CDCl_3$) δ 177.83, 99.89, 98.79, 59.67, 43.13 26.26, 26.24, 20.71, 18.42, 16.53, 15.38, 15.34, 15.26, 13.88, 13.55, 12.63, 12.06, -3.67,-4.01, -4.05; MS (ESI) *m*/*z* calcd for $C_{19}{}^{13}CH_{43}NNaO_5Si$ [M+Na$^+$] 429.2842, found: 429.2832

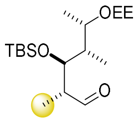

S5

Conversion of S4 to S5. Weinrebamide **S4** (2.3 g, 5.8 mmol) was dissolved in dichloromethane (60 ml) and cooled to −78 °C. DIBAL (1.0 M, 17.4 ml) was slowly added thereto, and the mixture was stirred for 1 hour, then a saturated aqueous sodium potassium tartrate solution was added, and the mixture was stirred for 5 hours. After extraction with ethyl acetate, the organic layer was dried over sodium sulfate and the solvent was retained. The obtained residue was purified by silica gel chromatography (hexane / AcOEt, 1: 0 → 5: 1) to obtain aldehyde **S5** (1.4 g, 71%) as a colorless oil.

R_f = 0.59 (silica gel, 1:5-ethyl acetate/hexane); ^{1}H NMR (500 MHz, $CDCl_3$) δ 9.69 (1H, dd, *J* = 1.5, 1.5 Hz, CHO), 4.64 (1H, qd, *J* = 5.0, 5.5 Hz, EE), 4.26-4.23 (0.5H, m, H35), 4.16-4.13 (0.5H, m, H35), 3.88-3.81 (1H, m, H37), 3.61-3.52 (1H, m, EE), 3.47-3.39 (1H, m, EE), 2.55-2.52 (0.5H, m, H34), 2.48-2.44 (0.5H, m, H34), 1.98-1.93 (0.5H, m, H36), 1.91-1.87 (0.5H, m, H36), 1.26-1.23 (4.5H, m, H40, EE), 1.18-1.15 (3H, m, EE), 1.12 (1.5H, d, *J* = 6.5 Hz, H38), 1.06 (1.5H, d, *J* = 6.5 Hz, H38), 1.00 (1.5H, dd, *J* = 9.0, 6.5 Hz, H40), 0.87-0.83 (12H, m, H39, *t*-Bu-Si), 0.04 (3H, s, Me-Si), -0.04 (3H, s, Me-Si) ; MS (ESI) *m*/*z* calcd for $C_{17}{}^{13}CH_{38}NaO_4Si$ [M+Na$^+$] 370.2471, found: 370.2496.

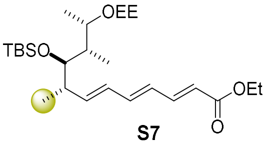

S7

Conversion of **S5** to **S7**. After dimethyl phosphonate **S6** (*70*) (1.6 g, 4.0 mmol) was dissolved in THF (20 ml) and cooled to 0 °C, LHMDS (1.0 M, 6.4 ml) was added, and the mixture was stirred for 10 minutes. Then, aldehyde **S5** (1.4 g, 4.0 mmol) dissolved in THF (20 ml) was slowly added dropwise, and the mixture was stirred for 1 hour. The reaction was quenched with saturated aqueous ammonium chloride solution and then extracted with ethyl acetate. The organic layer was dried over sodium sulfate, and the solvent was distilled off. The obtained residue was purified by silica gel chromatography (hexane / AcOEt 1: 0 → 30: 1) to obtain triene **S7** (1.7 g, 91%) as a colorless oil.

R$_f$ = 0.70 (hexane/AcOEt, 4/1); ^{1}H NMR (400 MHz, CDCl$_3$) δ 9.69 (1H, dd, *J*= 11.2, 15.2, H29), 6.52 (1H, dd, *J*= 10.5, 14.9, H31), 6.23 (1H, ddd, *J*= 14.8, 11.2, 3.4 Hz, H30), 6.11 (1H, dd, *J*= 15.3, 10.5 Hz, H32), 6.0 (1H, m, H33), 5.84 (1H, d, *J*= 15.2 Hz, H28), 4.65 (1H, q, *J*= 5.0 Hz, EE), 4.20 (2H, q, *J*= 7.1 Hz, -OEt), 3.92 (1H, m, H37), 3.38-3.65 (3H, m, H35, EE), 2.50 (1H, m, H34), 1.93 (1H, m, H36), 1.86 (1H, m, H36), 1.32-1.24 (6H, m, -OEt, EE), 1.18 (4.5H, m, H40, EE), 1.08 (1.5H, d, *J*= 6.4 Hz, H38), 1.00 (1.5H, d, *J*= 6.4 Hz, H38), 0.85 (1.5H, m, H40), 0.83 (3H, m, H39), 0.87-0.83 (12H, s, *t*-Bu-Si), 0.04 (3H, s, Me-Si), -0.04 (3H, s, Me-Si); ^{13}C NMR (100 MHz, CDCl$_3$) δ 167.16, 144.70, 144.64, 144.33, 128.86, 128.77, 128.32, 128.16, 98.88, 98.26, 77.47, 77.21, 72.72, 71.39, 60.93, 60.21, 60.02, 53.40, 42.69, 41.90, 40.52 40.42, 40.17, 40.06, 26.23, 26.13, 21.05, 20.88, 18.55, 18.34, 16.76, 16.66, 16.23, 16.09, 15.92, 15.80, 15.69, 15.35, 14.31, 13.89, 13.84, 13.72, 11.60, 11.49, -3.64, -3.70, -3.93; MS (ESI) *m*/*z* calcd for $C_{25}{}^{13}CH_{48}NaO_5Si$ [M+Na$^+$] 492.3202, found: 492.3199.

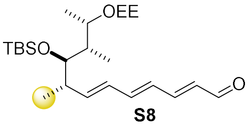

S8

Conversion of S7 to S8. Triene **S7** (1.0 g, 2.1 mmol) was dissolved in dichloromethane, cooled to -78 ºC, and DIBAL (1.0 M, 8.5 mmol) was added slowly. After stirring for 1.5 hours, the reaction was quenched with saturated aqueous sodium potassium tartrate solution, and the mixture was further stirred for 4 hours. After extraction with ethyl acetate, the organic layer was washed with saturated brine and dried over sodium sulfate. After distilling off the solvent, the resulting residue was dried under vacuum and used in the next reaction. Crude alcohol was dissolved in dichloromethane (21 mL) and Dess-Martin reagent (1.4 g, 3.2 mmol) was added at 0 ºC. After stirring at room temperature for 1 hour, the reaction was quenched with saturated sodium thiosulfate. After extraction with ethyl acetate, the organic layer was washed with saturated brine and dried over sodium sulfate. After the solvent was retained, purification was performed by silica gel chromatography (hexane / AcOEt, 1: 0 → 15: 1) to obtain trienal **S8** (345 mg, 38% for 2 steps) as a colorless oil.

R$_f$ = 0.55 (hexane/AcOEt, 4/1); ^{1}H NMR (500 MHz, CDCl$_3$) δ 9.53 (1H, d, *J*= 8.9, CHO), 7.11 (1H, dd, *J*= 13,3, 13,2), 6.23 (1H, dd, *J*= 10.0 Hz, 15.2), 6.35 (1H, m), 6.18-6.02 (2H, m), 6.40 (2H, m, EE), 3.90 (1H, m, H37), 3.62-3.39 (3H, m, H35, EE), 2.51 (1H, m, H34), 1.91 (0.5H, m, H36), 1.84 (1H, m, H36), 1.25 (3H, m, EE), 1.16 (4.5H, m, EE, H40), 1.06 (1.5H, dd, *J*= 6.2, 2.3 Hz, H38), 1.00 (1.5H, dd, *J*= 6.2, 2.3 Hz, H38), 0.92-0.81 (13.5H, m, tBu-Si, H40, H39), 20.12 (3H, s, Me-Si), -15.38 (3H, s, Me-Si); ^{13}C NMR (125 MHz, CDCl$_3$) δ 193.45, 152.28, 152.19, 151.96, 146.60, 146.25, 143.25, 143.12, 142.94, 130.76, 130.67, 128.72, 128.62, 128.27, 128.11, 99.17, 98.73, 98.13, 73.45, 72.54, 71.31, 60.81, 59.84, 59.72, 42.73, 41.81, 40.57, 40.44, 40.30, 40.15, 31.50, 26.12, 26.06, 26.02, 22.57, 20.96, 20.76, 20.70, 20.18, 20.06, 18.68, 18.43, 18.31, 17.19, 16.47, 16.16, 16.08, 15.89, 15.75, 15.65, 15.51, 15.28, 14.93, 13.74, 13.63, 13.57, 11.31, 10.58, 10.39, 8.86, -3.70, -3.79, -4.00; MS (ESI) *m/z* calcd for $C_{23}{}^{13}CH_{44}NaO_4Si$ [M+Na$^+$] 448.2940, found: 448.2939.

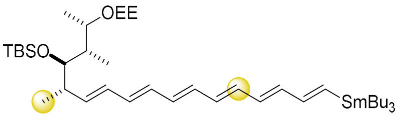

S10

Conversion of S8 to S10. ^{13}C-dimethyl phosphonate **S9** (*71*) (1.1 g, 2.36 mmol) was dissolved in THF (24 ml) and cooled to 0 °C. LHMDS (1.0 m, 1.2 mmol) was added thereto, and the mixture was stirred for 10 minutes. Then, trienal **S8** (500 mg, 1.2 mmol) dissolved in THF (5 ml) was added, and the mixture was stirred for 45 minutes. Then, saturated aqueous ammonium chloride solution was added to stop the reaction, and the mixture was extracted with diethyl ether. The organic layer was washed with saturated brine and dried over sodium sulfate. The solvent was distilled off and the obtained residue was purified by Florisil column chromatography (hexane / AcOEt 1: 0 → 30: 1) to obtain C22-C37 segment **S10** (505 mg, 54%) as a yellow oil.

R_f = 0.65 (hexane/AcOEt, 10/1); ^{1}H NMR (400 MHz, $CDCl_3$) δ 6.20-6.30 (10H, m, H21-H31), 6.06 (1H, m, H32), 5.77 (1H, m, H33), 4.66 (1H, m, EE), 3.95 (1H, m, 37), 3.68-3.57 (1H, m, EE), 3.50-3.39 (2H, H35, EE), 2.46 (1H, m, H34), 1.95 (0.5H, m, H36), 1.86 (0.5H, m, H36), 1.58-1.43 (6H, m, *n*-Bu-Sn), 1.37-1.25 (15H,m, *n*-Bu-Sn, EE), 1.22-1.16 (4.5H, m, EE, H40), 1.08 (1.5H, d, *J*= 6.4 Hz, H39), 1.02 (1.5H, d, *J*= 6.4 Hz, H39), 0.94-0.81 (22.5H, m, tBu-Si, *n*-Bu-Sn, H38, H40), 0.04 (3H, s, Me-Si), 0.01 (3H, s, Me-Si); ^{13}C NMR (100 MHz, $CDCl_3$) δ 146.93, 135.91, 135.65, 133.65, 133.51, 133.41, 133.30, 133.30, 133.14, 132.87, 132.82, 132.72, 132.66, 132.45, 132.40, 132.16, 129.35 129.30, 128.05, 127.99, 98.89, 98.31, 77.71, 77.60, 72.83, 71.42, 60.93, 60.05, 42.42, 41.81, 40.01, 31.57, 29.08, 27.82, 27.27, 26.99, 26.15, 21.08, 20.93, 18.45, 18.40, 16.19, 15.85, 16.62, 15.34, 13.99, 13.69, 12.70, 11.70, 11.44, 11.23, 10.57, 10.47, 10.35, 9.53, -3.62, -3.75, -3.89. -3.95; MS (ESI) *m/z* calcd for $C_{39}{}^{13}C_2H_{76}NaO_3SiSn$ [M+Na+] 789.4550, found: 789.4559.

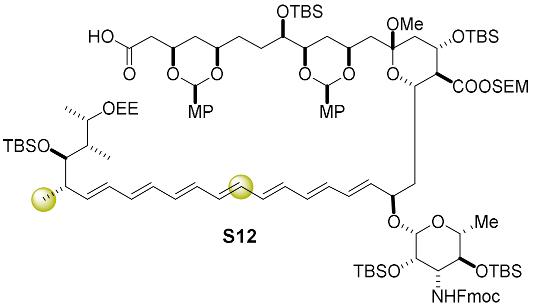

S12

Conversion of S10 to S12. The C1-C21 segment **S11**[18] (552 mg, 0.32 mmol) dehydrated by toluene azeotrope, the C22-C37 segment **S10** (505 mg, 0.66 mmol) and diisopropylethylamine (0.58 ml, 3.2 mmol) were dissolved in THF (25 ml). A solution of trisdibenzylideneacetone dipalladium (99 mg, 96 µmol) and triphenylarsane (97 mg, 0.28 mmol) in THF (32 mL) weighed in the glove box was added thereto at 0 ° C. The temperature was raised to room temperature and the mixture was stirred overnight. After that, THF was distilled off under reduced pressure, and the residue was crudely purified by silica gel column chromatography (ethyl acetate / hexane, 1:5, chloroform / methanol, 1: 10—1: 20, 1% triethylamine), and the coupling product **S12** (453). mg, impure) was obtained.

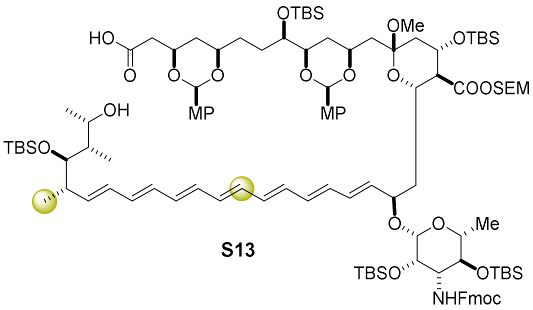

S13

Conversion of S12 to S13. Compound **S12** (450 mg) was dissolved in methanol (21 ml) and *p*-methoxybenzaldehyde dimethyl acetal (3.6 ml), PPTS (1.4 g, 6.3 mmol) was added, and the mixture was stirred at room temperature in the dark for 4.5 hours. The reaction was stopped with saturated aqueous sodium hydrogen carbonate solution, and the mixture was extracted with ether. After drying over anhydrous sodium sulfate, the solvent was evaporated under reduced pressure. The residue was crudely purified by silica gel column chromatography (ethyl acetate / hexane, 1: 5, chloroform / methanol, 1: 10—1: 20, 1% triethylamine) to give a yellow amorphous solid of secoic acid **S13** (499 mg, impure).

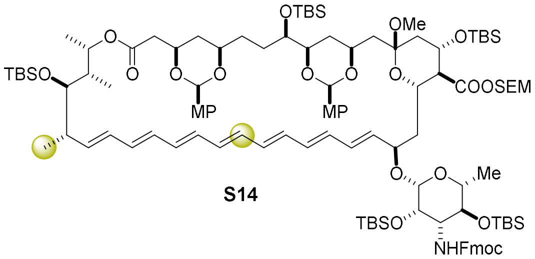

S14

Conversion of S13 to S14. Secoic acid **S13** (499 mg) was dissolved in dichloromethane (50 ml), and a solution of 2-methyl-6-nitrobenzoic acid anhydride (475 mg, 1.4 mmol), which was weighed in a glove box, and DMAP (337 mg, 2.8 mmol) in dichloromethane (190 ml) was added dropwise over an hour and a half. After stirring at room temperature for another 2 hours, the reaction was stopped with saturated aqueous sodium hydrogen carbonate solution, and the mixture was extracted with ether. After drying over anhydrous magnesium sulfate, the solvent was distilled off under reduced pressure. The residue was purified by silica gel column chromatography (ethyl acetate / hexane, 0: 1—1: 10, methanol / chloroform, 0: 1-1: 20) and macrolactone **S14** (171 mg, 35% for 3 steps) was obtained as an amorphous solid.
R_f = 0.52 (hexane/AcOEt, 4/1); ^{1}H NMR (400 MHz, $CDCl_3$) δ 7.75 (2H, d, *J*= 7.5 Hz, Fmoc), 7.59 (2H, m, Fmoc), 7.37-7.32 (6H, m, Fmoc, MP), 7.27 (2H, t, *J*= 7.5 Hz, Fmoc), 6.81 (4H, dd, *J*= 20.5, 8.5 Hz, MP), 6.43 (0.5H, m, H26), 6.22-6.01 (11.5H, m, H21-32), 5.73 (1H, dd, *J*= 14.5, 6.6 Hz, H20), 5.54 (1H, dd, *J*= 14.8, 9.2 Hz, 33H), 5.44 (1H, s, 3,5-MP acetal), 5.39 (1H, s, 9, 11-MP acetal), 5.32 (1H, d, *J*= 6.0 Hz, SEM), 5.24 (1H, d, *J*= 6.0 Hz, SEM), 4.90 (2H, d, *J*= 9.9 Hz), 4.40-4.46 (2H, m), 4.32-4.37 (1H, dd, *J*= 10.5, 6.6 Hz), 4,15-4.25 (3H, m), 3.85 (1H,

m), 3.78 (6H, s, -OMe), 3.59-3.74 (3H, m,), 3.35 (1H, t, *J*= 9.5 Hz), 3.29 (1H, m), 3.02 (3H, s, -OMe), 2.61 (1H, dd, *J*= 17.4, 7.0 Hz, H16), 2.34 (2H, t, *J*= 10.5 Hz, H2), 2.20-2.52 (2H, m), 1.96 (1H, m), 1.75-1.84 (3H, m), 1.55-1.70 (5H, m), 1.23 (3H, d, *J*= 6.5 Hz, H6'), 1.20 (3H, d, *J*= 6.5 Hz, 38Me), 1.14 (1.5H, d, *J*= 6.9 Hz, H40), 0.95 (3H, d, *J*= 8.7, H39), 0.91, 0.90, 0.87, 0.83, 0.75(46.5H, s, TBS, SEM, H40), 0.11-–0.14(41H, TBS, SEM); ^{13}C NMR (100 MHz, $CDCl_3$) δ 172.26, 169.71, 159.71, 159.61, 155.51, 144.02, 143.96, 141.36, 135.86, 133.63, 133.51, 133.32, 133.14, 132.74, 132.46, 132.20, 131.94, 131.73, 131.29, 131.21, 130.26, 127.62, 127.34, 126.96, 124.93, 119.89, 113.46, 113.25, 100.57, 100.17, 99.98, 97.89, 89.73, 80.21, 77.20, 75.29, 73.83, 73.44, 72.50, 72.34, 72.27, 72.20, 68.21, 68.78, 66.95, 66.66, 57.06, 56.06, 55.24, 47.99, 47.19, 43.03, 42.42, 40.66, 37.08, 36.01, 32.22, 31.84, 30.34, 28.91, 26.97, 26.08, 25.98, 25.75, 25.61, 18.84, 18.38, 18.31, 18.24, 18.11, 17.98, 17.82, 17.70, 14.02, 10.94, −1.44, −3.96, −4.03, −4.17, −4.26, −4.39, −4.43, −4.56, −5.14, −5.33; MS (ESI) m/z calcd for $C_{113}{}^{13}C_2H_{181}NNaO_{22}Si_6$ [M+Na$^+$] 2121.1656, found: 2121.1663

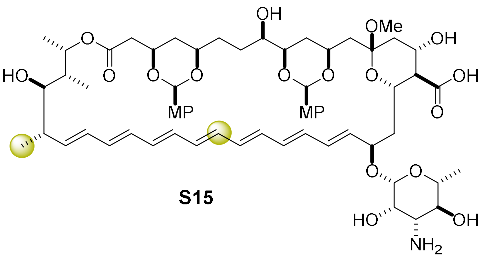

S15

Conversion of S14 to S15. Macrolactone **S14** (85 mg, 40 µmol) was dissolved in methanol (2.0 mL) in a Teflon reaction vessel. 18% HF-pyridine (1.6 ml) was added dropwise at room temperature, then the temperature was raised to 50 °C, and the mixture was stirred for 39 hours. The reaction solution was added dropwise to a saturated aqueous sodium hydrogen carbonate solution to stop the reaction, and the mixture was extracted with ethyl acetate. After drying the organic layer with anhydrous sodium sulfate, the solvent was distilled off under reduced pressure. The residue was crudely purified on an ODS column (0: 1-1: 0 methanol / H_2O) to give a yellow solid.

The obtained crude product (83 mg) was dissolved in dichloromethane (4.0 ml), piperidine (122 µl, 1.24 mmol) was added, and the mixture was stirred at room temperature for 4 hours. The solvent was evaporated under reduced pressure, and the residue was crudely purified by silica gel column chromatography (methanol / chloroform, 0:1 — 1: 0) to give compound **S15** (72 mg, impure) as a yellow solid.

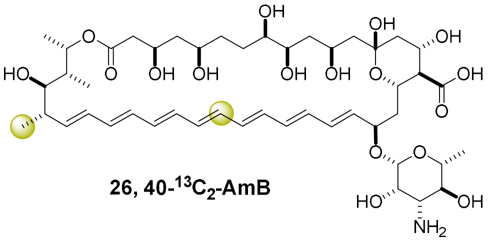

26, 40-$^{13}C_2$-AmB

Conversion of S15 to 26,40-$^{13}C_2$-AmB 6. Compound **S15** (72 mg) was dissolved in methanol (2.6 ml), cooled to 0 °C, concentrated hydrochloric acid (327 µl) was added dropwise, and the mixture was stirred at 0 °C for 20 minutes. Sodium hydrogen carbonate (409 mg) was added to stop the reaction, and it was confirmed that the pH was around 7. After filtration, the solvent was distilled off under reduced pressure. The obtained residue was dissolved in t-butanol (3.2 ml) and H2O (0.8 ml), concentrated hydrochloric acid (163 μl) was added thereto, and the mixture was stirred at 0 ºC for 5 hours. The reaction mixture was charged on an ODS open column (0: 1－1: 0 methanol / H2O) and crudely purified to obtain a yellow solid. It was repurified by HPLC to give pure 26,40-$^{13}C_2$-AmB (2.5 mg, 7% for 4 steps) as a yellow solid.

Solution MMR spectra of synthetic intermediates and product

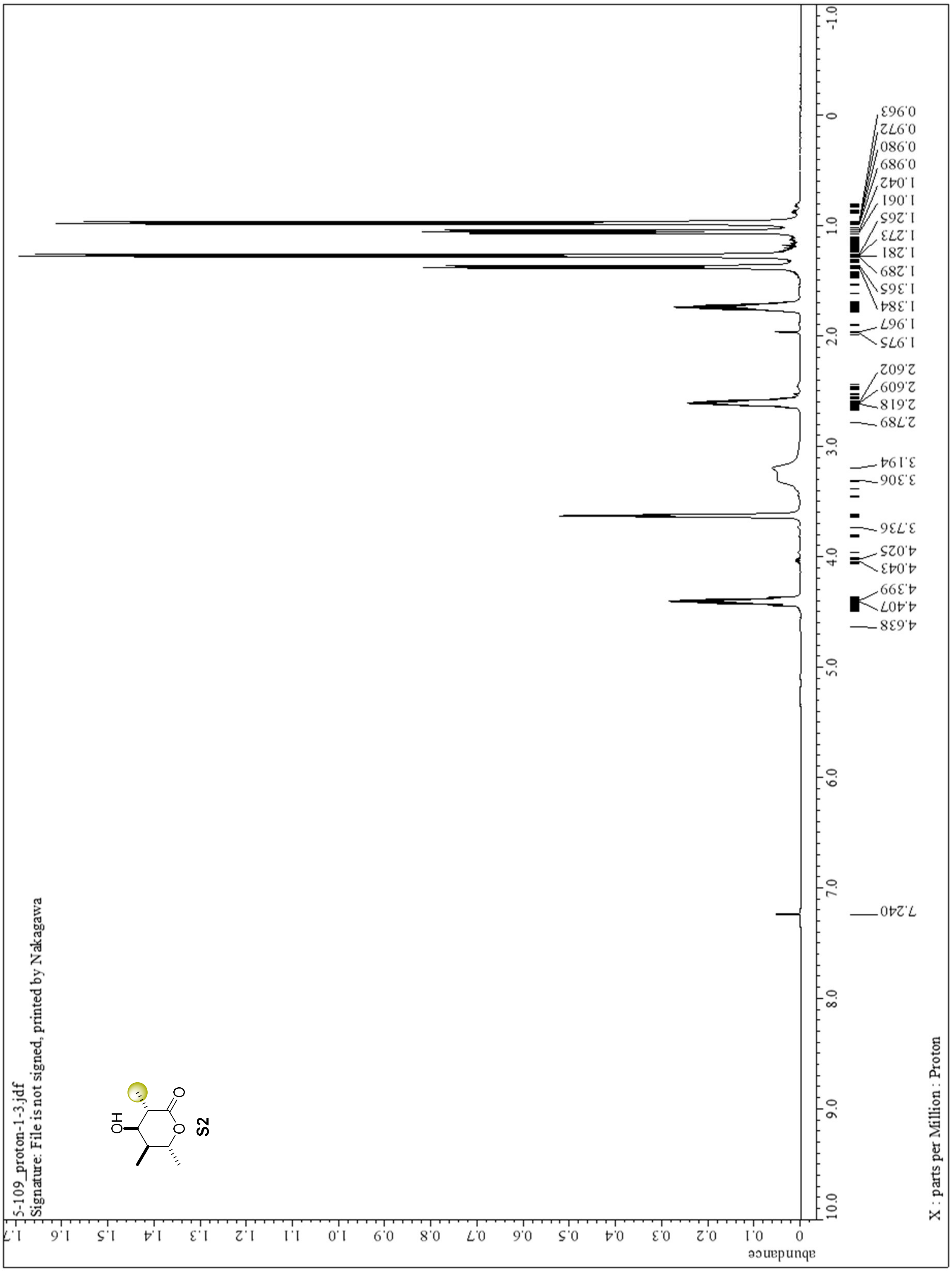

Fig. S9. ^{1}H NMR spectrum of compound **S2**.

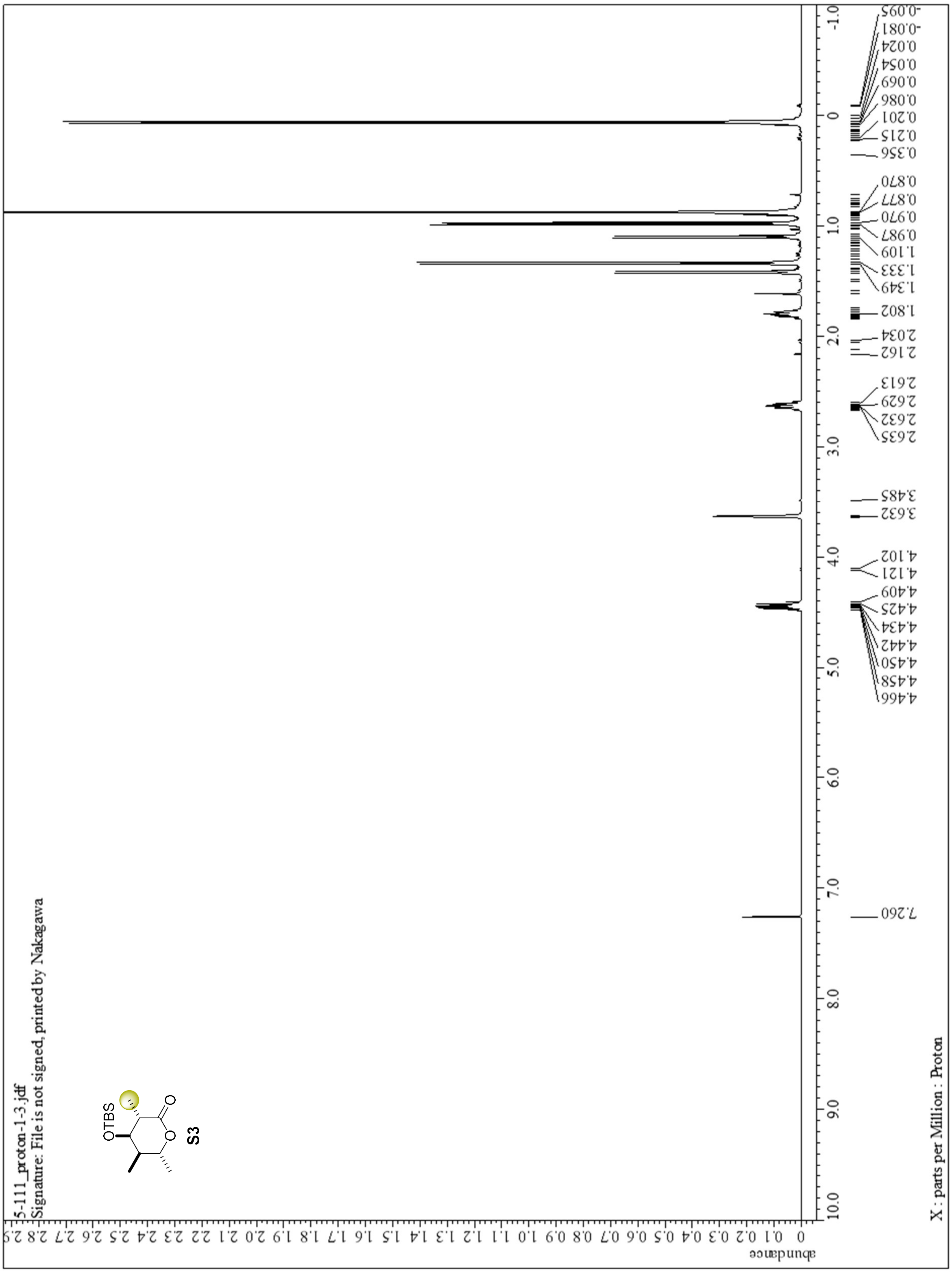

Fig. S10. ^{1}H NMR spectrum of compound **S3**.

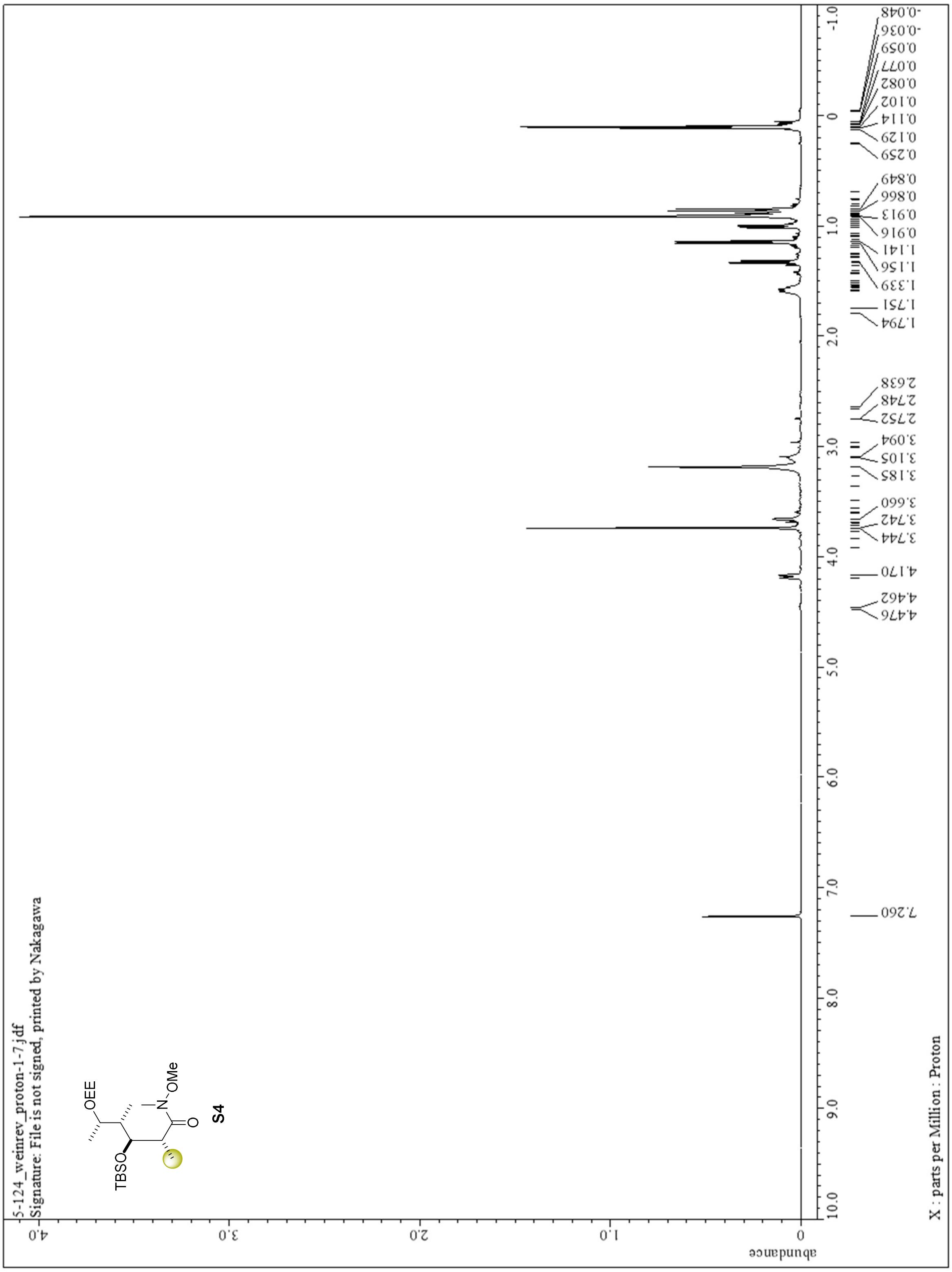

Fig. S11. ^{1}H NMR spectrum of compound **S4**.

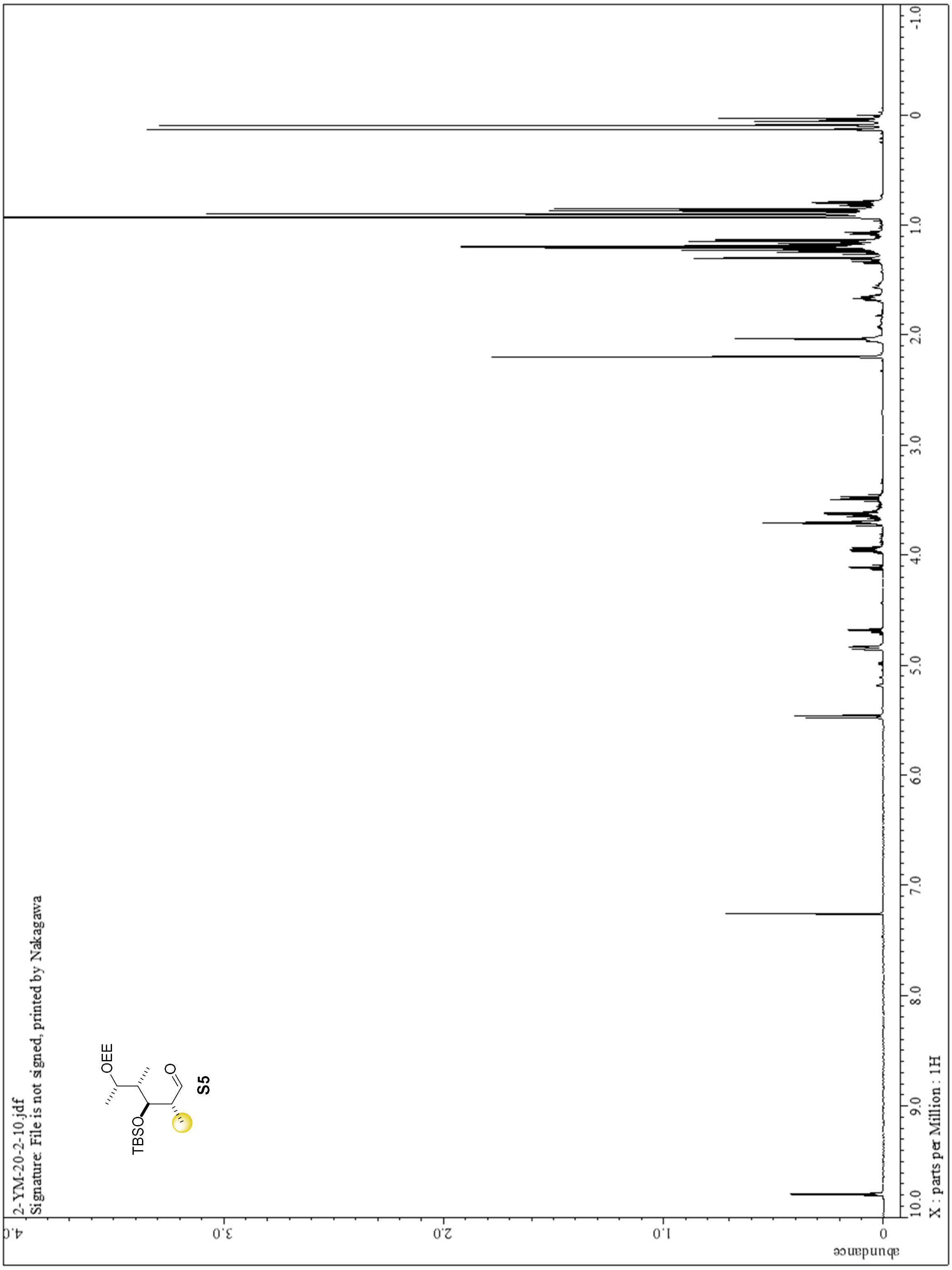

Fig. S12. ^{1}H NMR spectrum of compound **S5**.

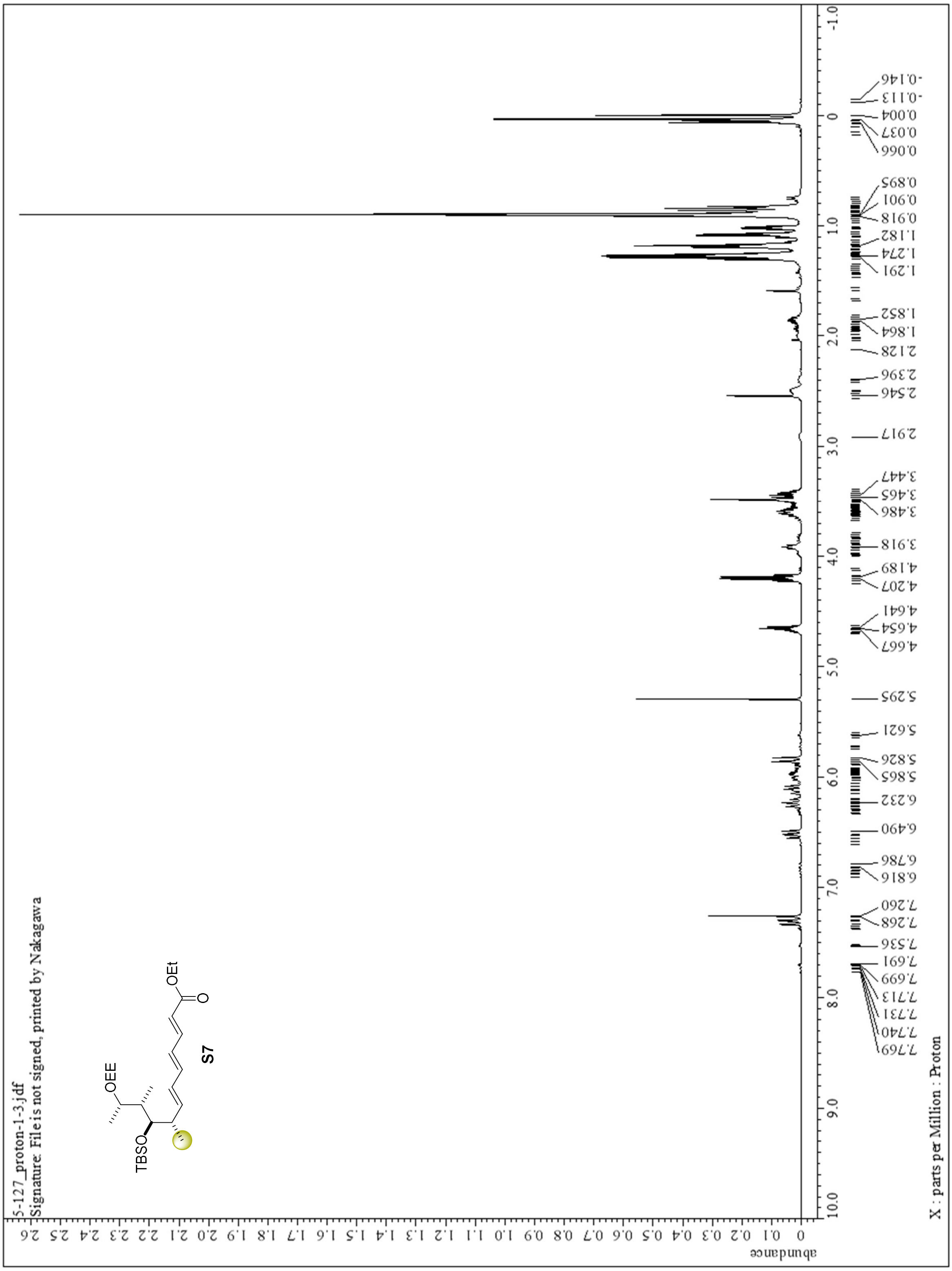

Fig. S13. ^{1}H NMR spectrum of compound **S7**.

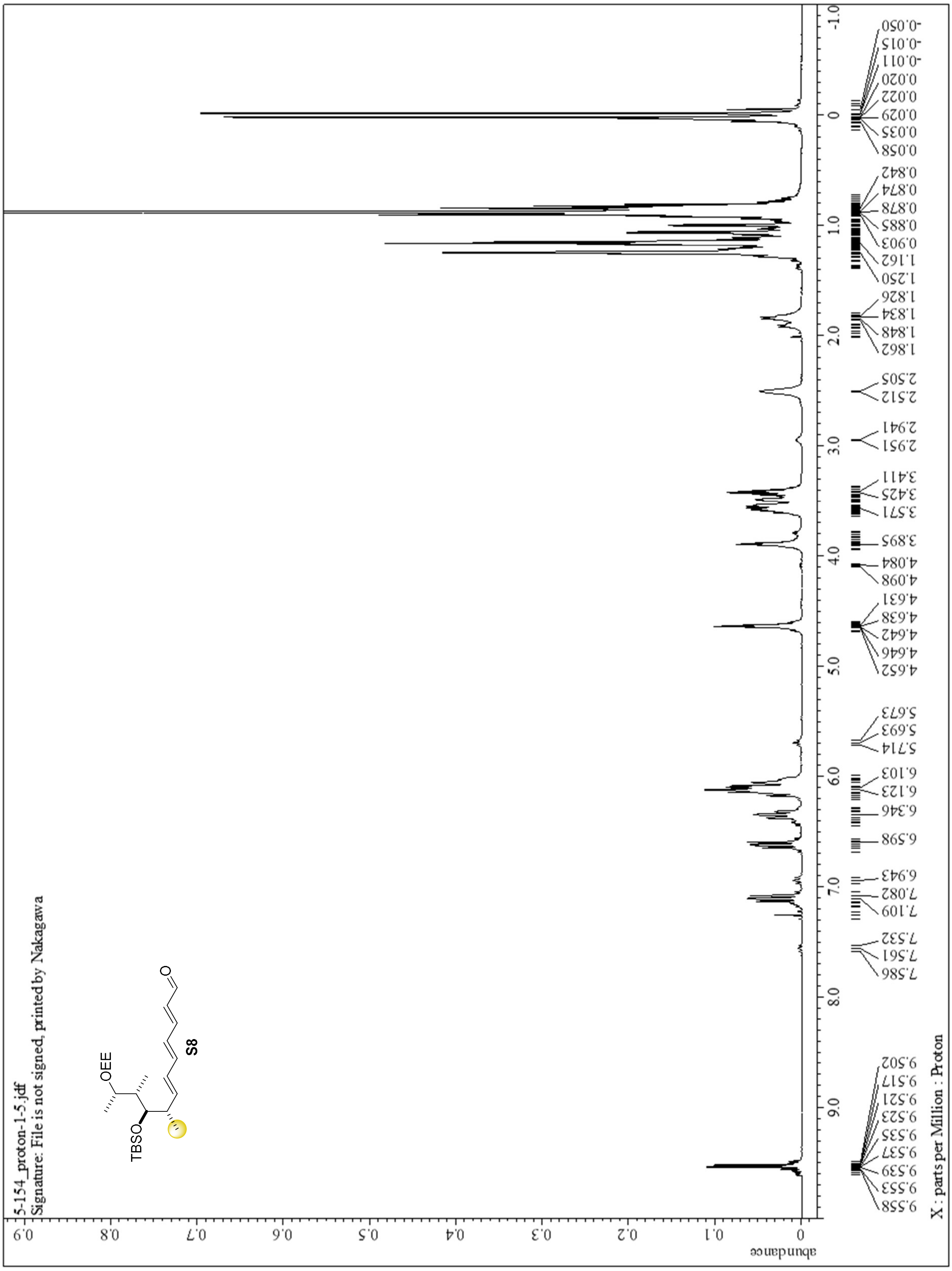

Fig. S14. ^{1}H NMR spectrum of compound **S8**.

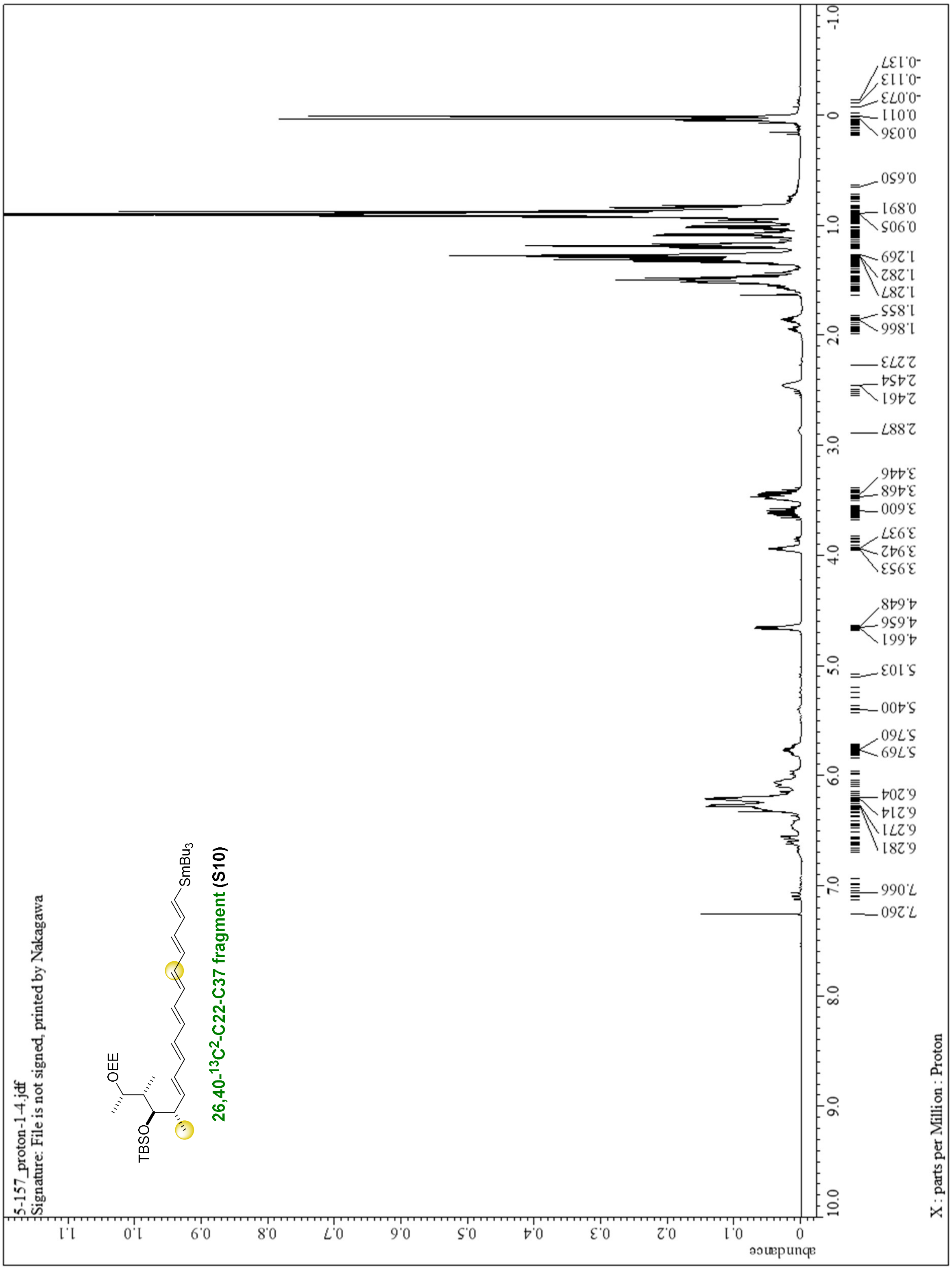

Fig. S15. ^{1}H NMR spectrum of compound **S10**.

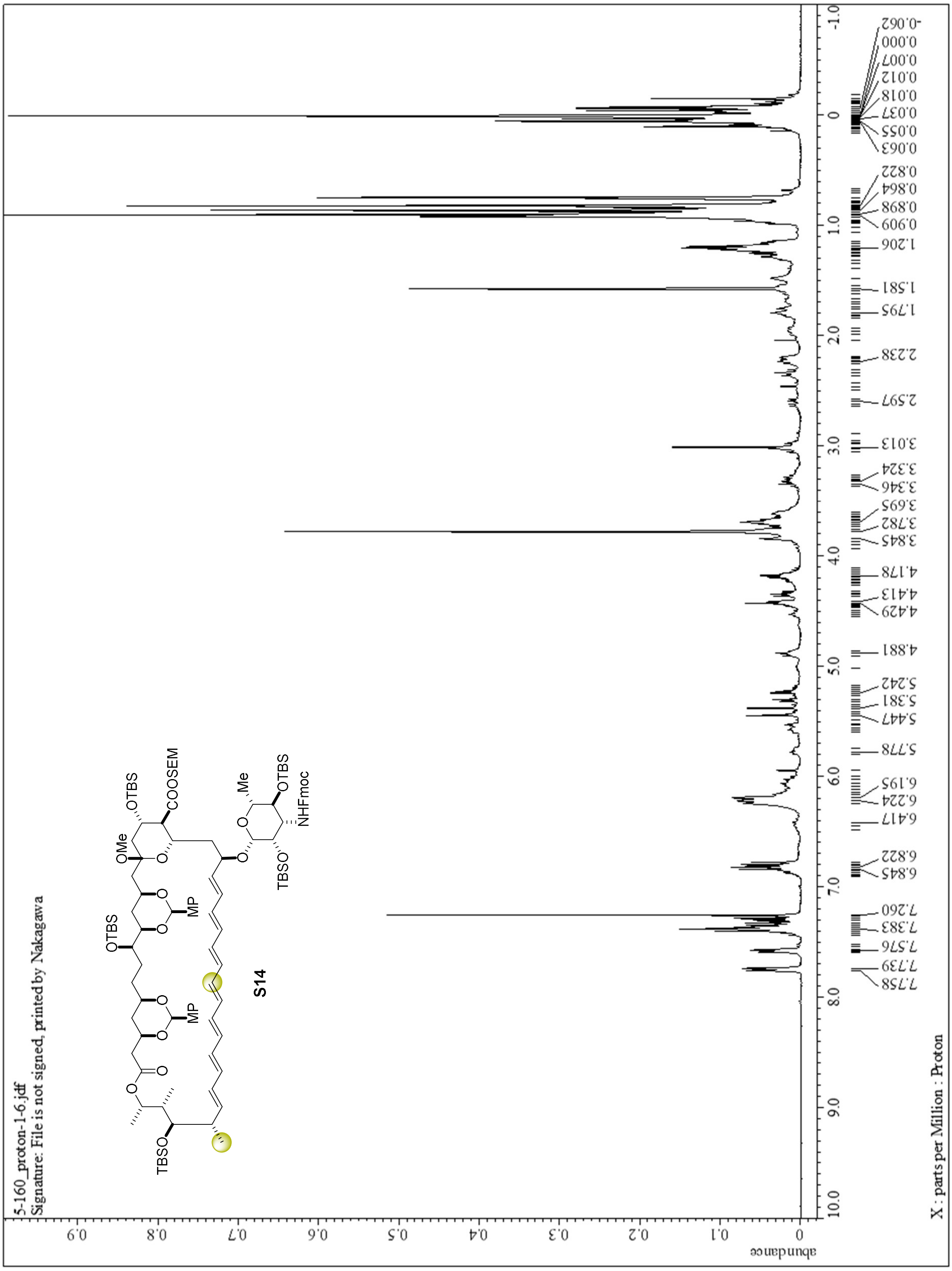

Fig. S16. ^{1}H NMR spectrum of compound **S14**.

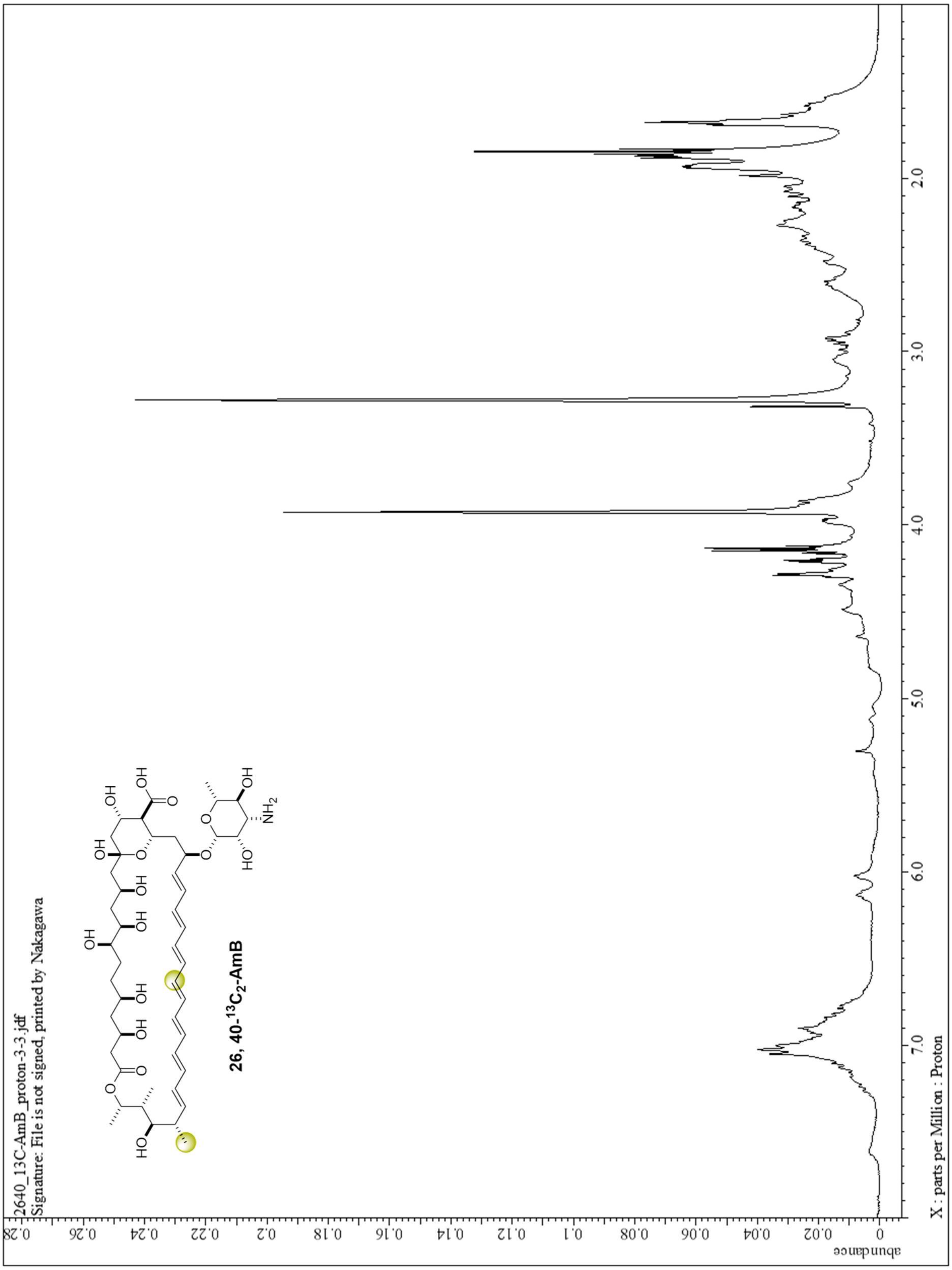

Fig. S17. ^{1}H NMR spectrum of compound **26, 40-$^{13}C_2$-AmB**.

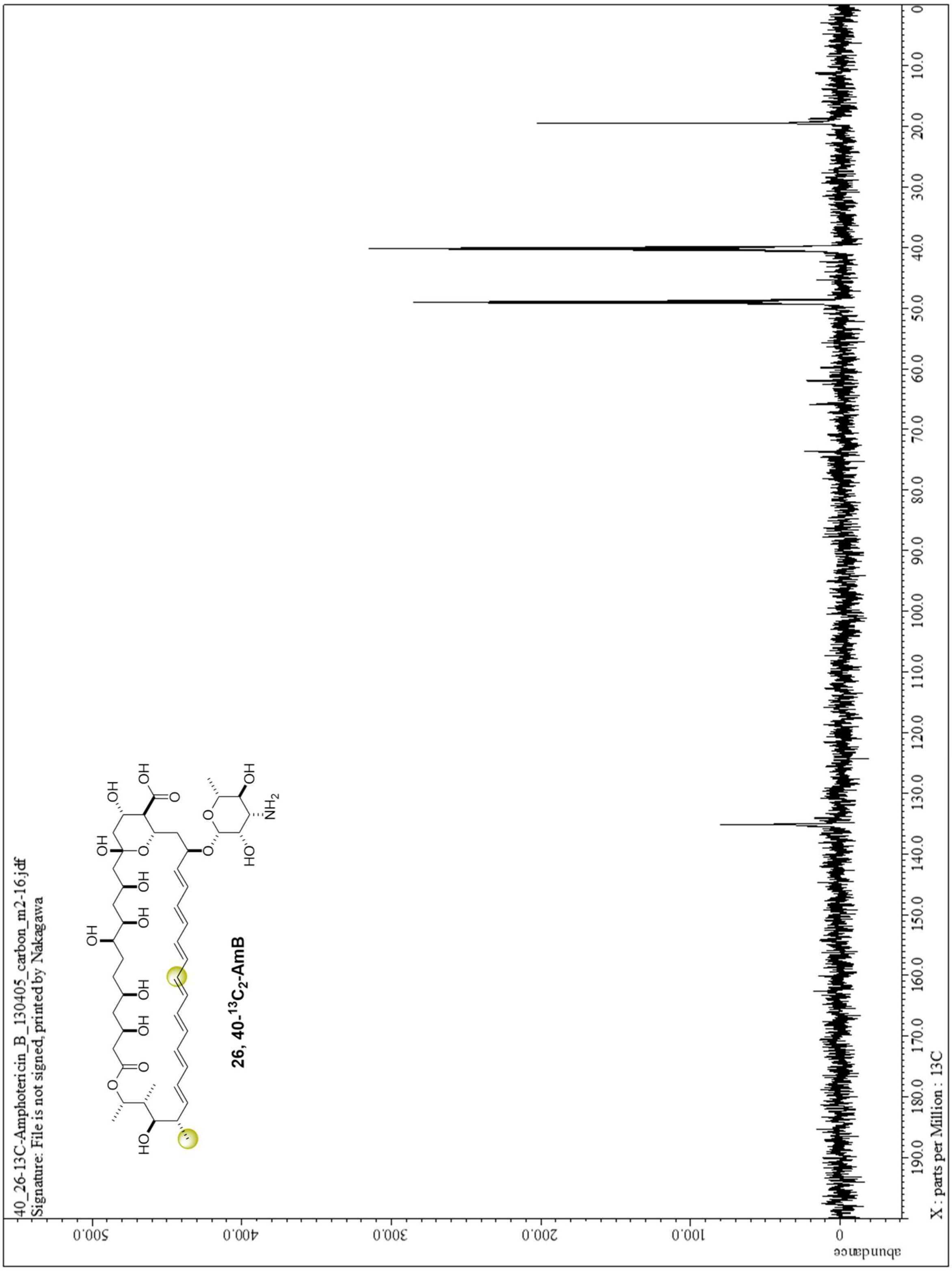

Fig. S18. ^{13}C NMR spectrum of compound **26, 40-$^{13}C_2$-AmB**.

Supplementary Figures and Tables with Text

I. Spectroscopic results and their interpretation in combination with MD simulations

Biological activities of fluorinated AmB analogues:

Table S3 shows that fluorinated AmB, 14-F-AmB and 32-F-AmB (their structures are given below) used in this study showed similar biological activities to those of AmB. The stereochemistry at C14 of 14-F-AmB is the *S* configuration (*19*). Regarding ion permeability, 14-F-AmB and 32-F-AmB, which were used for the NMR measurements, revealed the Erg-dependent activities with similar potency to AmB (Fig. S19). It was shown that the AmB assemblies formed in the artificial membrane under the same lipid composition as that in the NMR experiments efficiently form all-or-none type K^+ channels as reported for the ion permeability of AmB (*72*).

Table S3. Biological activity of F-labeled AmB analogues in comparison with AmB

Compound	Relative hemolytic activity[a]	Antifungal activity (μg)[b]
AmB	1.0	10
14-F-AmB	0.9	10
32-F-AmB	1.2	10

[a] Relative hemolytic activity in EC_{50} to AmB, where AmB induced the hemolysis with the EC_{50} of 1.4-5.6 μM, depending on the preparation of human blood cells. [b] The minimum amount of compounds on a paper disk that showed inhibitory zone on the culture of *Aspergillus niger* with the common ratio being 3 after 60–80 h.

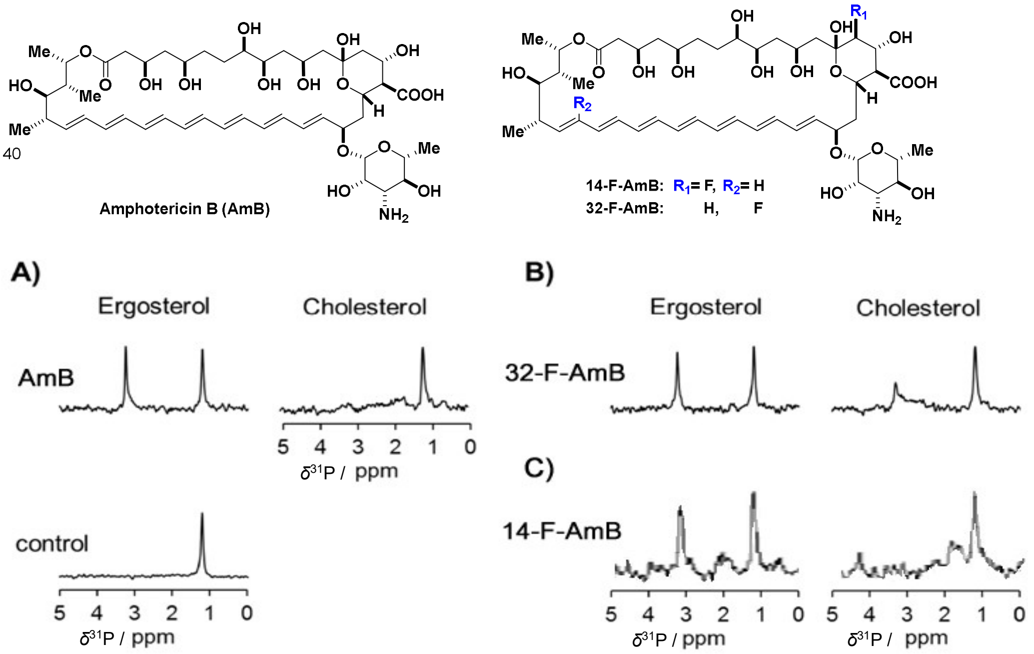

Fig. S19. K$^+$ ion permeation experiment of AmB channels based on ^{31}P NMR. AmB (A), 32-F-AmB (B), 14-F-AmB (C) from POPC membrane containing 10 mol% Erg and Cho in egg PC bilayers mainly consisting of POPC. AmB and the analogues were added in advance to the liposomes, and the influx of K$^+$ was measured as a change in the pH of liposome lumens (*72*). The signals were due to the inorganic phosphate inside the liposome. The ^{31}P resonance near 1 ppm is the signal of phosphate in the liposomes without K$^+$ inflex, and the signal around 3 ppm is the signal in the liposome after K$^+$ has finished flowing in. The ratio of AmB and fluorinated AmB to phospholipids was 0.01 mol%, and the control was the result without AmB (*19*).

Setting up the conformation of AmB monomer for constructing the time-averaged structure of the AmB assembly based on the interatomic distance:

The initial structure of the AmB molecule: The crystal structure (*28*) was used as the conformation of the macrolide ring. For the relative conformation of a mycosamine moiety to the macrolide, which is the only flexible portion in the AmB structure, we used the dihedral angles, φ (C1'-O-C19-C18), ψ(C2'-C1'-O-C19) = −89°,154° in the C$_6$-crosslink **3** that showed the highest Erg selectivity in K$^+$ flux activity (Table S4) (*29*) as the initial structure, and minimized the energy with respect to the angles φ, ψ for AmB after eliminating the crosslinker using MacroModel (calculated without limitation in these dihedral angles in octanol). As a result, we obtained the dihedral angle (φ, ψ) = (−69.0°, 176.4°) of the stable conformation, which was used for the subsequent structural elucidation of AmB assembly. These dihedral angles agree well with the active conformation of AmB proposed in previous studies (*73*).

Table S4. K$^+$ flux activity (EC$_{50}$) of AmB Crosslinkers 2–4* (*23*)

Compound	Sterol-free	Cho	Erg
AmB	47	43	11
C$_4$-Crosslink **2**	61	86	50
C$_6$-Crosslink **3**	60	58	5.8
C$_8$-Crosslink **4**	180	110	27

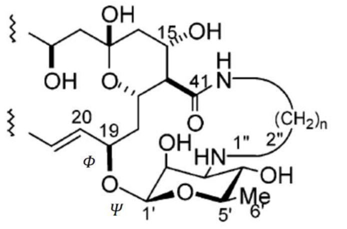

2: n=4
3: n=6
4: n=8

*The activity was determined by ^{31}P NMR (Fig. S19) and expressed as a compound/lipid molar ratio, R_a (x10^6) to induce the activity of EC$_{50}$.

REDOR results of AmB assembly under two kinds of lipid compositions:

REDOR experiments were basically performed to determine the interatomic distance on two kinds of the lipid bilayers (MLVs) with different lipid composition ratios, AmB/Erg/POPC = 1: 3: 7 and 1: 1: 9. At the ratio of 1: 3: 7, the saturated amount of Erg bound to the AmB assemblies, but under the lower Erg ratio (1: 1: 9), the bound Erg to the assemblies was only 23% and did not reach saturation (*23*). In order to determine the position and orientation of Erg molecules bound to the AmB assembly with ^{13}C-labeled Erg, the highest possible proportion of Erg molecules must be bound to the assembly, so AmB with a low Erg content, AmB/Erg/POPC = 1: 1: 9, was used. On the other hand, to stabilize the AmB assembly, it was desirable that many Erg molecules be bound to the assembly, so the measurement was performed with a high Erg content. Since we used the position and orientation of a bimolecular AmB-Erg complex determined under the condition of the ratio of 1: 1: 9 (*23*), it was necessary to obtain the NMR results with this composition. Thus, we investigated the structural difference of the AmB assemblies under the 1: 3: 7 and 1: 1: 9 ratios. As a result, 14-F REDOR (and CODEX) experiments performed in both ratios showed no significant differences in the interatomic distances between 14-F and C41 or 14-F and C1' (Fig. S20). The structure of AmB assemblies could, therefore, be regarded as indistinguishable under these two conditions.

We preferentially used the results obtained with the 1: 3: 7 composition ratio, where we recorded more data on the REDOR experiments (Fig. 2B). However, in the NMR experiment using 32,40-^{13}C$_2$-AmB, we used the results only at the 1: 1: 9 ratio because it was difficult to obtain reliable $\Delta S/S_0$ values in the 1: 3: 7 ratio due to the heavy overlap of the C40 signal of AmB on the Erg signals with the higher Erg content.

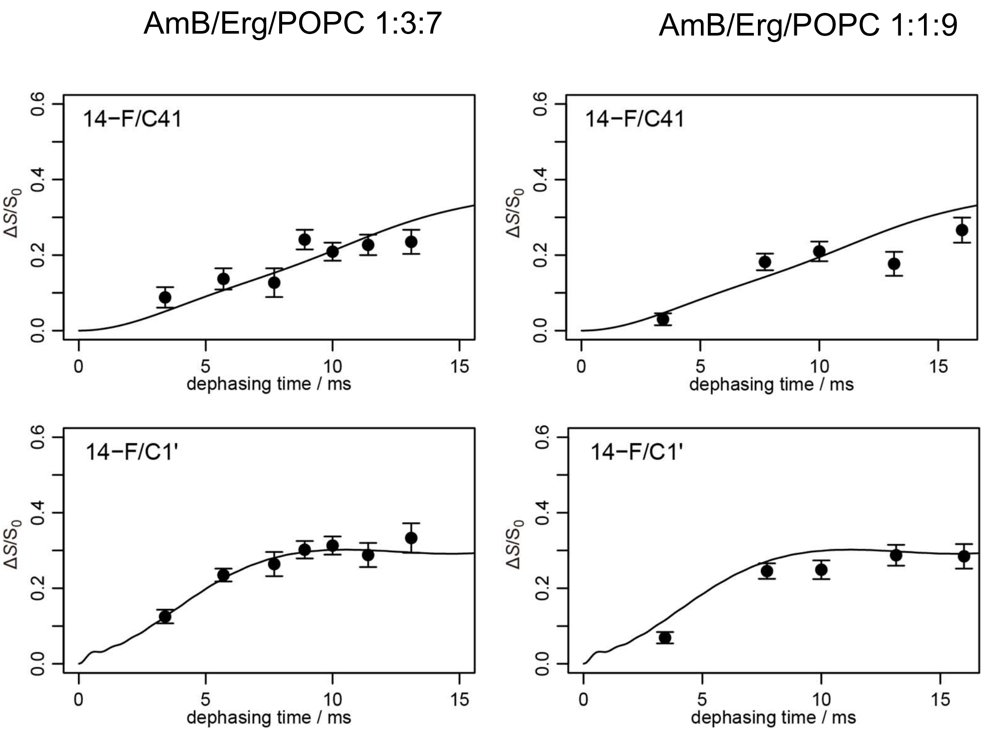

Fig. S20. REDOR experiment of 14-F-AmB/skipped ^{13}C-AmB/Erg/POPC membranes with two kinds of the lipid compositions. Comparison of lipid composition 0.5: 0.5: 3: 7 (left) and 0.5: 0.5: 1: 9 (right). The error bars denote the S/N ratios of ΔS signals.

The intermolecular distances of 14-F/C41 in Fig. 4E are significantly smaller than the previous value, 12.1 Å (*45*). This is mainly because the probability *p* of adjacent fluorine-labeled AmB and natural AmB was set to 0.5 assuming a random mixture in the previous report. This is the reason that the magnitude of the magnetic dipole coupling estimated from the previous REDOR study became smaller, resulting in a longer distance than the current one where the *p*-value was 0.24.

Setting-up of neighboring probability parameters *p* and *p*' for estimating the interatomic distance between AmB-AmB molecules:

We introduced the parameter *p*-value for estimating the interatomic distance in REDOR for the following reason. As shown in Fig. 1E and Fig. S22, the MLV preparations with 14-F-AmB and 32-F-AmB contained considerable amounts of the AmB analogues that did not bind to the membrane. The ratios varied depending on preparation of AmB-containing MLVs. Since fluorine with a large electric dipole was introduced in the polar headgroup of AmB, it was expected that the molecular behavior of fluorinated AmB analogues could be different from that of AmB. For this reason, we set different *p*-values, the probability of F-AmB being adjacent to ^{13}C-labeled AmB. We adopted the single *p*-value for the adjacency probabilities of F-AmB to ^{13}C-AmB on both faces bearing the interatomic distances r_1 and r_2 (Fig. 3B); all the assemblies, even with various numbers of AmB molecules, have cyclic structures, where ^{13}C-AmB is always adjacent to F-AmB at two or more even-numbers of points when one or more F-AmB is contained. One half of them are on the r_1 side and the other half are on the r_2 side. That is, all combinations of AmB assemblies have the same number of pairs of ^{13}C-AmB and F-AmB adjacent on the r_1 side and those on the r_2 side (regarding the probability of ^{13}C-AmB sandwiched between F-AmBs, whether it can be regarded as p^2 will be discussed next).

We considered that the number of labeled-AmB molecules per assembly was different between 14-F-AmB and 32-F-AmB, and the probability of their adjacency with ^{13}C-labeled AmB in the assembly was also different. Thus, we used the different adjacent parameters *p* and *p*' for the 14-F-AmB and 32-F-AmB experiments. For 14-F-AmB, the probability *p* is as low as 0.24. As one of the causes, the uptake rate of 14-F-AmB in the membrane is reduced, which has been experimentally confirmed by the observation that a part of 14-F-AmB was present outside of the membrane (in the aqueous media), as shown in Fig. 1E. It is also possible that the affinity between 14-F-AmB and 14-F-AmB is higher than that between 14-F-AmB and ^{13}C-AmB.

On the other hand, the adjacent probability for ^{13}C-AmB sandwiched with two 14-F-AmB molecules could be influenced by fluorine effects on both side (Fig. S21B). In other words, it should be treated as a separate probability parameter rather than p^2. Therefore, we set the probability of the sandwich structure as p_{FCF} and examined how much it affects the REDOR curve. Fig. S21C shows the REDOR attenuation curves when *p* is fixed at 0.24 and $p_{\mathrm{FCF}}{}^2$ is changed from 0.04 to 0.09 (parameters other than probability adopt the optimum values in Fig. 3C). It was confirmed that p_{FCF} affects the REDOR curve to some extent, but does not significantly influence the interatomic distances.

Regarding 32-F-AmB, '$p' = 0.5$' means that 32-F-AmB and ^{13}C-AmB are adjacent to each other with almost equal probability, suggesting that there is no difference in affinity for ^{13}C-AmB between 32-F-AmB and ^{13}C-AmB. Therefore, the adjacent probability of ^{13}C-AmB sandwiched between 32-F-AmB can be expressed by p'^2.

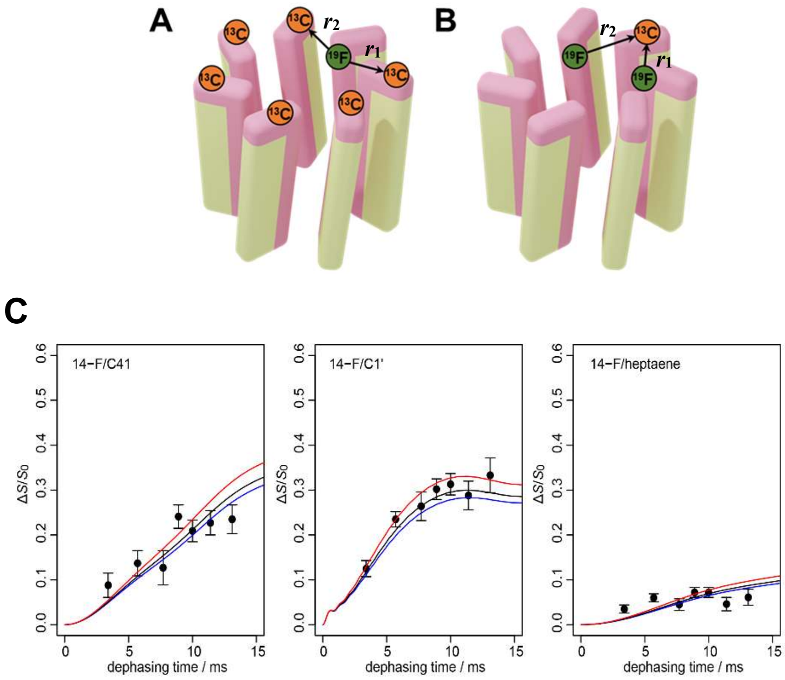

Fig. S21. Evaluation of influence of parameter *p* on the REDOR results. (A) As an example, the state of a channel assembly consisting of six molecules of ^{13}C-AmB and one molecule of 14-F-AmB is shown. At this time, the case of lining up to the right and the case of lining up to the left are synonymous, and REDOR attenuation occurs in ^{13}C-AmB of 2 molecules (33%) out of 6 molecules. (B) The structure sandwiched between fluorine is affected by the difference in affinity between 14-F-AmB and ^{13}C-AmB. (C) The REDOR plots with different p_{FCF} value; 0.04 (blue), 0.058 (= 0.24^2, black), 0.09 (red). The error bars denote the S/N ratios of ΔS signals.

14-F-AmB partly remained outside membranes:

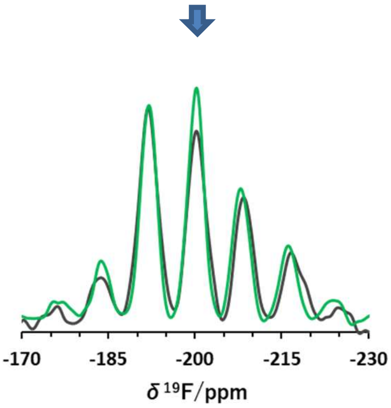

Fig. S22. ^{19}F NMR spectra showing that 14-F-AmB did not completely bind to the membrane. The spectra were taken at 376 MHz for 14-F-AmB-Erg-POPC 1:3:7 mixture under magic angle spinning at 3 kHz. In the 14-F-AmB spectra where the spectra at 0 °C and at -36 °C are shown with green and black traces, respectively, the peak intensity (arrow) near the isotropic chemical shift was increased at 0 °C, which means that a certain fraction of the F-AmB has high mobility and does not bind to the membrane. Thus, for estimating the number of AmB molecules per channel assembly, the isotropic peak (arrow) was not included for calculating the S/S_0 values in Fig. 1F.

How to elucidate the symmetric structure (time-averaged) of an AmB assembly based on RMSD analysis of NMR-derived distance:

The parameters that we used to elucidate the NMR-derived structure of the AmB assembly are shown in Fig. 3. The process of minimizing RMSD was divided into two steps, as shown below, and lastly, the best parameter set that yielded the minimum RMSD (Fig. S23) was obtained by combining both. To eliminate the REDOR dephasings caused by longer ^{13}C-^{19}F spin pairs such as inter-channel interaction, the experimental data observed at less than 15 ms dephasing time (seven data points for each labeled position) were taken into account for channel structure screening. Regarding the dephasing curve within 15 ms, the shorter of the two ^{13}C-^{19}F distances (r_1 and r_2), which is less than 10 Å including C20 and C22 in the heptaene, has the dominant dephasing effect. When the longer distance exceeds 12 Å, it has little effect on the channel structure. The best-fit parameters were obtained by RMSD analysis.

1) A relatively high *S*/*N* ratio in REDOR spectra was achieved with 14-F-AmB in the composition 14-F-AmB/^{13}C-AmB/Erg/POPC = 0.5: 0.5: 3: 7. Thus, we collected more REDOR dephasing data with 14-F-AmB-containing samples (Fig. 2B), particularly for the upper part of an AmB assembly. The six parameters (α, β, γ, n, R, p) to define the position/orientation of AmB molecules were taken as follows (see Fig. S23-I for α, β, γ, and R). The oxygen atom at C8 (8-O in Table S1) of AmB was placed at the origin of the AmB molecular frame. The line passing through 14β-H was defined as the z-axis, and the x-axis was defined so that C41 was placed in the xz plane, thus allowing the line orthogonal to these axes to be the y-axis (Fig. S23-IA, where these axes are shown in blue). In addition, the same direction as each axis at panel **A** was defined as the X, Y, Z axes (capital letters) of the bilayer frame; see Fig. 3A and Fig. S23-IA where the bilayer coordinate axes are shown in red. Next, with respect to the bilayer frame, an AmB molecule was rotated by Euler angles to change its orientation with respect to the membrane normal (Fig. S23-IB). AmB was then translated in the X-axis direction of the bilayer frame to provide a space for pore formation. The pore radius R is defined as the distance between the origin of the bilayer frame and the origin (8-O) of the AmB molecular frame (Fig. S23-IC). That is, after forming a C_n symmetric AmB channel, the Z axis is in the direction of the pore axis and located at the center of the pore. Some of these parameters were varied within certain ranges based on the structural outline (Fig. S25) deduced from NMR results as follows. Upon varying the Euler angles α, β, γ of each AmB molecule in the bilayer frame, the angle between the C16/17-O vector of AmB and the membrane normal was restricted to a range from -25° to 25° by assuming the single-length channel. The number of AmB molecules per assembly, n, was varied from four to eight, for which the CODEX results implied that the average number is close to 7 (Fig. 1F). The inner radius R (the radius of a circle formed by the oxygen atom 8-O of each AmB molecule in C_n symmetric structure) is varied from 4 Å to 5.5 Å based on previous studies(*74, 75*). For the adjacent probability p, see the text (page S38) before Fig. S21. Of the parameter sets thus obtained, the sets with RMSD smaller than 0.035 were adopted as RMSD1

for the next step of calculation; those larger than 0.035 were rejected; When the RMSD exceeds 0.035, the value of REDOR attenuation exceeds the error ranges that are shown in Fig. 3.

2) The same RMSD calculation as described in 1) was then performed for the REDOR experiments of 32-F-AmB, which could precisely provide the intermolecular distances in the bottom portion of an AmB assembly. We used another probability p' for 32-F-AmB as described in the text before Fig. S21. The newly calculated value for the parameter set (α, β, γ, n, R, p, p') was defined as RMSD2. Since the number of data points for 14-F-AmB was 21 and that for 32-F-AmB was 5, the final RMSD was calculated as RMSD3 = 21/26 × RMSD1 + 5/26 × RMSD2. The structure that gave rise to the smallest RMSD3 value was defined as the "symmetrical structure of the AmB assembly determined by NMR". As is evident from Fig. S23-II, each parameter shows the minimum value in a relatively narrow range, and the parameters that gave the minimum value of RMSD3 were ($\alpha, \beta, \gamma, n, R, p, p'$) = (-12, 2, -20, 7, 5.4, 0.24, 0.5). Pore size and channel activity in the dynamic structure of the AmB channels are described in detail in Figs. 4 and S31.

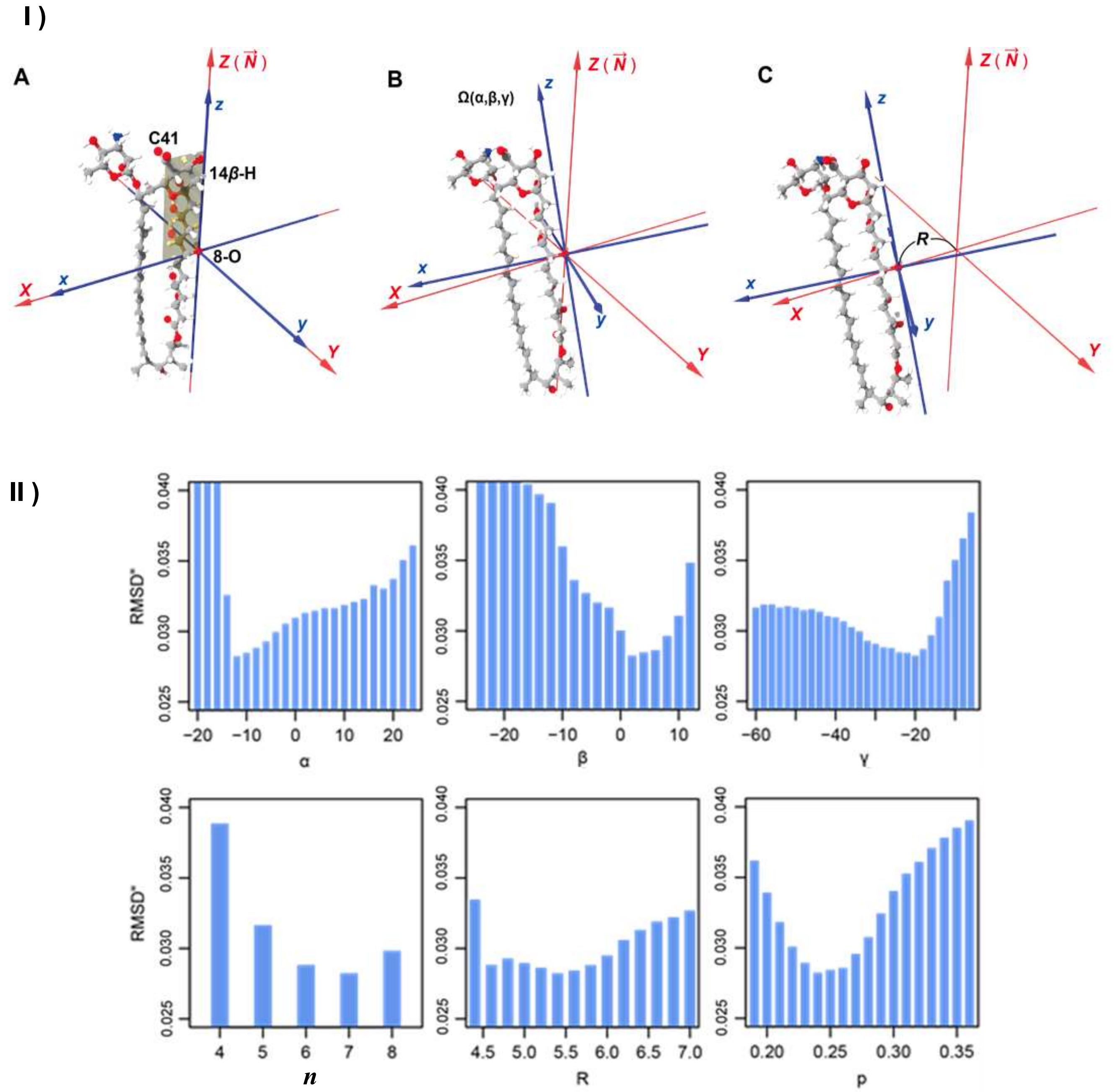

Fig. S23. Optimal parameters obtained by RMSD analysis based on the REDOR results of two types of AmBs with different ^{19}F-labeling positions. I) Definition of parameters *α, β, γ* and *R* in the AmB molecular frame and the bilayer frame. (**A**) The initial orientation of AmB molecule in the AmB molecular frame (blue axes) that is equal to the bilayer frame (red axes). (**B**) Rotation by Euler angles. (**C**) Definition of channel radius *R*. **II)** The RMSD in the figure is required to reflect both data; *vertical axis corresponds to RMSD3 as described above. For the number of AmB molecules (*n*) varied from 4 to 8, *R, α/β/γ* angles, and *p values* were changed by 0.2 Å, 2°, and 0.01, respectively, for RMSD calculation.

Experimental evidence that AmB orientation is parallel in the assembly:

Assuming that the assembly formed by AmB mimics the half-barrel stave model, we investigated whether AmB monomers are oriented in the same direction (parallel or head-to-head) or partly in the opposite direction (antiparallel or head-to-tail). Most previous studies reported that AmB molecules are aligned in a parallel manner. This orientation was confirmed by measuring the AmB-AmB distances between 14-F and C40 by REDOR experiments by using 26,40-$^{13}C_2$-AmB and 14-F-AmB (Fig. S24). It was found that the distance between 14-F and C40 was larger than 16 Å, which clearly indicated that neighboring AmB molecules in the assembly were almost exclusively arranged in the head-to-head manner.

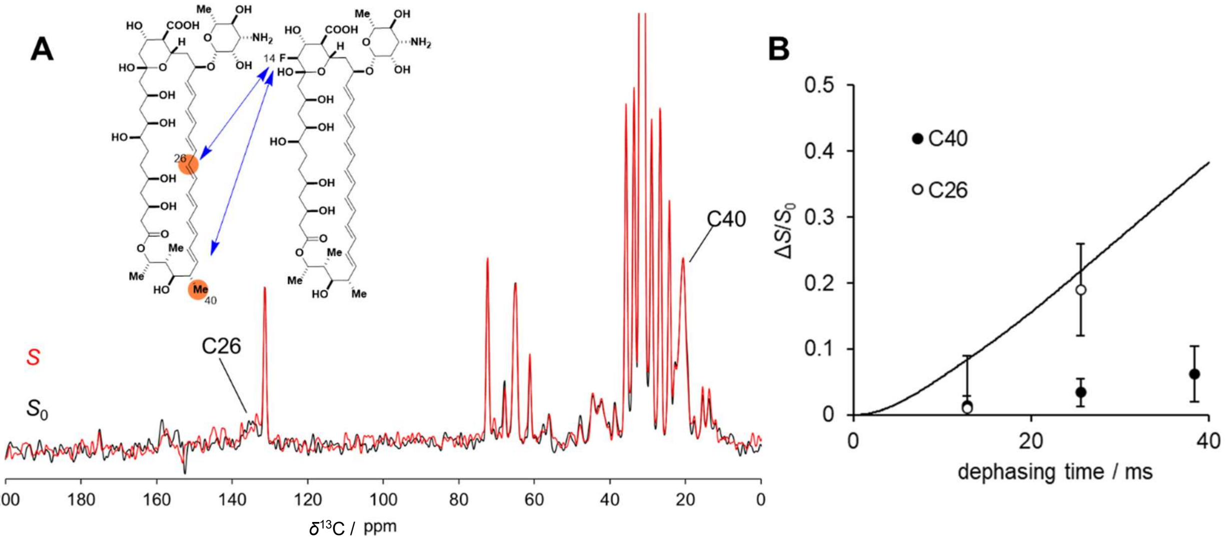

Fig. S24. $^{13}C\{^{19}F\}$ REDOR spectrum (A) for 26,40-$^{13}C_2$-AmB/14-F-AmB (dephasing time: 25.6 ms) and the dephasing curve for C40 and C26 (B). The lipid composition was 26,40-$^{13}C_2$-AmB/14-F-AmB/Erg/POPC = 0.5: 0.5: 1: 9. The result supported the parallel orientation of AmB-AmB in the assembly. Since the relaxation time of the ^{13}C26 signal is much shorter than that of ^{13}C40 and the REDOR attenuation values of ^{13}C26 are not reliable enough under the present measurement conditions, these $\Delta S/S_0$ values of C26 are not included in the channel structure analysis.

Preliminary NMR data analysis and our previous studies support the half-barrel stave structure:

Before constructing a precise assembly structure based on the interatomic distance data, we tried to address two important issues. 1) Is the half-barrel structure an appropriate model for AmB channels? 2) Are assemblies formed by high concentration AmB are similar to those in the fungal membranes that are formed in low concentrations of AmB?

1) From the result of REDOR, it was assumed that the ^{19}F-^{13}C distance between directly adjacent AmB and AmB was relatively small. ^{19}F-^{13}C dipolar interaction within the short distance more strongly reflects the S/S_0 values in the short dephasing time (15 ms or less). Using the S/S_0 values in the range from 3 to 13 ms, the interatomic distances on the polyol side and the polyene side were approximately estimated without considering the parameters R, n or p. As a result, the interatomic distance between the hydrophilic headgroups (14-F and C41) was estimated to be 5–7 Å for the inner side of the upper portion of the assembly, and the distance between the hydrophobic tails (32-F and C40) was 9–13 Å for the outer side of the bottom portion as shown in Fig. S25. These distances suggest that all AmB molecules are arranged in the head-to-head manner within the assembly (see also Fig. S24), and the AmB molecular major axis is approximately in parallel with the pore axis, forming a cylindrical oligomer. Previous studies have reported similar observations that AmB spans the lipid bilayer with a single molecular length (*26*) and the molecular axis of AmB is oriented almost perpendicular to the membrane plane (*27*). Combining these findings, the structure of the AmB assembly in the membrane is conceptually close to the upper half of the classic barrel stave model proposed by de Kruijff et al. (*13*), and other structures are very unlikely.

2) It was shown that the structure mimicking the upper half of the classical channel model was reproduced under the current experimental conditions. Therefore, it was confirmed that AmB assemblies with an ion channel-like structure were formed even under the high concentrations of AmB (about 10 mol% of total lipids; 43 w/w% lipids and 50 w/w% water) used in the NMR experiments. In Figs. S32 and S33, we describe the rationale why the structure of ion channels is not significantly affected by AmB concentrations in the membrane, and also explain the functional similarity between ion-conducting pore examined by channel-recording experiments and the ion channel assembly in the model membrane in Fig. S31 and the text (page S59)

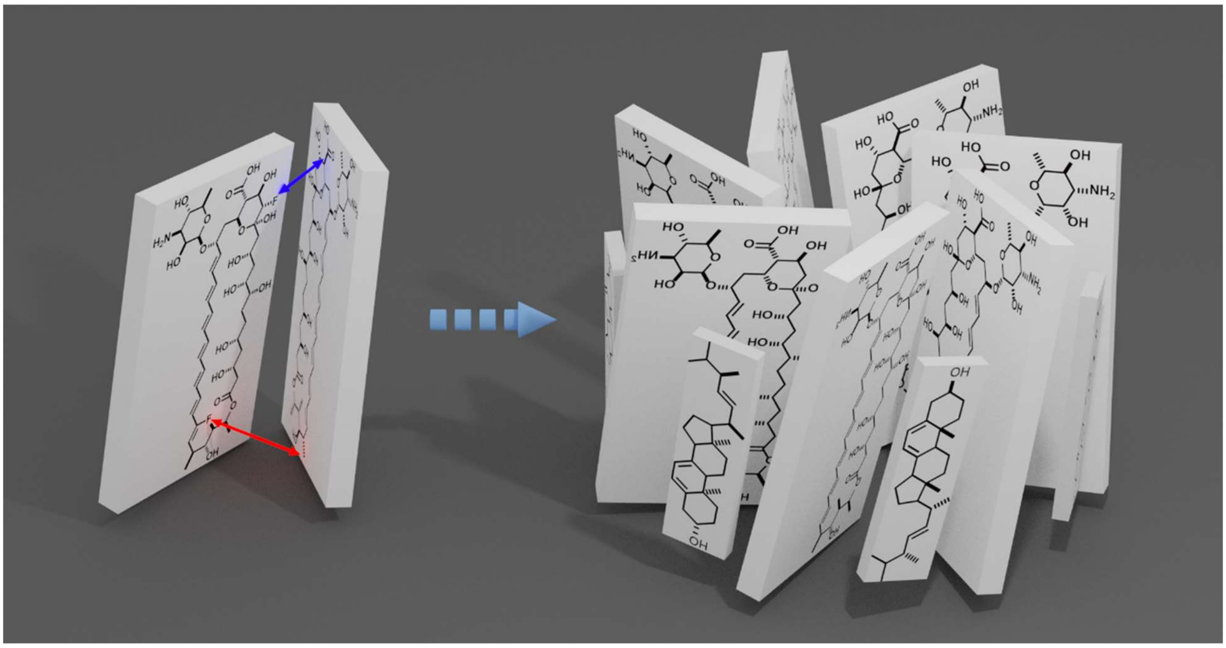

Fig. S25. Structural outline of AmBs in bimolecular complex (left) and resultant assembly (right) deduced from the interatomic distances estimated from REDOR experiments. A rough interpretation of the experimental results (Fig. 3) revealed that the distance between 14-F and C41 at the upper portion of the hydrophilic side (blue arrow) is estimated to be about 5–7 Å, and the distance between 32-F and C40 at the bottom of the hydrophobic side (red arrow) was about 9 −13 Å. These findings indicate that the hydrophilic sides of the adjacent AmB molecules come closer and the hydrophobic sides stay away each other, while the direction of the molecular axe is almost in parallel with the pore axis. The model on the right shows an assembly of seven molecules by arranging AmB-AmB pairs in a rotational symmetric way based on the result of precise distance measurements as described later.

RMSD analysis of the NMR results indicates that heptamer (seven molecules) assemblies are major whereas the assemblies consisting of hexamer (six molecules) or less or octamer (eight molecules) are scarce:

The structures of assemblies with six (**A**), seven (**B**), and eight (**C**) molecular numbers *n* are shown in Fig. S26, where the molecular arrangements that showed relatively good agreement with NMR data obtained by changing the parameters in Fig. S23 are drawn in an overlaying manner. The number of relatively stable structures obtained in the RMSD analysis was 19 for **A**, 77 for **B**, and 2 for **C**, where combinations with the same structure parameters (N, R, α, β, γ) but different probabilities (p, p') are counted as one structure. When the overlapping probabilities are counted separately, **A** is 178 (13%), **B** is 1157 (86%), and **C** is 12 (1%). Although they may not represent the actual distribution of the number of molecules per AmB assembly in the membrane, the NMR-derived distances showed that the heptamer assembly better accounts for the experimental results than hexamer or octamer.

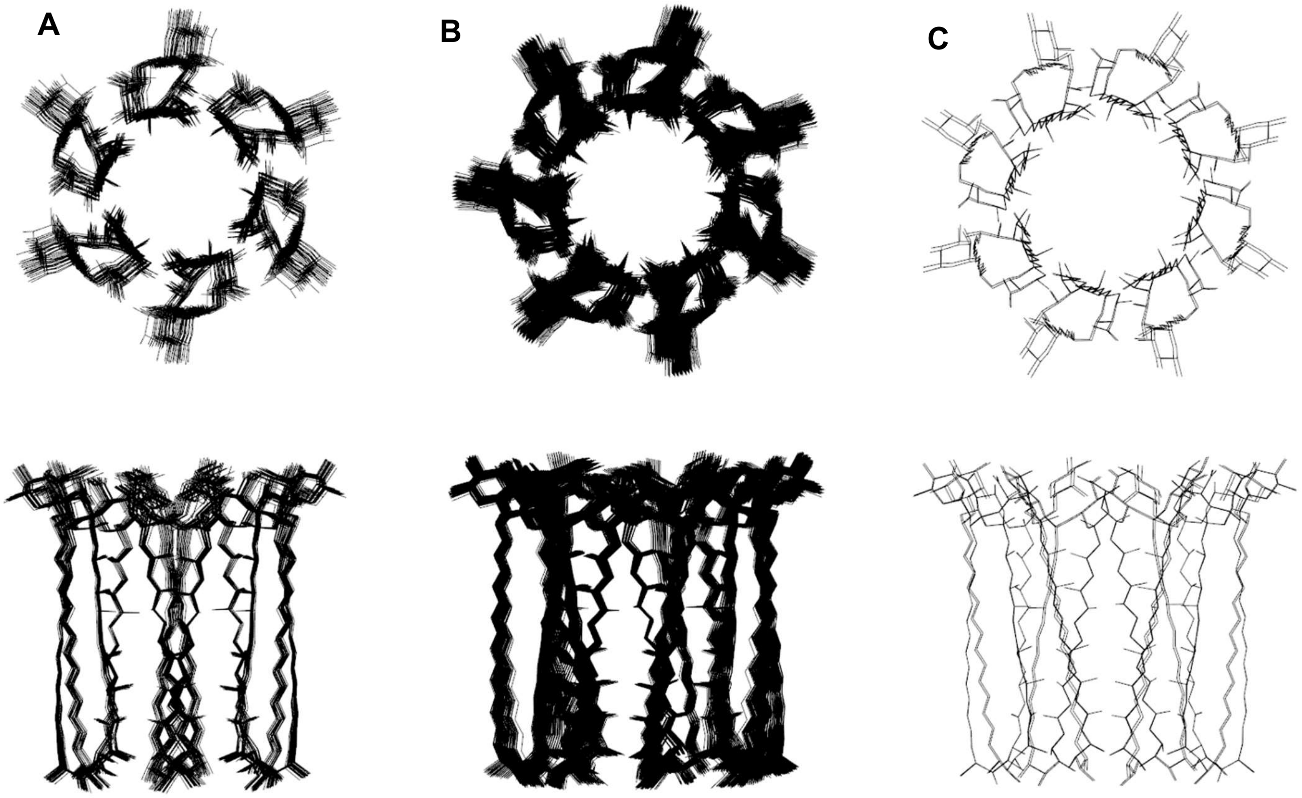

D Interatomic distances for hexamer, heptamer and octamer assemblies

n	hexamer (AmB$_6$)		heptamer (AmB$_7$)		octamer (AmB$_8$)	
	r_1 / Å	r_2 / Å	r_1 / Å	r_2 / Å	r_1 / Å	r_2 / Å
14-F/C41	6.7 - 7.1	9.3 - 9.8	6.5 - 7.1	8.6- 9.6	6.7 - 6.8	8.9
14-F/C1'	5.3 - 5.7	12.0-12.4	5.2 - 5.8	11.5-12.4	5.4 - 5.6	11.9
14-F/heptaene	11.6-12.2	15.9-16.3	11.5-12.1	15.7-16.4	11.7-11.8	15.9
32-F/C40	10.8-11.4	9.4-10.2	9.7-11.4	8.5-10.2	9.7	8.54
32-F/C26	12.6-13.4	10.3-11.0	12.3-13.4	9.6-10.9	12.3	9.4

Fig. S26. Validity of channel structure composed of six molecules, seven molecules, and eight molecules of AmB. In the fitting performed under the condition of Fig. S23, the seven parameters α, β, γ, n, R, p, and p' are varied by each 2°, 2°, 2°, 1, 0.2, 0.01, 0.01 increment, respectively, to obtain the parameter set that gave rise to the minimum RMSD values. **A** is the result of hexamer (six molecules, n = 6), **B** is the result of heptamer (seven molecules), and **C** is the result of octamer (eight molecules), when RMSD becomes close to the minimum value (0.028 - 0.030). Superpositions of all the assembly structures derived from the parameter sets are shown. **D** is a summary of the interatomic distances for each structure.

Values of interatomic distances obtained from solid-state NMR and MD simulations:

Table S5. ^{13}C-F interatomic distances measured by REDOR experiments and values from MD simulations (System VII-1). The interatomic distances differ between the front and back of the molecule and correspond to r_1 and r_2, respectively. The distance determined by REDOR measurement is shown in the minimum and maximum range of the structures shown in Fig. S26, and the best fit value is shown in parentheses. The same values are used for the graph in Fig. 4E. Details of MD simulation results on the structures of pentamer, hexamer, heptamer and octamer assemblies of AmB are presented in Figs. S36-S37.

Positions	r_1 / r_2	
	REDOR / Å	MD / Å
14-F / C41	6.5～7.1 (6.8) / 8.6～9.8 (8.9)	7.42±0.25 / 9.32±0.27
14-F / C1’	5.2～5.8 (5.5) / 11.4～12.4 (11.9)	6.42±0.12 / 12.7±1.5
14-F / heptaene	11.5～12.2 (11.6) / 15.7～16.4 (16.0)	12.18±0.15 / 14.30±0.11
32-F / C40	9.7～11.4 (11.2) / 8.5～10.2 (9.9)	9.38±0.07 / 8.62±0.10
32-F / C26	12.3～13.4 (13.2) / 9.4～11.0 (10.3)	10.24±0.05 / 12.22±0.15

UV-VIS and circular dichroism (CD) spectra to examine whether the channel structure changes depending on the AmB concentration in sterol-containing membranes:

The concentration of AmB in Erg-containing membranes (R_a= [AmB]/[lipids]) that significantly increases ion permeability is estimated to be 0.01 to 0.1 mol% in either fungal membranes or artificial bilayers (*16, 29*). There is a large concentration difference over 100 times between the concentration necessary for these AmB activities and that of the NMR experiments. Whether or not the structure of the AmB assembly changes in this concentration range was examined by UV-VIS and CD spectra with the lipid compositions similar to the NMR experiments, and the spectra thus obtained were compared with those in previous studies(*16, 29, 36, 40, 76-78*).

The UV-VIS spectra (Fig. S27) measured with large unilamellar vesicles (LUVs) consisting of the same lipid compositions as those of the NMR measurements gave rise to the characteristic spectra of AmB in Erg- or Cho-containing membranes (*76*). As for the Erg-containing membrane, the sharp absorption peak at 415 nm was observed at the same position in the range from R_a= 10^{-1}, which was the concentration for solid-state NMR, to R_a = 10^{-3}, which was the concentration in the antifungal assay. In the Erg vesicles, AmB was mostly present in the membrane by forming assemblies with Erg in this concentration range. However, the absorption on the short wavelength side (around 325 nm) and a band at around 413 nm was observed for the sterol-free and Cho-containing membranes (*27*). The absorption at 325-330 nm, which was observed for the sterol-free LUVs and for the Cho-LUVs as a shoulder peak, was reported to be due to AmB present as micelles or aggregates in aqueous phase (*40*). Increases in absorbance at Ra = 10^{-2} are due to the dilution of AmB density in membrane as generally observed for membrane-bound entities.

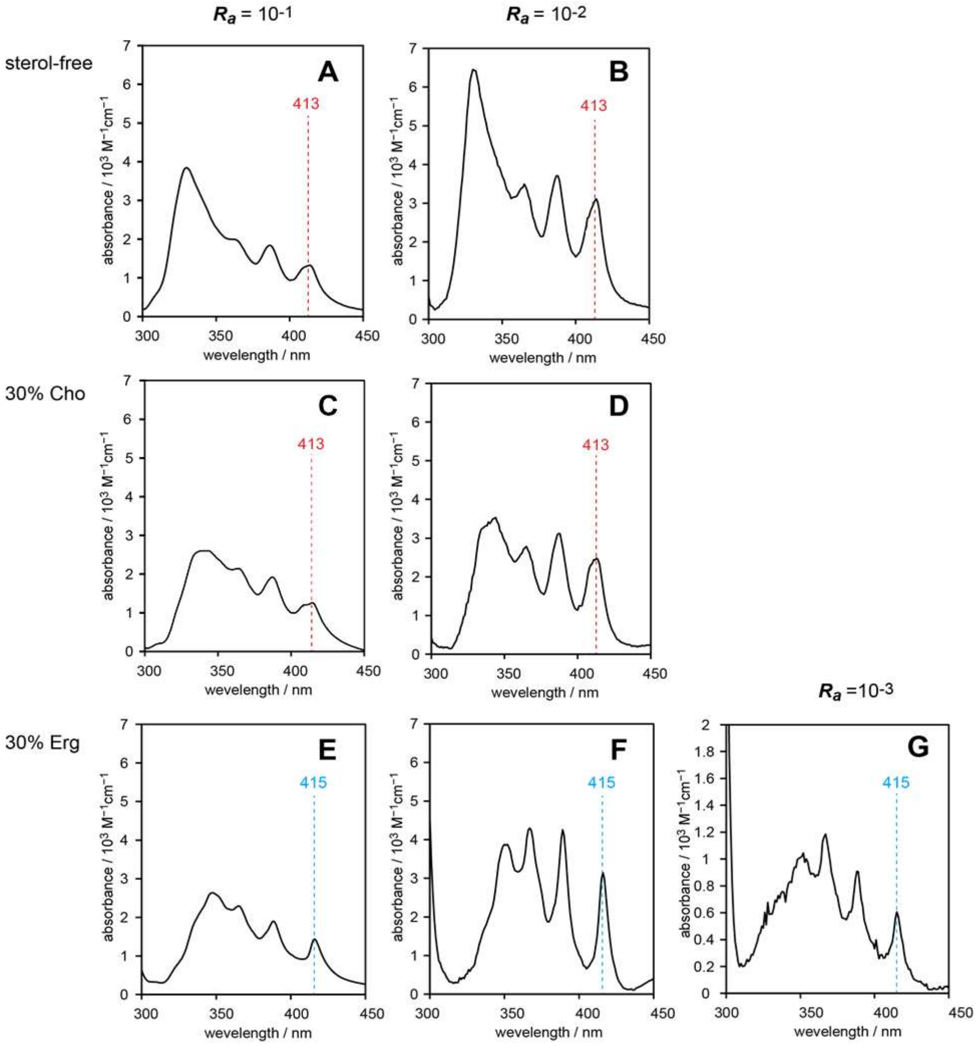

Fig. S27. UV-VIS spectra of AmB in membranes. The AmB concentration, R_a, and sterol contents in % depicted in the figure are those at the time of LUV preparation. After preparation of LUVs, AmB and sterol contents in the LUVs were determined as follows. **A**: $R_a = 0.43 \times 10^{-1}$, **B**: $R_a = 0.46 \times 10^{-2}$, **C**: $R_a = 0.56 \times 10^{-1}$ (32 mol% Cho), **D**: $R_a = 0.38 \times 10^{-2}$ (24 mol% Cho), **E**: $R_a = 0.60 \times 10^{-1}$ (25 mol% Erg), **F**: $R_a = 0.47 \times 10^{-2}$ (16 mol% Erg), **G**: $R_a = 0.53 \times 10^{-3}$ (19 mol% Erg). The concentration of AmB was calculated from the UV spectra after dissolving LUVs in DMSO, and the PC and sterol contents were determined by a Phospholipid C Test-Wako kit and Cholesterol E-Test Wako kit, respectively.

Next, the concentration-dependent change of the AmB assembly was examined by CD spectroscopy. The CD spectra in Fig. S28 were measured by changing the concentration of AmB in LUVs containing 10 mol% and 30 mol% Erg or Cho in POPC. In the spectra of Erg-containing LUVs, the positions of three negative peaks in the wavelength range longer than 350 nm were observed at the same positions regardless of the concentration of AmB. In the spectrum of 0.1 mol% AmB ($R_a = 10^{-3}$, panel I), light scattering caused by LUVs reduces the S/N ratio; the peak intensity ($\Delta\varepsilon$) was also attenuated because monomeric AmB partially occurring in the membrane due to the high dilution gave rise to positive peaks almost at the same positions (*36*).

The positive peak intensity near 325 nm indicates the presence of AmB that does not penetrate the membrane interior. The proportion of these unbound AmB molecules was slightly higher than that in the NMR measurements (see Figs. 1-E and S22) because the lipid/water ratios in the CD spectra were much lower, where micelles containing AmB are easily dispersed in water phase. At 10 mol% of AmB ($R_\mathrm{a} = 10^{-1}$, panel G), the AmB membrane concentration and lipid composition in the CD experiment was the same as those in the solid-state NMR experiment. Considering the characteristics of the CD spectra that sensitively reflect the association state of AmB molecules in membrane, the close similarity in peak positions on the CD spectra of different AmB concentrations (Fig. S28, G, H, I) implies that an interactions of the heptaene moieties in the AmB assemblies under the NMR conditions ($R_\mathrm{a} = 10^{-1}$) is very similar to that in the assemblies formed under the concentration of the antifungal assays ($R_\mathrm{a} = 10^{-3}$). Therefore, we considered that the structure of the AmB assembly under the NMR conditions largely reproduces that of the AmB ion channels responsible for the antifungal efficacy and ion-flux activity.

Vertut-Croquin et al. measured the CD spectra in Erg-egg PC membranes by changing the AmB concentration (R_a) from 0.01 mol% to 5 mol% under similar conditions to those used in our NMR experiments (*37*). They reported that AmB assemblies that were presumed to have channel activity were formed in this concentration range, and the change in the CD spectra was relatively small, particularly in the membranes with a high Erg content (20 mol%); the negative peak on the long wavelength side was observed at the same position even when the AmB concentration was varied. This result also shows that the arrangement of the heptaene moieties of AmB (that is, the higher-order structure of the AmB assembly) was unchanged over the wide concentration range.

Previous reports showed that the properties of AmB ion channels are significantly influenced by the way AmB was added to membranes (*30, 40*). In our experiments, AmB was added at the time of membrane preparation, which was different from the case that AmB was added via an aqueous medium to preformed vesicles, as in the case of drug administration or channel current recording. Whether this difference in the administration method of the drug affects the channel structure was examined by CD spectroscopy. As shown in Fig. S28H, a reported CD spectrum, where AmB was administered via the aqueous layer to the Erg-containing LUVs (*78*), was indistinguishable from the spectrum of the present experiment, where AmB was added at the time of LUV preparation. The observations indicate that AmB assemblies having very similar AmB arrangements are formed in membranes by these two ways in AmB addition.

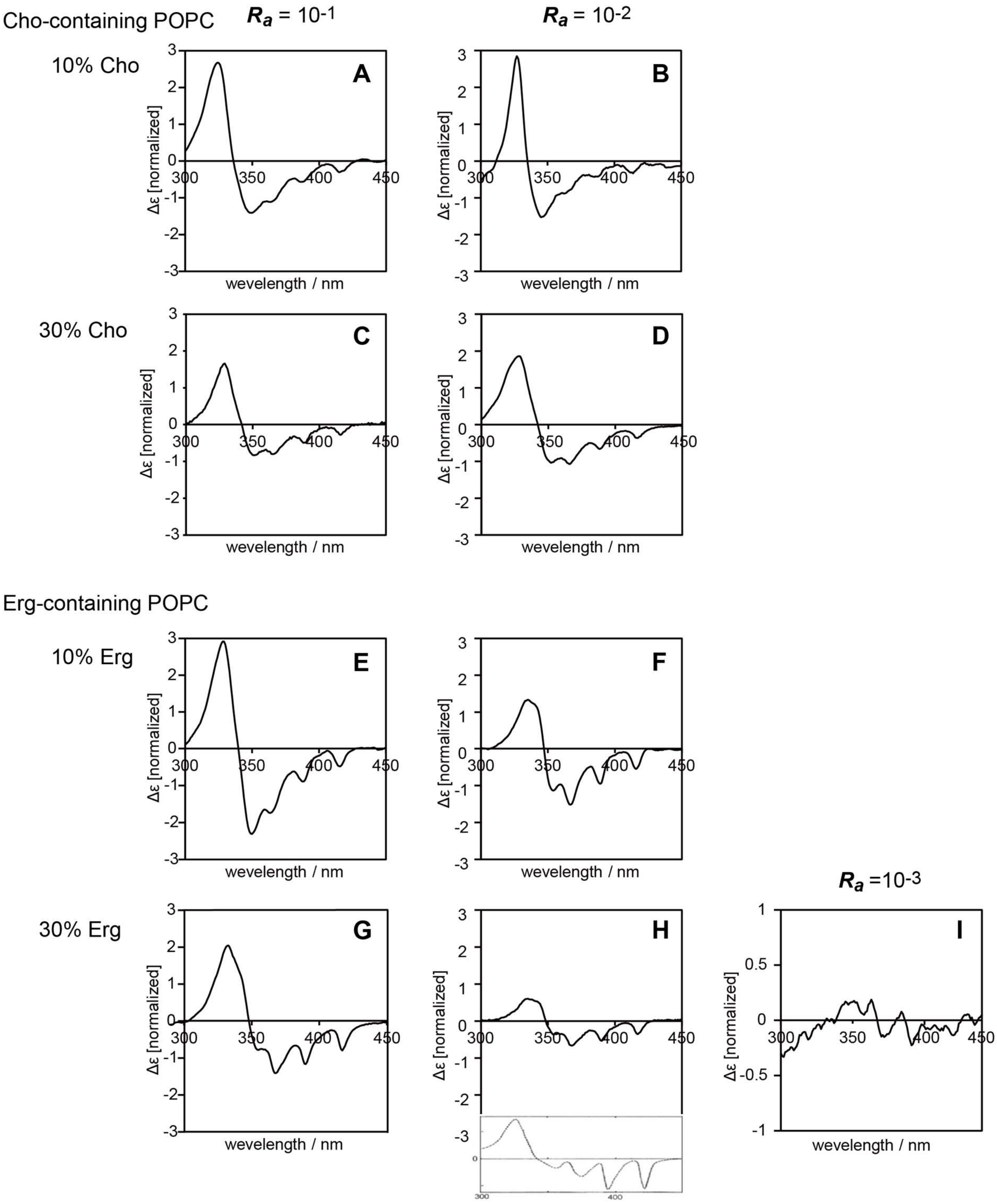

Fig. S28. Membrane concentration-dependent CD spectra of AmB in Cho-containing and Erg-containing PC membranes. A, B, E, and F are 10 mol% sterol/egg-PC, and C, D, G and I are 30 mol% sterol in POPC LUVs. The inset diagram of panel H is the CD spectrum in literature (*78*) in which AmB (R_a = 1 mol%) was added to preformed LUVs with the same lipid composition and AmB concentration as that in panel H. These two spectra are in good agreement despite that the administration methods are different. The AmB concentration and sterol content depicted in the figure are those at the time of preparing the LUV sample. The AmB content and sterol concentration of the final sample were determined as follows. AmB/lipid ratio (R_a) and sterol content after extrusion. **A**: $R_a = 0.67 \times 10^{-1}$ (19% Cho), **B**: $R_a = 0.32 \times 10^{-2}$ (13% Cho), **C**: $R_a = 0.56 \times 10^{-1}$ (32% Cho), **D**: $R_a = 0.38 \times 10^{-2}$ (24% Cho), **E**: $R_a = 0.62 \times 10^{-1}$ (21% Erg), **F**: $R_a = 0.28 \times 10^{-2}$ (11% Erg), **G**: $R_a = 0.60 \times 10^{-1}$ (25% Erg), **H**: $R_a = 0.47 \times 10^{-2}$ (16% Erg), **I**: $R_a = 0.53 \times 10^{-3}$ (19% Erg). The concentration of AmB was calculated from the UV spectrum after dissolving LUVs in DMSO, and the PC and sterol contents were determined by a Phospholipid C Test-Wako kit and Cholesterol E-Test Wako kit, respectively.

Higher affinity of Erg to AmB assembly than Cho supported by MD simulation:

We previously reported a structure-activity relationship for the AmB-sterol complex (*23, 76*) and considered that hydrophobic van der Waals (vdW) contacts between AmB and Erg stabilized the bimolecular complex. This idea was also supported by the present MD simulation performed for the AmB channel structure in the present study by replacing Erg with Cho; the detailed results are provided in Figs. S35 and S38. Compared with the AmB-Erg complex (Fig. S29), the interaction between AmB and Cho was unstable, where Cho was easily separated from the AmB assembly. On the other hand, the inner diameter of the AmB channels in the Cho membrane is quite similar to that in the Erg membrane (Fig. S29F). Thus, the difference in AmB activity between the two membranes is considered to be derived from difference in stability of the AmB channel. The synergistic effect of hydrogen bonds and vdW interactions that occur in fungal membranes containing Erg probably stabilizes the active ion channel complex and thus facilitate the formation of aggregates of channels (Fig. S32). On the other hand, in mammalian cell membranes containing Cho, conductive AmB channels are formed to some extent. The aggregates of channels are, however, unlikely to occur in the Cho membrane because of a short lifetime of the channel assembly.

A

Sample #	(OH-OH distance)/Å	
	Erg	Cho
1	2.8±1.3	10.5±1.8
2	2.6±1.0	3.6±1.6
3	2.4±0.6	3.2±1.6
4	2.8±0.8	2.6±1.2
5	2.7±1.0	3.1±1.4
6	2.3±1.0	3.1±1.6
7	1.3±0.9	3.6±2.0
Average	2.6	4.2

B

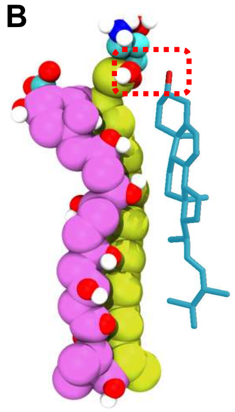

C

D

E

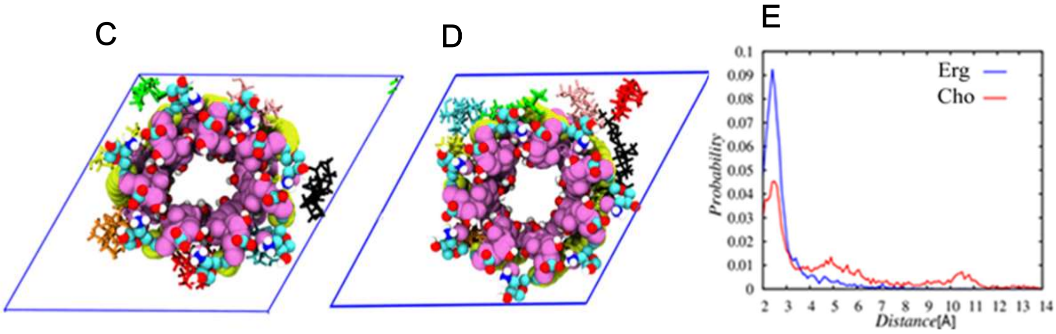

F

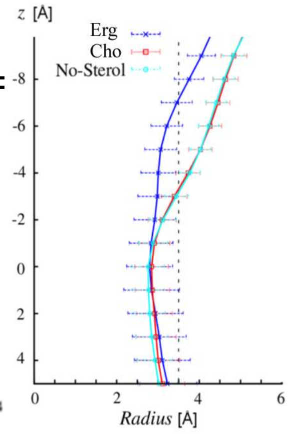

Fig. S29. MD simulations revealed that Erg has much higher affinity for the AmB assembly than Cho. The simulations were performed for the simulation time of 1 μs with lipid composition of AmB/Sterol/POPC = 7: 7: 16. Table **A** shows the interatomic distance (red dotted line in panel **B**) between the oxygen at the 2' position of mycosamine and the oxygen atom of the sterol's 3-position in the Erg-containing membrane and Cho-containing membrane. The table shows the average over the probability distribution of distance. From this distance, Erg was shown to have a high binding probability while Cho has low binding probability (values in red). **C** and **D** are the top views of seven molecule AmB channels of the Erg and Cho membranes, respectively, where seven differently colored molecules of the sterol are partly incorporated into the AmB channel complex. **E** Distribution of the distances between sterol and the mycosamine moiety in Table A. **F** Distribution of pore radii of AmB channels along the pore axis in Erg, Cho, and sterol-free membranes. Note that the Cho membrane and the sterol-free membrane are very similar. This result implies that the binding of a few Cho molecules does not significantly affect the structure of the AmB assembly. See Figs. S35 and S38 for details.

Comparison of the single length channel and the double-length channel with the heptamer and octamer AmB assemblies:

We compared channel pore inner diameters to deduce which of the four structures of ion channels, different in heptamer/octamer and single-length/double-length as suggested in the previous and current studies (Fig. 1BC and Fig. S30), best reproduced the ion channel function.

In the previous study (*26*), which was not based on the present structure of the AmB channel, MD simulations were tentatively performed for a heptamer assembly. Therefore, we re-examined the stability of the single-length heptamer channel obtained in this study. When the present single-length channel was compared with the double-length assembly consisting of 14 molecules of AmB (cited from Reference *26*), a remarkable difference was observed as shown in Fig. S30A. First, the average radius of the bottom half of the double-length assembly is significantly narrower than the present channel (green), suggesting that the double assembly cannot function as an ion-conducting channel. Second, the large fluctuation of the lower AmB molecule of the double-length assembly implies that the stability of this channel is lower than that of the single-length channel. Stabilization of the single-length channel can be explained by the aggregation of the channel assembly as discussed later (Figs. S32, S33, S43, and S44).

Next, we repeated a similar examination for 2x8 AmB channel in the double-length assembly, starting from four different initial configurations. Each initial configuration contained the same structure of AmB_8-Erg_8 in a single-length channel system, though copied and rotated to have mycosamine moiety of both octamers oriented outward of the membrane. A simulation system was composed of 16:48:112 (1:3:7) AmB/Erg/POPC molecules, hydrated with 8430 water molecules. The constructed channel was embedded in lipid membrane using the CHARMM-GUI (*47-49*) four initial configurations and a final snapshot after 500 ns-MD were given in Fig. S47. As found in the final snapshot, the channel was deformed largely typically within 100 ns. Pore size analysis along the channel is given in Fig. S30B. As is the case with the heptamer assemblies, the average radius of the upper half of the double-length assembly (Fig. S30B, left) is significantly narrower than the single-length channel (right), suggesting that the double assembly is too unstable to act as an ion-conducting channel. The large fluctuation of the half octamer portion of the double-length assembly implies its lower stability in the bilayer.

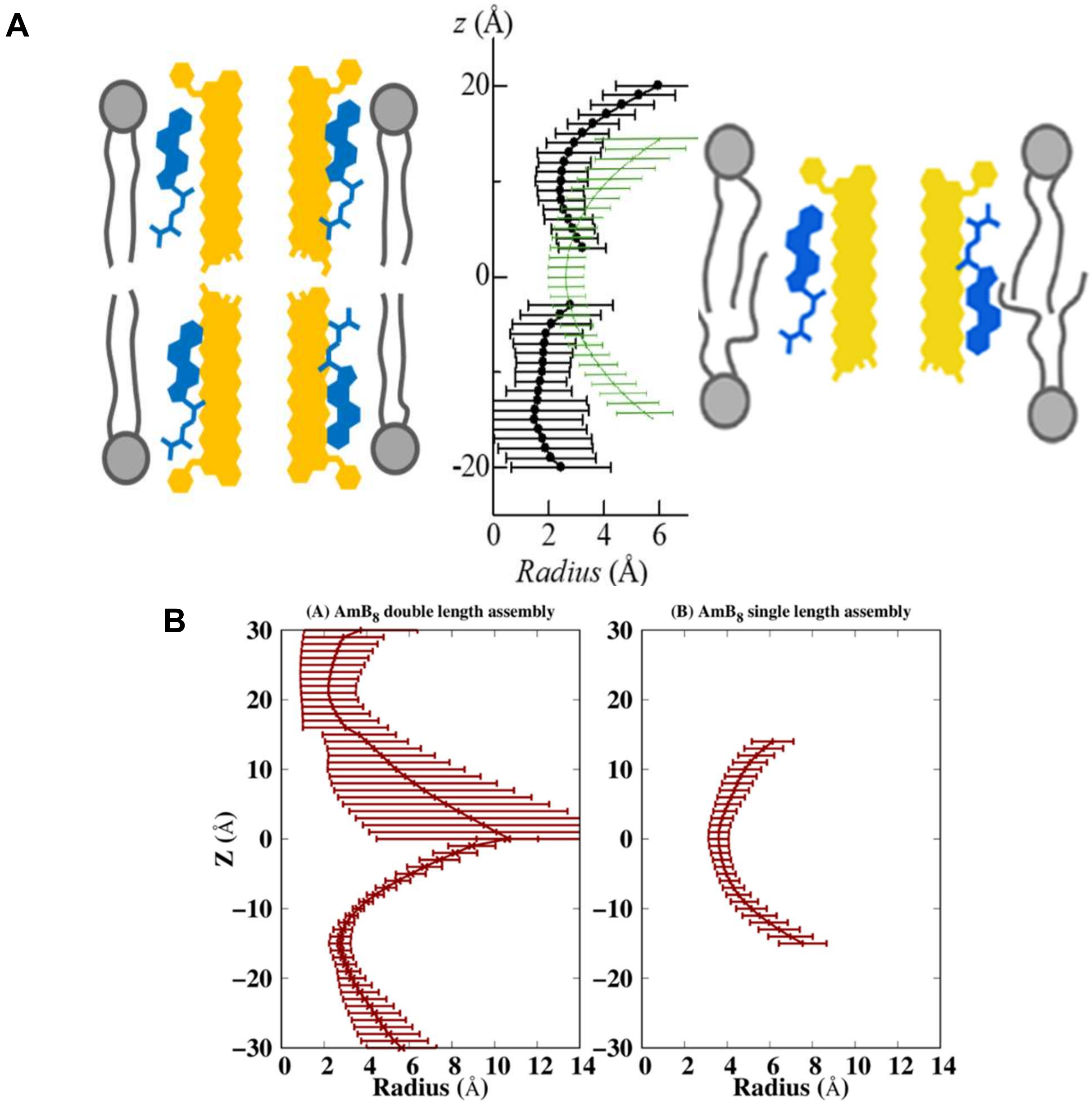

Fig. S30. Model diagrams of the double-length channel (left) and single-length channel (right) and distribution of pore radii along the channel pore surrounded by heptamer or octamer assemblies.

(A) Channel radius profile along the pore axis calculated from the last 500 ns MD trajectories. Black: double-length AmB complex in AmB/Erg/POPC 14:42:98 (*26*). Green: single-length AmB complex in the POPC-Erg bilayer obtained in this study (Fig. 1B). The present result confirmed that the minimum radius of the single-length channel is significantly larger than that of the double-length channel. (B) Pore radius profiles of AmB$_{16}$ double length assembly (left) shown in Fig. 1C and AmB$_8$ single length assembly (right) along the membrane normal calculated from the 2-10 µs MD trajectories in the POPC-Erg bilayers. The error bars denote the standard deviations.

Comparison between the channel conductance of MD-derived AmB assemblies and previous results of single-channel recording:

From previous channel recording studies, the conductance of a single channel consisting of AmB and Erg in the DPhPC membrane is 14–16 pS with a typical value of 14.5 pS (*30*) as described in Fig 4F. This value corresponds to the passage of 9.4 to 10.7 K^+ ions per channel for 1 μs under the applied electric field of 0.01V/nm. Conductance of the ion channel estimated by MD simulation for the heptamer AmB assembly under the similar conditions agrees well with the experimental value (Fig. 4F). In addition, the conductance of the hexamer and octamer channels showed significantly small and large values, respectively. If the hexamer channels coexist with the heptamer channels, we consider that the contribution of the hexamer channels to the total ion current should be extremely small. On the other hand, if octamer channels are significantly formed, the single channel current should be much larger than the experimental results.

Previous channel recording was largely conducted by using DPhPC as a base lipid. We examined the stability of a single AmB channel in DPhPC bilayers using MD simulation. As shown in Fig. S40 and S41, a single (non-aggregated) channel appears to be stabilized in the upper interior of DPhPC-Erg bilayers as compared to the POPC-Erg bilayers, where the aggregates of the channels are easily formed even with highly diluted AmB. DPhPC molecules surrounding the AmB7 channels do not appear to be as deeply interdigitated as those of POPC (Fig. S41B versus Fig. S36C), which may contribute considerably to the stability of the isolated channel assembly. Thus, under the high dilution conditions, DPhPC is a suitable medium to obtain an isolated AmB channel both for current recording and MD simulation.

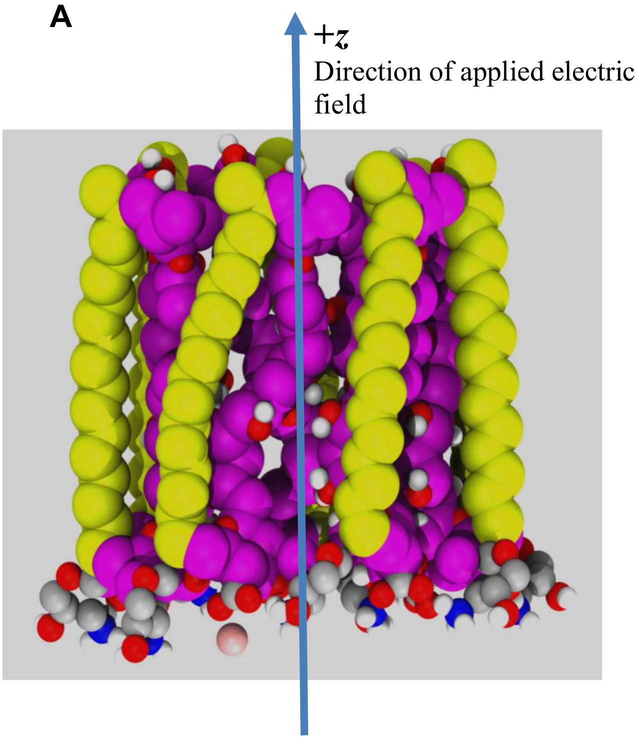

B

Sample #	K^+		Cl^-	
	+z	-z	+z	-z
S1	18	1	0	1
S2	30	0	1	0
S3	24	0	0	0
S4	15	0	0	6
S5	0	0	0	0
S6	2	0	0	5
S7	43	1	1	4
S8	5	1	0	0
S9	19	1	4	1
S10	35	1	1	14
S11	15	1	0	4
S12	7	0	0	0
S13	0	0	0	0
S14	18	0	0	8
S15	15	0	0	4
S16	1	0	0	0
Average	15.43	0.37	0.43	2.94

Fig. S31. MD channel trajectory and channel inner diameter distribution (see Videos 1 and 2 for MD ion permeation). A: The pink ball is at the K^+ position that is entering the channel. Note that the headgroup with the mycosamine moiety is oriented downward in the bilayer (opposite to the direction of AmB assembly in the manuscript and videos). **B**: The number ions which passed through the heptamer AmB channel (System VII-7) in the DPhPC-Erg bilayer from 16 independent MD runs. When the number of K^+ and Cl^- ions passing through the heptamer AmB channel was estimated under the conditions of 0.01V/nm and 2 M KCl by MD simulation, the heptamer AmB channel passed 15.06 of K^+ ions and 2.51 of Cl^- ions per μs on average, and this ion selectivity was in good agreement with previous experimental results (*30, 43*). See also Figs. S39, S40 and Table S9 for details of the MD simulations.

NMR and MD results suggest that the AmB-Erg channels are aggregated:

The REDOR experiment in Fig. 3C implied the aggregation of AmB-Erg assemblies; it was found that the dephasing values of 32-F/C26 were all slightly larger than the theoretical curve, which meant that their atomic distance between channels was shorter than the theoretical curve obtained from the intermolecular distance within the assembly. The 32-F and C26 positions reside in the heptane moiety, which locates in the outer side of the channel assembly, and allow C26 to be closer to 32-F, especially when an antiparallel pair of the assemblies comes close each other (Fig. S32A). In previous studies, we have extensively performed REDOR measurements with lipid bilayer membranes containing AmB. Then, we obtained several results suggesting that the assemblies formed by AmB-Erg are close to each other. For example, in the ^{13}C-^{31}P REDOR experiments, significant dephasing effects were observed between the ^{31}P nuclei of DMPC (or DSPC) and the ^{13}C signals of AmB (*79*). Since phospholipids in contact with membrane-bound entities such as peptides usually have a short residence time in the order of microseconds, REDOR dephasing is rarely observed. Therefore, the ^{13}C-^{31}P REDOR result implies that phospholipids were trapped in the interstitial space between channels, as shown in Figs. 5B and S32.

When MD simulation was performed with AmB assemblies (seven molecules) arranged at equal intervals, they more frequently came closer to each other than when the channels were randomly distributed (Fig. S32A). This is because peripheral interdigitation of lipids is required to incorporate the single-length assemblies into the lipid bilayer (Fig. 5, etc.), and more deeply interdigitating lipids and higher curvature of the surrounding membrane become necessary to incorporate isolated (not aggregated) assemblies. In other words, the aggregation of the channel assemblies is energetically favorable to avoid the interdigitation of lipid chains that more abundantly occurs around the isolated assembly.

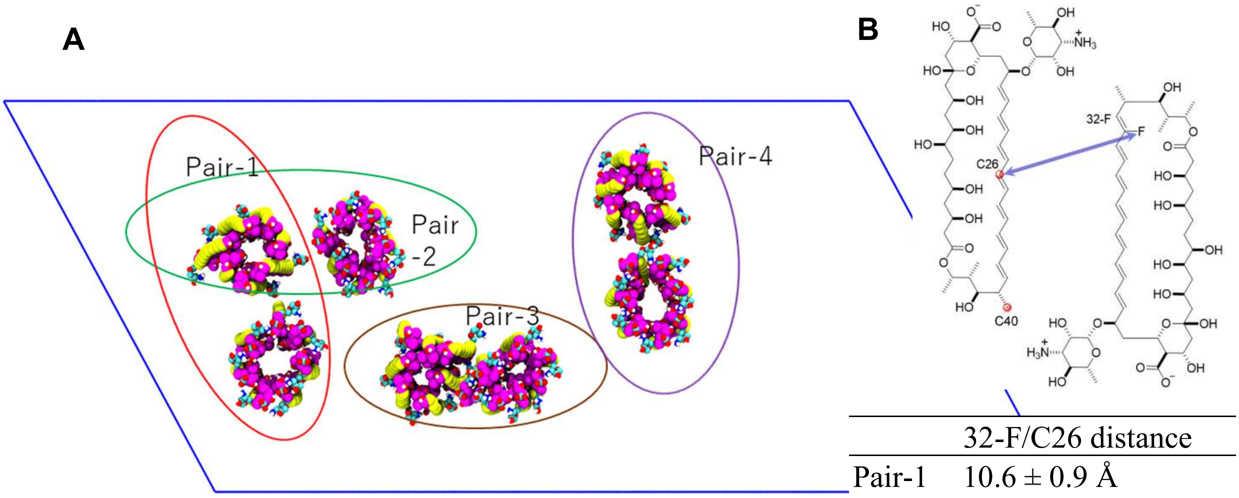

	32-F/C26 distance
Pair-1	10.6 ± 0.9 Å
Pair-2	10.6 ± 0.7 Å
Pair-3	6.3 ± 0.6 Å
Pair-4	10.5 ± 1.0 Å

Fig. S32. AmB channel clustering observed by MD simulations with the antiparallel channel-channel arrangement. MD simulations show that 32-F and C26 come close in some of the antiparallel assembly pair. The inset table shows the inter-assembly distances of 32-F/C26 for the four pair of the assemblies with the antiparallel orientation. The close proximity of 32-F/C26 as seen in the Pair-3 may cause their higher REDOR dephasing values than those deduced from the distance within an assembly (Fig. 3C). Colors in molecules: AmB is in pink for the hydrophilic group and in yellow for the polyene group. POPC and Erg are not shown for clarity. See Fig.S44 for details in MD simulation.

AmB binds more efficiently to membranes containing sterol, either Erg or Cho (*80*), so the equilibrium at step **a** of Fig. S33 also shifts toward the formation of AmB assemblies in sterol-containing bilayers. In the Erg-containing membrane, the channel assembly is stabilized by Erg binding, and thus, a large aggregate of the assemblies occurs through step **b** so as to reduce the degree of interdigitation of surrounding lipids and to relax higher curvature around the assembly. Once formed, the large aggregate is stable and therefore exhibits ion channel activity for long time. However, in the Cho membrane, the channel structure is not sufficiently stabilized due to the small number of Cho that binds to the channel assembly (see Fig. S29). A high concentration of AmB without sterols results in formation of phospholipid-free clusters, which partly come off the membrane (step **c**). Based on the assumption, it is presumed that AmB has a strong tendency to form high-density aggregates within Erg-containing membranes even in low membrane concentrations of AmB (AmB/phospholipids). This may be one of the reasons that a similar structure of an AmB channel assembly is maintained regardless of the concentrations of AmB, as shown in the text (page S50-S52) and Figs. S27 and S28

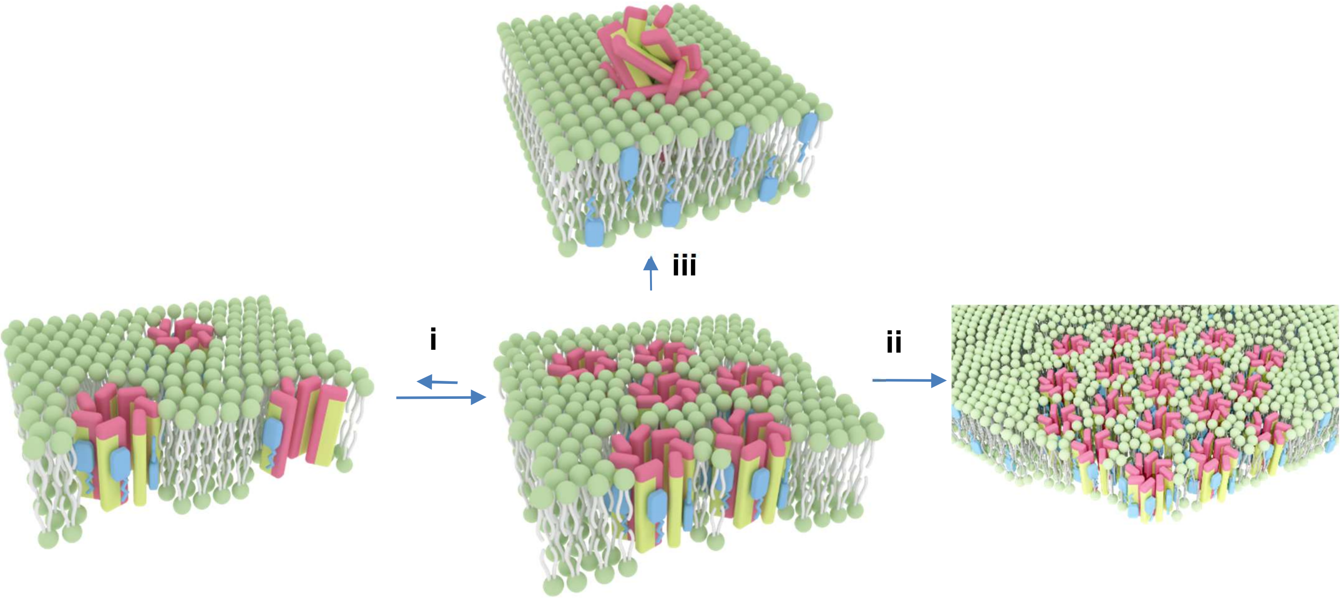

Fig. S33. Proposed aggregated states of AmB channel assemblies in the Erg and Cho membranes. In Erg-membranes, large aggregates of AmB assemblies tend to form, as shown in steps **i** and **ii,** while in Cho-membranes, AmB assemblies cannot form stable assemblies within membrane and partly form AmB-only clusters, as shown in step **iii**. Although the assemblies in the same orientation (parallel arrangement) are drawn in the figure, it is assumed that similar aggregation occurs with the antiparallel arrangement when channel assemblies reside in Erg-containing membranes as seen in Figs. 5B and S44.

Previous structure-activity relationship results can be accounted for by the present channel structure:

In the field of medicinal chemistry, extensive investigations have been conducted to modify the AmB structure to enhance its efficacy and reduce adverse effects. Some of these structure-activity relationship results can be explained by the present channel structure. Since the functional groups of AmB are important for stabilizing the assembly structure by electrostatic and hydrogen bonding interactions (Fig. 4D), we investigated their effects on K^+ channel activity using MD simulations. The results on the methyl ester of AmB (AME), which is a biologically active derivative, and *N*-acetyl-AmB, which largely loses ion channel activity, are described below as typical examples.

1) **AME, effects of 41-COOH methylation**: Numerous previous papers have reported that AME retains biological activities, including antifungal and ion channel activities (*42, 43*). In the MD simulation, AME forms a stable assembly with a pore similar to that of AmB (Figs. S34B, S45). Under the experiment-mimicking conditions (1 M KCl, membrane potential 0.1 V, POPC/Erg bilayers), the K^+ conductance of a heptamer AME channel was 3.5 pS, which agrees with the previously reported conductance of 4.5 pS for biomembrane (*81*) (Fig. 4F and Table S12).
2) ***N*-Acetyl-AmB, effects of blocking the amino group**: It is well known that *N*-acetyl-AmB shows almost no channel activity (*42*). This experimental fact was clearly supported by the MD simulation based on this channel structure. The fluctuation of the pore radius during the simulation (Fig. S34B) was much larger than that of AmB and AME. This observation indicates that the channel stability of *N*-acetyl-AmB is very low, therefore, suggesting that channel assemblies with ion permeation activity are hardly formed in membranes (Fig. S45).

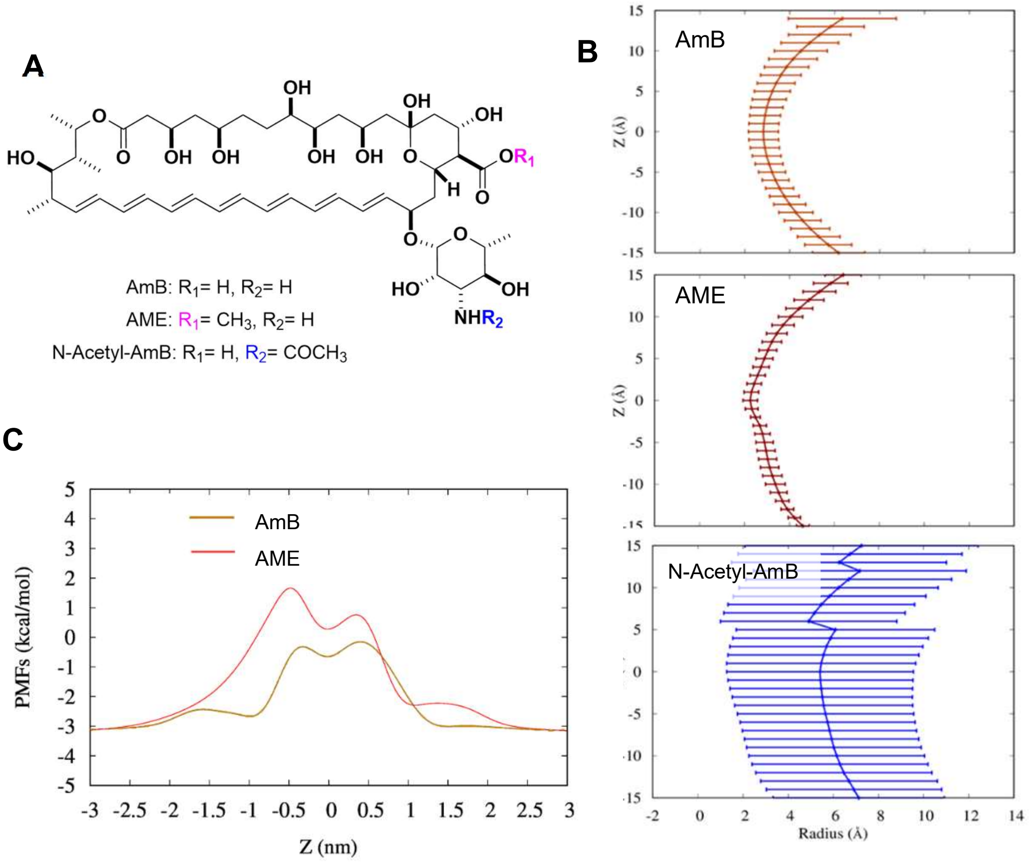

Fig. S34. Summary of the cture-activity relationship of AmB: MD simulations of heptamer channels consisting of AME and N-acetyl-AmB. A: Chemical structures of AME and N-Acetyl-AmB. **B**: Profile of the channel inner radii along the channel pore calculated by MD simulations based on the NMR-derived symmetric assembly of AmB. The error bars denote the standard deviations. **C**: Potential of mean force (PMF) of K^+ ion measured according to the channel model. See Fig. S45 and Tables S11/S12 for details.

II. Detailed results and interpretations of MD simulations

Stability of pentamer, hexamer, heptamer and octamer channels in Erg (and Cho) bilayers:

We need to confirm whether the AmB assembly constructed by NMR and MD results forms an ion-conducting channel. Before reproducing the results of previous channel recording experiments by MD simulation, it was necessary to examine whether AmB had an ion-conducting structure under the conditions of NMR and UV-VIS/CD measurements. This is because the channel recording experiments have usually been carried out under the conditions of high concentration KCl solution using DPhPC bilayers, and it is not possible to reproduce these conditions in the NMR experiments. Therefore, MD simulation was performed using a POPC-Erg membrane in the presence of a low concentration of KCl without applying an electric potential. One-μs MD simulations for each AmB assembly (AmB_5, AmB_6, AmB_7 and AmB_8) has been repeatedly performed from ten different initial structures. The AmB assembly structures were stable for all these systems, when Erg molecules were included (Fig. S35). The stability of these assemblies is mainly explained by two intermolecular interactions within the AmB channel; the electrostatic interaction between 3'-NH_3 and 41-$COO^−$ group of AmB molecules and the hydrogen bonds between 15-OH and 2'-OH group of AmB molecules. The values of these interaction energies are provided in Table S7, which validated the formation of stable AmB assemblies, the inter molecular electrostatic interaction between 3'-NH_3 and 41-$COO^−$ is significantly responsible for the AmB assembly. The interdigitated arrangement of POPC is also responsible for the AmB channel stability as we will discuss below. As seen in panel D, AmB assemblies in the presence of Cho sometimes collapse into a non-conductive form.

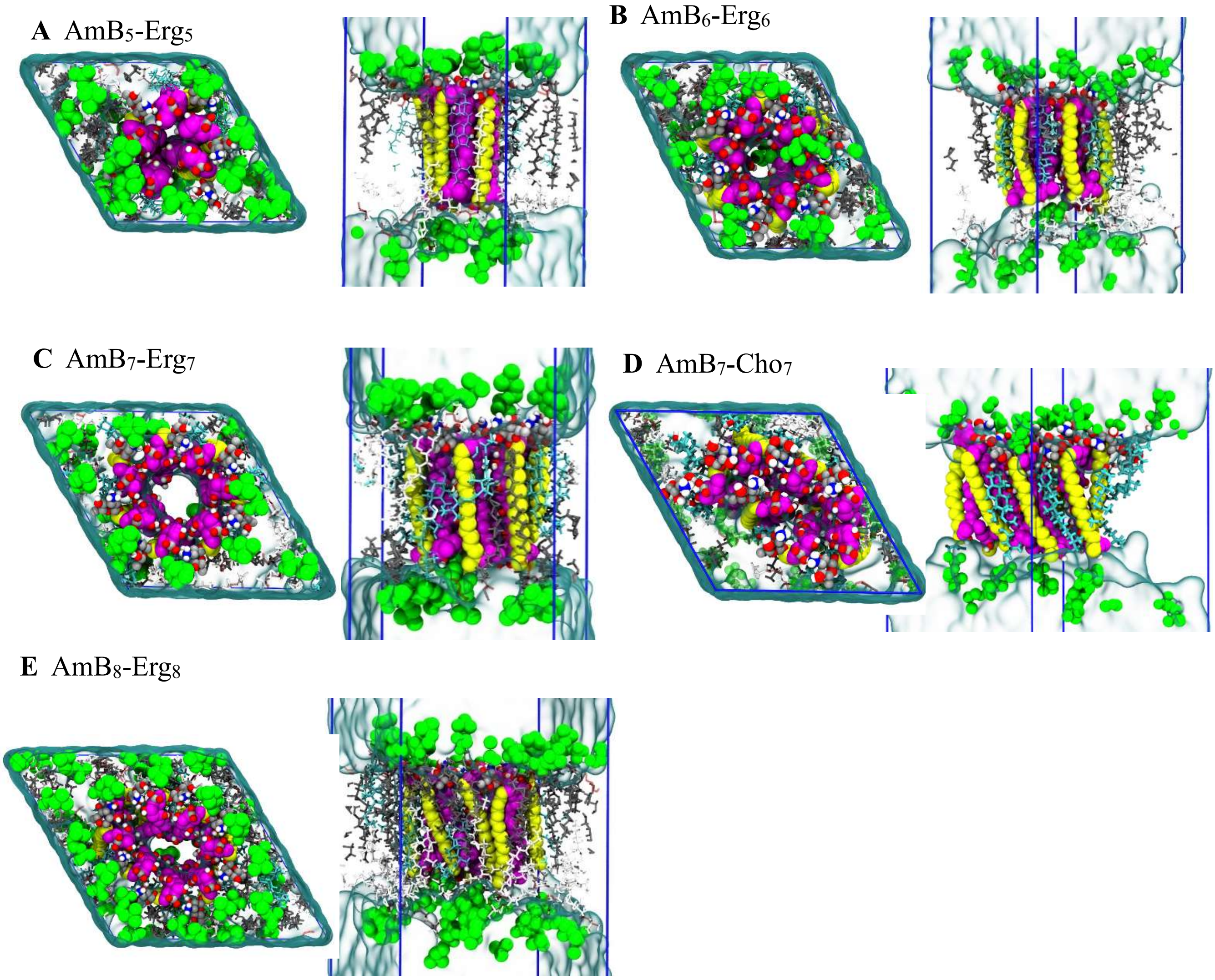

A AmB_5-Erg_5

B AmB_6-Erg_6

C AmB_7-Erg_7

D AmB_7-Cho_7

E AmB_8-Erg_8

Fig. S35. The final configuration after 1μs MD run of System-V (**A**), System-VI-1 (**B**), System-VII-1 (**C**), System-VII-2 (**D**), and System-VIII-1 (**E**) in the POPC-Erg bilayers. The color code of AmB/Erg (Cho) and the presentation are the same as in Fig. S2. The color code of POPC is the same as in Fig. S3.

Distribution of POPC headgroups and terminal methyl groups along the bilayer normal:

The distribution of several selected atoms along the bilayer normal obtained from MD simulation are shown in Fig. S36. The probability distribution for the lipid atoms was calculated only for the neighboring lipid molecules within 5 Å of the AmB channel. We noticed that the distributions of the acyl-chain terminal positions of the upper and lower leaflets overlapped with each other, suggesting the membrane thinning due to the partial interdigitation of lipid molecules caused by the stabilized AmB assembly in Erg-containing lipid bilayers.

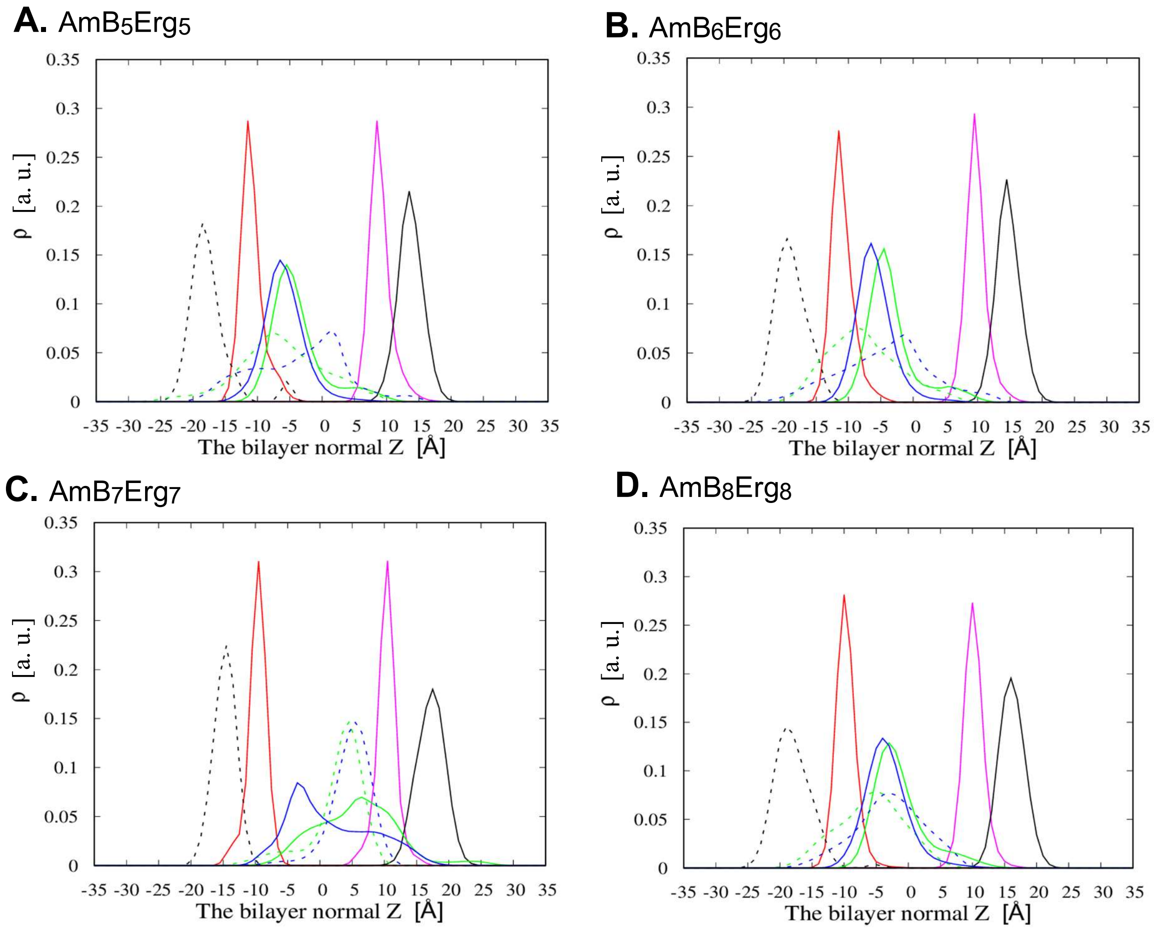

Fig. S36. Probability distribution (ρ) of selected atoms along the bilayer normal of POPC-Erg bilayers calculated from the ten 1μs MD trajectory of the AmB assembly. The probability of lipid atoms was calculated for the neighboring lipids within 5 Å of the AmB assembly: black for phosphorus of the POPC headgroup, blue for the carbon of a terminal methyl group (*sn-1*), and green for the carbon of a terminal methyl group (*sn-2*). Solid and dashed lines indicate lipids in the upper and lower leaflets, respectively. Red and magenta lines correspond to the C1' and C40 positions of AmB, respectively. (**A**) System-V (**B**) System-VI-1 (**C**) System-VII-1, and (**D**) System-VIII-1. Note that the AmB head group is in a negative position on the *Z* axis parallel to the bilayer normal (see Fig. S41D).

Ion channel activity is explained by the pore size and stability in POPC-Erg bilayers:

To confirm the ion channel activity of the heptamer assembly under the NMR conditions, we have carried out 10 μs MD simulations for AmB_5 to AmB_8 channel with 0.15M KCl salt concentration (the System-V, VI-1, VII-1, and VIII-1) in POPC-Erg bilayers. We computed the number of ions (K^+ and Cl^-) passing through the channel. These numbers are given in Table S6.

Table S6: Number of the ions which passed through the AmB channels with 0.15 M KCl in the POPC-Erg bilayers.

Sample #	**System-V** **AmB_5**		**System-VI-1** **AmB_6**		**System-VII-1** **AmB_7**		**System-VIII-1** **AmB_8**	
	K^+	Cl^-	K^+	Cl^-	K^+	Cl^-	K^+	Cl^-
S1	0	0	0	0	1	0	36	4
S2	0	0	0	0	0	0	12	3
S3	0	0	0	0	16	0	70	7
S4	0	0	0	0	0	0	6	4
S5	0	0	0	0	1	0	7	0
S6	0	0	0	0	11	2	11	2
S7	0	0	0	0	8	1	54	8
S8	0	0	0	0	11	1	55	12
S9	0	0	0	0	1	0	52	3
S10	0	0	0	0	5	0	69	14
Average	0	0	0	0	5.4	0.4	37.2	5.7

No ions passed through AmB_5 and AmB_6 channels during the MD simulations. It is evident that these channels are inactive in terms of ion conduction. On contrary, we detected ion permeation through AmB_7 and AmB_8 channels. Particularly, AmB_8 is a highly active ion channel. Fig. S37 plots the pore radius profiles of these channels as a function of z position along the pore axis. The AmB_5 and AmB_6 channels have smaller pore radii compared to AmB_7 and AmB_8 channels. Only dehydrated ion permeates through the channel in these systems, and only AmB_7 and AmB_8 channels give a large enough pathway for hydrated K^+ and Cl^- to go along with. Also, the difference between K^+ and Cl^- may be explained by the difference of the size of hydrated ion.

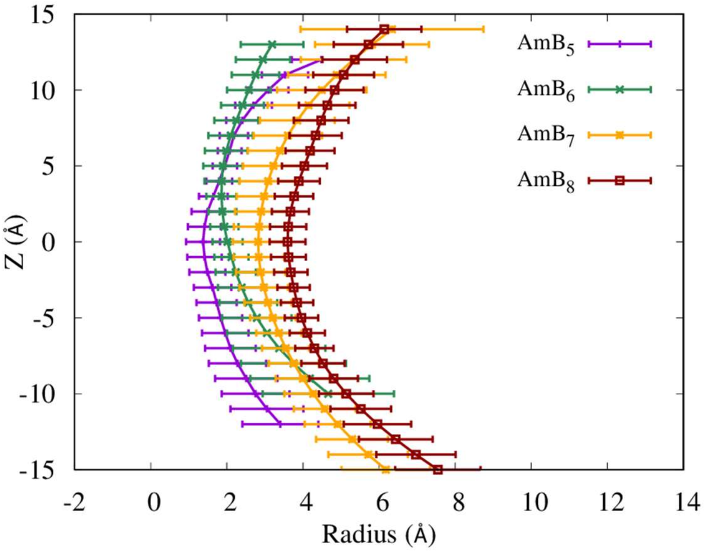

Fig. S37. Pore radius profiles of AmB channels along the membrane normal calculated from the 10 μs MD trajectories in the POPC-Erg bilayers. The error bars denote the standard deviations.

Table S7: Coulombic (Coulomb) and Lenard-Jones (LJ) contribution to the interaction energies between AmB-AmB and AmB-Erg molecules in the POPC-Erg bilayers.

Sample #	Interaction energies [kJ/mol]		
	Coulomb	LJ	Total
15th-OH_{AmB}-2'-OH_{Mycos}			
System V AmB_5-Erg_5	-34.8	-0.1	-34.9±4.2
System VI-1 AmB_6-Erg_6	-47.4	-0.1	-47.5±6.2
System VII-1 AmB_7-Erg_7	-65.1	-0.2	-65.3±4.6
System VIII-1 AmB_8-Erg_8	-59.7	-0.1	-59.8±4.2
3β-OH_{Erg}-2'-OH_{Mycos}			
System V AmB_5-Erg_5	-21.4	-0.0	-21.4±4.4
System VI-1 AmB_6-Erg_6	-49.5	0.13	-49.6±8.0
System VII-1 AmB_7-Erg_7	-45.4	-0.1	-45.5±3.6
System VIII-1 AmB_8-Erg_8	-40.8	-0.1	-40.9±3.2
3'-NH_3-41-COO^-			
System V AmB_5-Erg_5	-84.7	5.0	-79.7+6.3
System VI-1 AmB_6-Erg_6	-107.5	6.7	-100.8+6.2
System VII-1 AmB_7-Erg_7	-121.3	7.4	-113.4±5.2
System VIII-1 AmB_8-Erg_8	-124.8	7.9	-116.9±3.6
AmB_7-Cho_7			
System VII-2 15th-OH_{amb}-2'-OH_{Mycos}	-71.6	-0.2	-71.8±3.9
System VII-2 3β-OH_{Cho}-2'-$OH_{Myc\text{-}os}$	-35.1	-0.1	-35.2±3.5
System VII-2 3'-NH_3-41-COO^-	-134.8	8.8	-125.9±2.4

Preferential binding of AmB with Erg explains the pore stability:

The final configurations after 1μs-MD runs of AmB-Erg$_7$ (System VII-1) and AmB-Cho$_7$ (System VII-2) are shown in Fig. S35. We observed stable AmB-Erg and unstable AmB-Cho complexes. The different stability of the complexes is explained by the difference of hydrogen bonding interaction energies between the hydroxy group of Erg/Cho (3β-OH) and the hydroxy group of mycosamine of AmB (2'-OH) as suggested previously (*29, 82*). These interaction energies are provided in Table S8. For Erg, the interaction energy was -45.5±3.6 kJ/mol, while for Cho, the value was -35.2±3.5 kJ/mol, indicating that Erg more strongly interacted with AmB than did Cho. To verify the strong association of AmB with Erg, we also computed radial distribution function (g) of 3β-OH groups of Erg/Cho around 2'-OH group of AmB (Fig. S38). The intensity of the first peak for Erg is much higher than that of Cho. Therefore, Erg bound to the AmB channel more strongly than did Cho. In the case of Erg, the second peak is sharp and located within 4Å. For Cho, the broader second peak is observed. This indicated that Erg located closer to the AmB as compared to Cho.

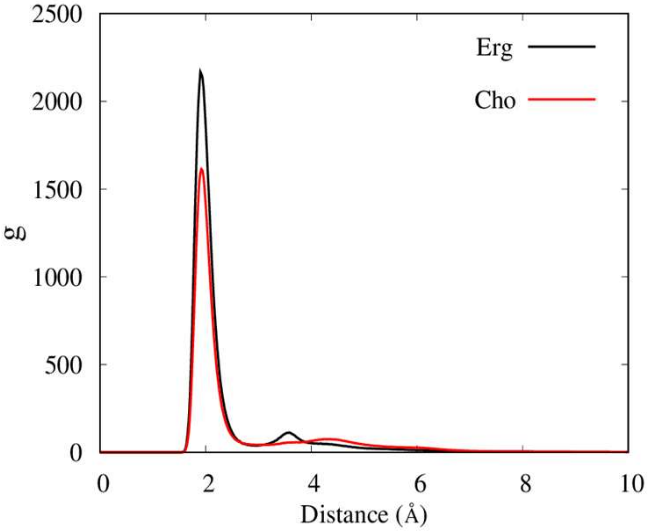

Fig. S38. Radial distribution function (g) of 3β-OH groups of Erg or Cho around 2'-OH group of AmB in POPC bilayers.

Higher Stability of AmB channels in DPhPC bilayers at the lower AmB/lipid ratio:

We evaluated the channel activity (ion conductivity) of AmB$_6$ (System-VI-2), AmB$_7$ (System-VII-7) and AmB$_8$ (System-VIII-2) channels in DPhPC bilayer membranes. The equilibrated structures of these channels (after 100 ns MD simulations) are shown in Fig. S39. In all these cases, the structural stability of AmB channels were high, and the AmB channel belonged to the upper leaflet of DPhPC bilayer. The mycosamine group of each AmB molecule contains two hydroxy groups (2'-OH and 4'-OH, Fig. S1(A)). The 2'-OH groups of AmB strongly interacted with the surrounding ergosterol, while the other hydroxy groups (4'-OH) strongly bound to the headgroups of DPhPC in the upper leaflet of the bilayer. In the bottom of AmB, the hydroxy groups (35th-OH, Fig. S1(A)) also associated with the headgroups of DPhPC in the lower leaflet of the bilayer. The radial distribution functions of phosphate groups of DPhPC around the hydroxy groups are shown in Fig. S40. It is seen that the 4'-OH groups of mycosamine are strongly associated with phosphate groups of upper leaflet while interaction between the 35th -OH groups of AmB (which are present in the bottom of AmB channel) and the phosphate group of lower leaflet is less intense. Thus, AmB channel is affixed in the upper leaflet.

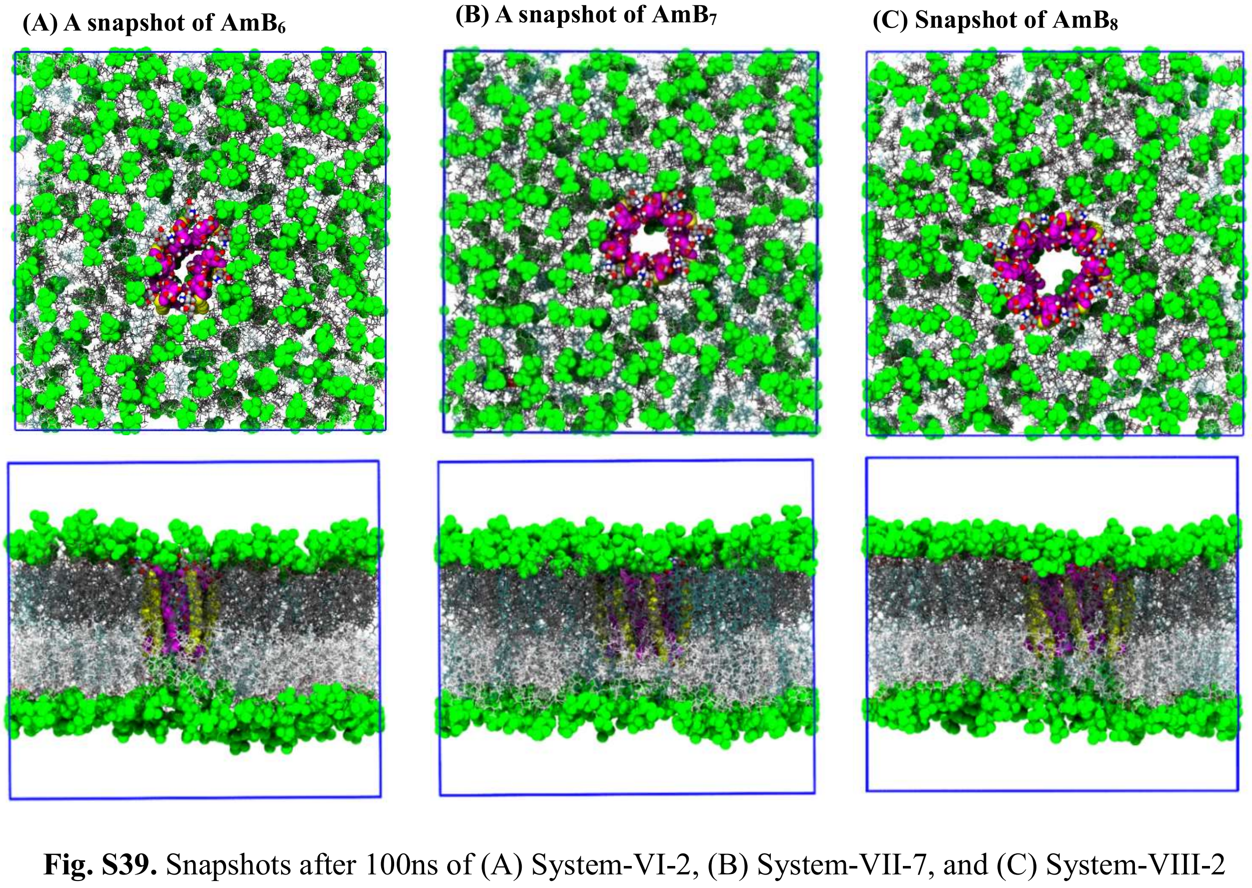
(A) A snapshot of AmB$_6$ **(B) A snapshot of AmB$_7$** **(C) Snapshot of AmB$_8$**

Fig. S39. Snapshots after 100ns of (A) System-VI-2, (B) System-VII-7, and (C) System-VIII-2 in the DPhPC-Erg bilayers. Water is not shown for clarity. The color code of AmB/Erg (Cho) and the presentation are the same as in Fig. S2. The color code of DPhPC is the same as in Fig. S3.

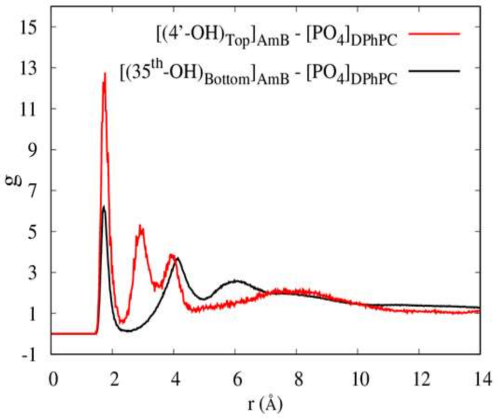

Fig. S40. The radial distribution function of phosphate groups of DPhPC around 4’ -OH group of AmB (red, headgroup) and the 35-OH group (black, tail).

The partial interdigitation of lipid molecules around the AmB channel is one of the important factors for AmB channel stability. We have calculated the distribution of several selected atoms along the bilayer normal obtained from MD simulation, which are shown in Fig. S41. We observed the significant overlapping of the peaks of the acyl-chain terminal signals of the upper and lower leaflets of POPC with each other. This observation indicates the partial interdigitation of the lipid bilayers around the AmB channels, which reduces the energy cost due to the hydrophobic mismatch and this arrangement of lipids stabilizes AmB channel in the bilayers.

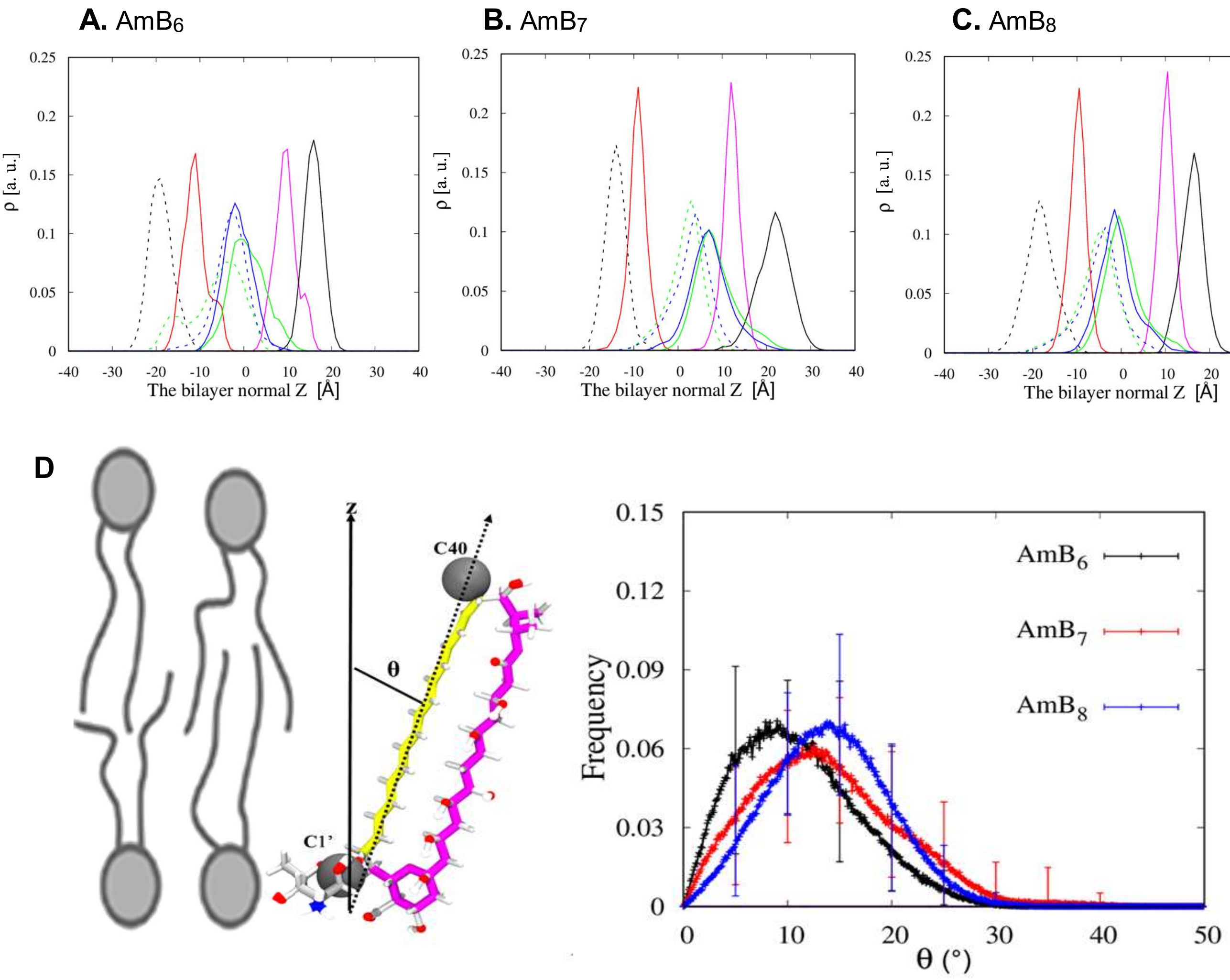

Fig. S41. Probability distribution (ρ) of selected atoms along the bilayer normal calculated from the l μs MD trajectory of the AmB channel in the DPhPC-Erg bilayers. The probability of lipid atoms was calculated for the neighboring lipids within 5 Å of the AmB assembly: black for phosphorus of the DPhPC headgroup, blue for the carbon of a terminal methyl group (*sn-1*), and green for the carbon of a terminal methyl group (*sn-2*). Solid and dashed lines indicate lipids in the upper and lower leaflets, respectively. Red and magenta lines correspond to the C1' and C40 positions of AmB, respectively. (**A**) System-VI-2. (**B**) System-VII-7 and (**C**) System-VIII-2. **(D)** The probability distribution of the tilt angle θ of the AmB molecule embedded in the lipid bilayer; *θ* is defined as the angle between the AmB axis and the bilayer normal. Black; SystemVI-2. Red; SystemVII-7, and Blue: System-VIII-2. The tilt angle (*θ*) is used to describe orientation of the AmB molecule which is defined as the angle between the molecular axis (C1' to C40) of AmB and the bilayer normal. Note that the headgroup (C1') is oriented downward in the bilayer.

Conductance measurements of AmB channels in the mixture of DPhPC and Erg suggest that the AmB_7 channel explains the experimental conductance:

To study the ion channel activity of AmB channels, we have performed 10μs 1MD simulations for each AmB channel with 2M KCl in the presence of applied electric field. (System VI-2, System VII-7, and System VIII-2) We calculated conductance of each AmB channel as given in Tables S8 - S10.

Table S8. Calculated conductance of AmB_6 channel in the DPhPC-Erg bilayer (System-VI-2).

Sample #	AmB_6		
	I [pA]	ΔV [Volt]	G [pS]
S1	0.00	0.25	0.00
S2	0.00	0.17	0.00
S3	0.96	0.12	7.97
S4	0.00	0.17	0.00
S5	0.16	0.14	1.12
S6	0.00	0.24	0.00
S7	0.00	0.21	0.00
S8	0.16	0.118	1.34
S9	0.00	0.193	0.00
S10	0.00	0.17	0.00
Average	0.13 ± 0.02	0.18 ± 0.0	1.04 ± 0.83

Table S9. Calculated conductance of AmB_7 channel in the DPhPC-Erg bilayer (System-VII-7).

Samples	AmB_7		
	I [pA]	ΔV[Volt]	G [pS]
S1	2.88	0.195	14.78
S2	4.64	0.199	23.26
S3	3.84	0.206	18.57
S4	3.36	0.167	20.06
S5	0.00	0.229	0.00
S6	1.12	0.145	7.70
S7	7.20	0.20	35.09
S8	0.64	0.182	3.51
S9	2.40	0.185	12.98
S10	7.52	0.19	39.09
S11	2.88	0.22	13.07
S12	1.12	0.15	7.30
S13	0.00	0.16	0.00
S14	4.16	0.188	22.09
S15	3.04	0.150	20.27
S16	0.16	0.195	0.82
Average	2.8 ± 0.6	0.1850 ± 0.006	14.9 ± 4.8

Table S10. Calculated conductance of AmB_8 channel in the DPhPC-Erg bilayer (System-VIII-2).

Sample #	AmB_8		
	I [pA]	ΔV[Volt]	G [pS]
S1	107.30	0.169	632.97
S2	93.68	0.164	569.76
S3	107.30	0.159	673.59
S4	117.07	0.165	709.38
S5	56.05	0.116	482.62
S6	2.08	0.157	13.2
S7	11.05	0.215	51.31
S8	70.46	0.161	435.89
S9	21.30	0.28	73.89
S10	1.92	0.21	9.00
Average	59 ± 15	0.18 ± 0.01	365 ± 93

The results indicate that ion channel activity of AmB$_6$ is very low. On the contrary, AmB$_8$ is a highly active ion channel. AmB$_7$ has an intermediate activity, showing the average conductance of 14.9 pS. This value is similar to the experimental value of ~14.5 pS. As shown in Table S9, 16 independent MD runs for the System VII-7 give rather large difference in the conductance; indeed, two of 16 MD runs show zero conductance. These channels are supposed to be in a closed state, and the effective pore sizes were indeed smaller than the others. The average pore radius profiles of the AmB$_6$, AmB$_7$, and AmB$_8$ channels are given in Fig. S42. The minimum pore radii for AmB$_6$, AmB$_7$ and AmB$_8$ are $R_{\mathrm{min}} < 2.0$ Å, $R_{\mathrm{min}} > 2.0$ Å, and R_{min} ~4.0 Å, respectively. The required pore radius for hydrated K^+ ions is supposed to be ~2.0 Å to explain the conductance data obtained here. In case of AmB$_8$, the average conductance is 365 pS, which is too high compare to the experimental value. This observation supports that the experimentally obtained AmB channel is most likely a 7-mer complex.

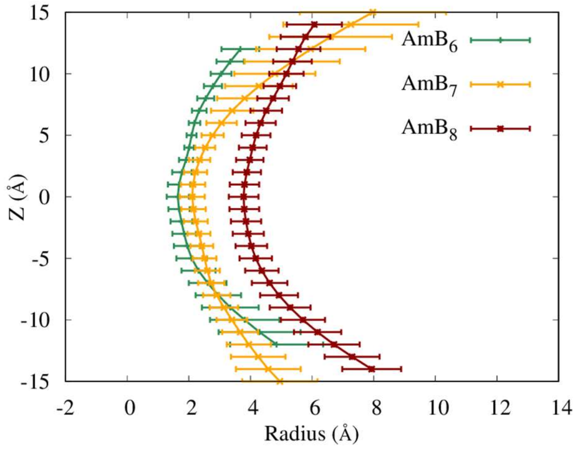

Fig. S42. Pore radius profiles of AmB channels in the DPhPC-Erg bilayers.

Formation of stable dimers of AmB channels in AmB channels aggregation:

We investigated the aggregation behavior of AmB channels in a large POPC bilayer. We first prepared the system with nine AmB_7 channel with the parallel arrangement embedded in the lipid membrane composed of 450 of POPC molecules, which is in consistent with the previous experimental molar ratio (AmB/Erg/POPC, 1: 3: 7) (System-VII-5) (Fig. S43A). We carried out 4-μs MD simulation for the System-VII-5. We also constructed the system with 16 AmB channels with antiparallel arrangement inserted in the lipid membrane composed of 512 POPC and 224 Erg molecules (Fig. S5). We performed 2-μs MD simulation for the System-VII-6.

For system-VII-5, at initial configuration, nine AmB channels are inserted evenly. After 4 μs, we observed the clustering of the AmB channels as shown in Fig. S43A. In the case of system-VII-6, we performed 1μs MD simulations of 4 AmB_7 channels with antiparallel arrangement (Figs. S32A and S32B). We took the final configuration of 4 AmB channels after 1μs and replicated it into *x-y* direction (2x2) and constructed 16 antiparallel AmB channels and generated the initial configuration for system-VII-6 and ran 2μs MD simulations. After 2 μs, we observed stable antiparallel dimers (Fig. S44A).

The clustering of channels was driven by the hydrophobic mismatch between the thin AmB channel and the thicker POPC bilayer. Length of hydrophobic polyene part of AmB is estimated as ~16 Å, based on the crystal structure of *N*-iodoacetyl AmB (*28*), while the length of the hydrophobic core of POPC bilayer is much greater (~25.8 Å) (*83*). To accommodate the thin AmB channel, the surrounding POPCs need to have an interdigitated tails arrangement. We have shown the distribution of selected atoms of AmB and lipid molecules along the bilayer normal in Figs S43C, S44B. The distributions of the acyl-chain terminal signals of the upper (solid lines) and lower leaflets (dotted lines) overlapped with each other. These distributions indicate that membrane thinning is caused by the partial interdigitation of lipid molecules surrounding the AmB channels including those incorporated in the channel aggregates (as illustrated on the right-hand side of Fig. S33).

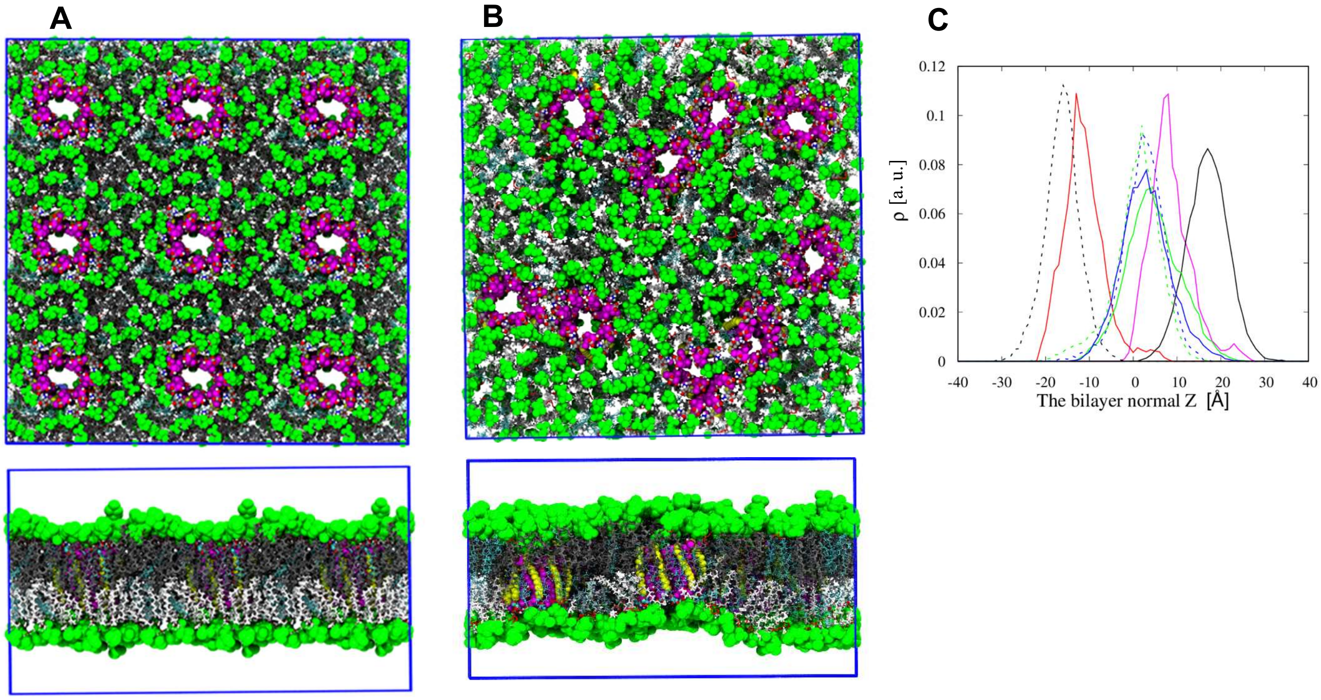

Fig. S43. **A**. The initial arrangement of nine AmB channel assemblies (System VII-5) that were oriented in the same direction (the parallel arrangement) with 450 POPCs, 189 Ergs and 63 AmBs. **B**. The snapshot after 4 μsec revealed that some of the assemblies come close contact to each other; the color code of AmB/Erg and the presentation are the same as in Fig. S2. The color code of POPC is the same as in Fig. S3. **C**. The probability of lipid atoms was calculated for the neighboring lipids within 5 Å of the AmB assembly: black for phosphorus of the POPC headgroup, blue for the carbon of a terminal methyl group (*sn-1*), and green for the carbon of a terminal methyl group (*sn-2*). Solid and dashed lines indicate lipids in the upper and lower leaflets, respectively. Red and magenta lines correspond to the C1' and C40 positions of AmB, respectively. Note that the AmB head group is in a negative position on the *Z* axis parallel to the bilayer normal (see Fig. S41D).

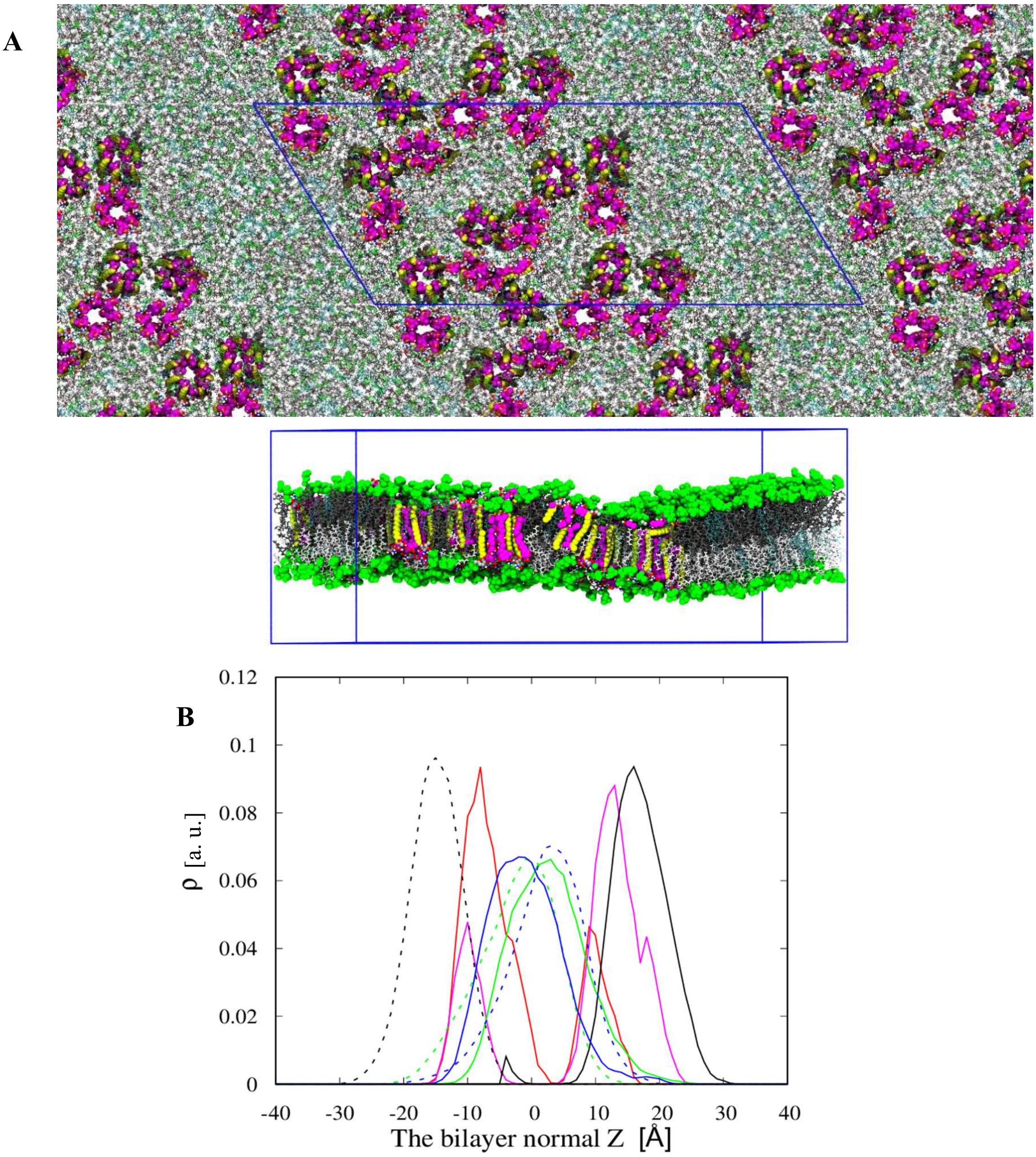

Fig. S44. **A**. The snapshot of the System-VII-6 with the antiparallel arrangement after 2μs MD simulation in the POPC-Erg bilayer; the color code of AmB/Erg and the presentation are the same as in Fig. S2. The color code of POPC is the same as in Fig. S3. **B**. Probability distribution (ρ) of selected atoms along the bilayer normal calculated from the last l μs MD trajectory of the AmB channels (System-VII-6). The probability of lipid atoms was calculated for the neighboring lipids within 5 Å of the AmB assembly: black for phosphorus of the DPhPC headgroup, blue for the carbon of a terminal methyl group (*sn-1*), and green for the carbon of a terminal methyl group (*sn-2*). Solid and dashed lines indicate lipids in the upper and lower leaflets, respectively. Red and magenta lines correspond to the C1’ and C40 positions of AmB, respectively. Note that the AmB head group is in a negative position on the *Z* axis parallel to the bilayer normal (see Fig. S41D).

AME assembly is a stable and active ion channel and N-acetyl-AmB is unstable:

The AmB derivatives can be used to improve the therapeutic index of AmB drugs and with less side effects. In the present work, we have studied the stability and ion channel activity of methyl ester (Fig. S1(B)) (System-VII-3, AME) and *N*-acetyl-derivative (Fig. S1(C)) (system-VII-4, AmB-NHCOCH$_3$) in the POPC-Erg bilayers. The initial structures of these two systems are provided in Fig. S3. We have performed 10 μs all-atom MD simulations for each channel.

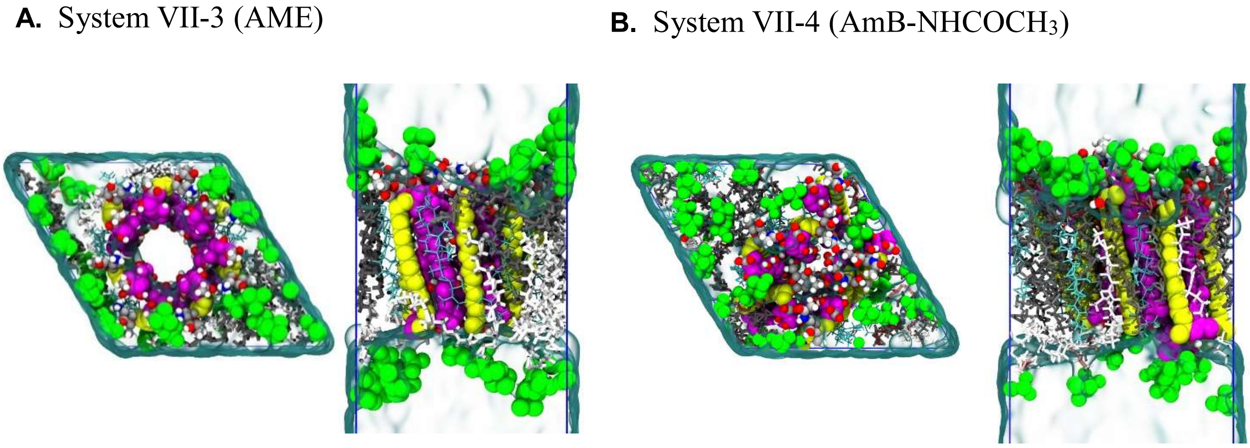
A. System VII-3 (AME)

B. System VII-4 (AmB-NHCOCH$_3$)

Fig. S45. The final configuration from one of the ten 1μs-MD runs of (A) System VII-3 (AME) and (B) System VII-4 (AmB-NHCOCH$_3$) in the POPC-Erg bilayers. The color code of AmB/Erg and the presentation are the same as in Fig. S2. The color code of POPC is the same as in Fig. S3.

The snapshots of the last MD frames of these systems after 1 μs are given in Fig. S45. A stable AME channel was kept, though a significantly distorted structure was observed in the AmB-NHCOCH$_3$ channel. The intermolecular interaction energies between the AmB molecules for AME and AmB-NHCOCH$_3$ channels, respectively, were calculated as given in Table S11. In the case of AmB-CONHCH$_3$ channel, the electrostatic interaction between the aceto-amide group (3'-NHAc) of mycosamine and carboxylate (41^{st}-COO^{-}) group was completely abandoned, while for AME, a strong electrostatic interaction was observed between the two groups. Thus, we ascertained stable AME and unstable AmB-NHCOCH$_3$ ion channels.

Table S11. Coulombic and Lenard-Jones contribution to the interaction energies between ammonium group (3'-NH_3) and carboxylate group (41^{st}-COO^-) of AmB in the POPC-Erg bilayers.

System #	Interaction energies [kJ/mol]		
	3'-NH_3-41^{st}-COO^-		
	Coul	LJ	Total
System-VII-3 (AME)	-33.5	1.9	-33.6 ± 2.4
System-VII-4 (AmB-$NHCOCH_3$)	1.5	-0.2	1.3 ± 0.1

We calculated the conductance of AME channel with 1M-KCl in the presence of applied electric field. The values are provided in the Table S12. The average value of conductance is 3.54 ± 1.0 pS. The low ion channel activity is observed because of the smaller pore radius than that of AmB (Fig. S34(B)).

Table S12. The values of conductance (G) of AME channel in the POPC-Erg bilayers (System-VII-3) in the presence of applied electric field ($E_{\text{applied}} = 0.01$ V/nm).

Sample #	AME channel		
	I [pA]	ΔV [V]	G [pS]
S1	3.20	1.17	2.74
S2	6.88	1.68	4.09
S3	14.57	1.77	8.21
S4	5.12	2.15	2.38
S5	8.16	1.47	5.54
S6	7.37	1.34	5.49
S7	0.16	2.24	0.07
S8	1.12	0.87	1.28
S9	2.08	0.88	2.37
S10	5.60	1.75	3.19
Average	5.43 ± 1.3	1.53 ± 0.15	3.54 ± 1.0

The effect of AmB: Lipid ratio on the stability of AmB channel:

We performed the simulations of AmB$_7$ in 16-POPC (VII-8), 32-POPC (VII-9) and 64-POPC (VII-10) lipid bilayer for ten different initial structures. The distribution of several selected atoms along the bilayer normal obtained from MD simulation are shown in Fig. S46. The probability distribution for the lipid atoms was calculated only for the neighboring lipid molecules within 5 Å of the AmB channel. In all systems, both C$_{40}$ and C$_{41}$ were located near the phosphate group of POPC, while C$_{40}$ was located slightly deeper in the membrane than C$_{41}$. Additionally, the distributions of the acyl-chain terminal signals of the upper and lower leaflets overlapped with each other, indicating membrane thinning because of the interdigitation of lipid molecules and stabilization of the AmB channel in the lipid bilayers. These findings are consistent with the previous report (*26*). However, there was shown to be the difference about the frequency of the interdigitation of lipid molecules among SystemVII-8~10. The peaks of the acyl-chain terminal signals of the upper and lower leaflet molecules was deeper and sharper in the opposite leaflet in SystemVII-10 than SystemVII-8,9, indicating the larger formation of the interdigitation of the lipid molecules in the denser domain of AmB channels. This was driven by the lower energy penalty of the interdigitation by the aggregation of the channels. The larger formation of the interdigitation lead the reduction of the area of the hydrophobic mismatch between AmB channel and the lipid bilayer. The reduction of the area of the hydrophobic mismatch led to reduce the mechanical stress around the AmB channel due to the energy penalty of the hydrophobic mismatch. By the reduction of the mechanical stress, AmB channel was thought to become more stable with less fluctuation in SystemII-3. From these results and discussions, we found the frequency of the interdigitation of lipid molecules was strongly affected by the molar concentration of AmB molecules. In addition, the frequency of the interdigitation resulted in the difference about the channel stability in the different molar ratio (AmB/POPC).

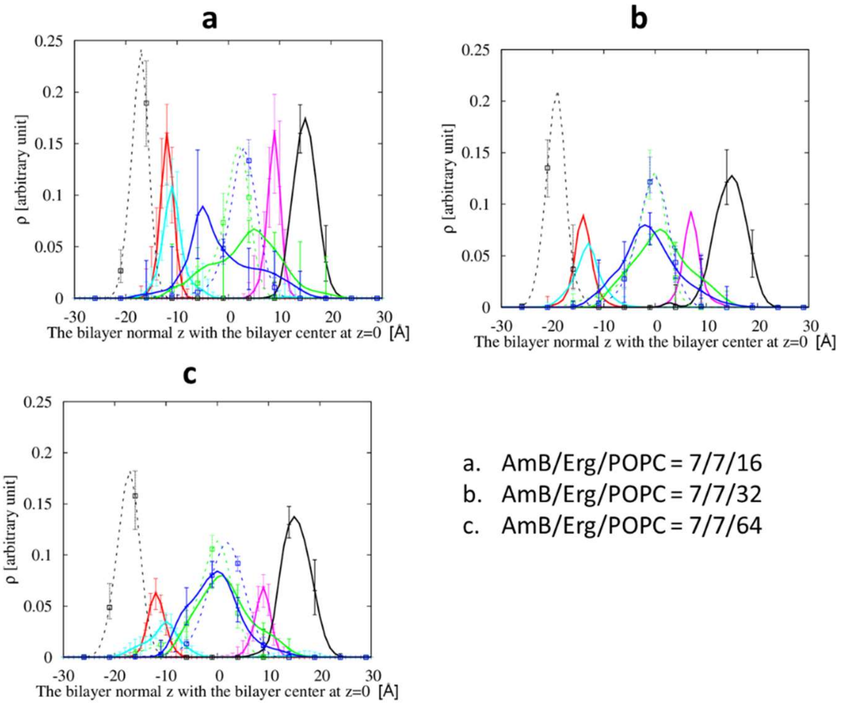

Fig. S46. Probability distribution of selected atoms along the bilayer normal calculated from the last 500 ns MD trajectory of the AmB channel. The probability of lipid atoms was calculated for the neighboring lipids within 5 Å of the AmB assembly: black for phosphorus of the POPC headgroup, blue for the carbon of a terminal methyl group (*sn-1*), and green for the carbon of a terminal methyl group (*sn-2*). Solid and dashed lines indicate lipids in the upper and lower leaflets, respectively. Red and magenta lines correspond to the C_{41} and C_{40} positions of AmB, respectively. Light blue lines correspond to the O_3 position of Erg. (**a**) System VII-8. (**b**) System VII-9. (**c**) System VII-10.

The AmB_8 single assembly is more stable than AmB_8 double length assembly in Erg-POPC lipid bilayer:

We additionally tested the stability of a double-length channel composed of 2x8 AmBs, which may correspond to a standard barrel-stave model (*13*). Our previous MD simulation of a double-length channel composed of 2x7 AmBs showed a significantly lower stability, leading to a collapse of the channel within a simulation time (*26*). Here we repeated a similar examination for 2x8 AmB channel, starting from four different initial configurations. Each initial configuration contains the same structure of 8 AmBs with 8 Erg in a single-length channel system, though copied and rotated to have mycosamine moiety of both 8 mers oriented outward of the membrane. A simulation system is composed of 16:48:112 (1:3:7) AmB:Erg:POPC molecules, hydrated with 8430 water molecules. The constructed channel is embedded in lipid membrane using the CHARMM-GUI (*47-49*). four initial configurations and a final snapshot after 500 ns-MD are given in Fig. S47. As found in the final snapshot, the channel was deformed largely typically within 100 ns. Pore size analysis along the channel is given in Fig. S30B.

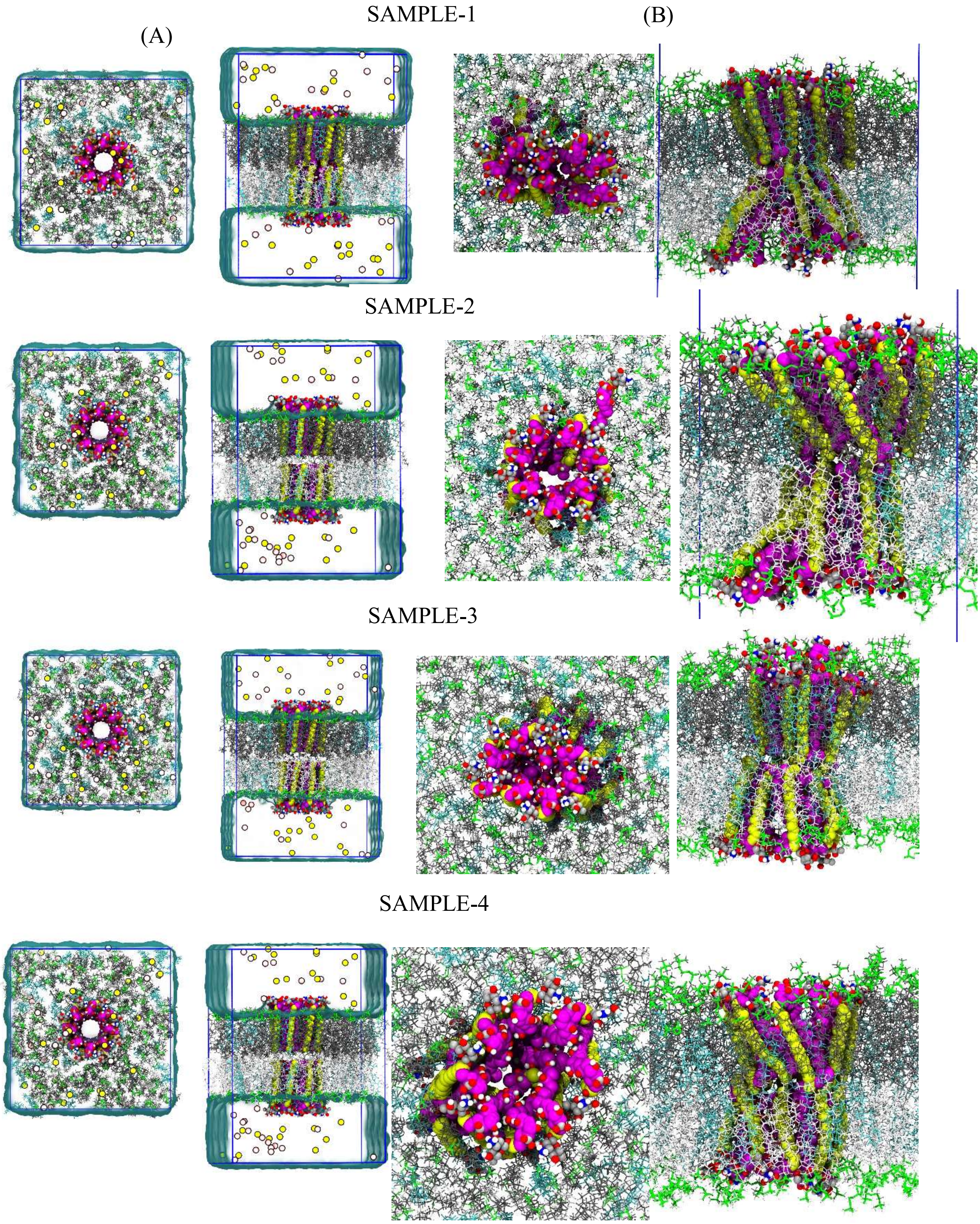

Fig. S47. (A) The initial arrangement of AmB8 double length assembly with 112 POPCs, 48 Ergs and 16 AmBs. Snapshots after 500 ns (B). The color code of AmB/Erg and the presentation are the same as in Fig. S2. The color code of POPC is the same as in Fig. S3. Water is not shown for clarity.

Video description

Videos of the MD simulations of AmB channel. Water molecules and ions that do not penetrate the channel are not shown for clarity.

Video 1: MD simulation of AmB heptamer in DPhPC (side view) under the conditions of VII-7 (Table S2)

Video 2: MD simulation of AmB heptamer in DPhPC (top view) under the conditions of VII-7 (Table S2)

Video 3: MD simulation of AmB hexamer in DPhPC (side view) under the conditions of VI-2 (Table S2)

Video 4: MD simulation of AmB octamer in DPhPC (side view) under the conditions of VIII-2 (Table S2)

Video 5: MD simulation of AmB octamer in DPhPC (top view) under the conditions of VIII-2 (Table S2)

REFERENCES AND NOTES

1. R. Donovick, W. Gold, J. F. Pagano, H. A. Stout, Amphotericins A and B, antifungal antibiotics produced by a streptomycete. I. In vitro studies. *Antibiot. Annu.*, **3**, 579–586 (1956)

2. E. T. Stiller, J. Vandeputte, J. L. Wachtel, Amphotericins A and B, antifungal antibiotics produced by a streptomycete. II. The isolation and properties of the crystalline amphotericins. *Antibiot. Annu.* **3**, 587–591(1956).

3. S. Hartsel, J. Bolard, Amphotericin B: New life for an old drug. *Trends Pharmacol. Sci.* **17**, 445–449 (1996).

4. J. Bolard, How do the polyene macrolide antibiotics affect the cellular membrane properties? *Biochim. Biophys. Acta* **864**, 257–304 (1986).

5. D. Ellis, Amphotericin B: Spectrum and resistance. *J. Antimicrob. Chemother.* **49**, 7–10 (2002).

6. V. Petraitis, R. Petraitiene, J. M. Valdez, V. Pyrgos, M. J. Lizak, B. A. Klaunberg, D. Kalasauskas, A. Basevicius, J. D. Bacher, D. K. Benjamin Jr., W. W. Hope, T. J. Walsh, Amphotericin B penetrates into the central nervous system through focal disruption of the blood-brain barrier in experimental hematogenous *Candida* meningoencephalitis, *Antimicrob. Agents Chemother.* **63**, e01626-19 (2019).

7. W. Luo, M. Hong, Determination of the oligomeric number and intermolecular distances of membrane protein assemblies by anisotropic ^{1}H-driven spin diffusion NMR spectroscopy. *J. Am. Chem. Soc.* **128**, 7242–7251 (2006).

8. G. Gröbner, P. Williamson, Solid-state NMR methods for studying membrane systems, in *Solid-State NMR* (IOP Publising, 2020), pp. 1–30.

9. S. Matsuoka, M. Inoue, Application of REDOR NMR in natural product chemistry. *Chem. Commun.* 5664–5675 (2009).

10. A. Vertut-Croquin, J. Bolard, C. M. Gary-Bobo, Enhancement of amphotericin B selectivity by antibiotic incorporation into gel state vesicles. A circular dichroism and permeability study. *Biochem. Biophys. Res. Commun.* **125**, 360–366 (1984).

11. S. A. Davis, B. M. Vincent, M. M. Endo, L. Whitesell, K. Marchillo, D. R. Andes, S. Lindquist, M. D. Burke, Nontoxic antimicrobials that evade drug resistance. *Nat. Chem. Biol.* **11**, 481–487 (2015).

12. P. Dong, C. Zong, Z. Dagher, J. Hui, J. Li, Y. Zhan, Polarization-sensitive stimulated Raman scattering imaging resolves amphotericin B orientation in *Candida* membrane. *Sci. Adv.* **7**, eabd5230 (2021).

13. B. de Kruijff, R. A. Demel, Polyene antibiotic-sterol interactions in membranes of *Acholeplasma laidlawii* cells and lecithin liposomes. 3. Molecular structure of the polyene antibiotic-cholesterol complexes. *Biochim. Biophys. Acta* **339**, 57–70 (1974).

14. T. Gullion, J. Schaefer, Rotational-echo double-resonance NMR. *J. Magn. Reson.* **81,** 196–200 (1989).

15. J. D. Gehman, F. Separovic, K. Lu, A. K. Mehta, Boltzmann statistics rotational-echo double-resonance analysis, *J. Phys. Chem. B* **111**, 7802–7811 (2007).

16. B. Venegas, J. González-Damián, H. Celis, I. Ortega-Blake, Amphotericin B channels in the bacterial membrane: Role of sterol and temperature. *Biophys. J.* **85**, 2323–2332 (2003).

17. J. Gabrielska, M. Gagoś, J. Gubernator, W. I. Gruszecki, Binding of antibiotic amphotericin B to lipid membranes: A ^{1}H NMR study. *FEBS Lett.* **580**, 2677–2685 (2006).

18. J. Zielińska, M. Wieczor, P. Chodnicki, E. Grela, R. Luchowski, Ł. Nierzwicki, T. Bączek, W. Gruszecki, J. Czub, Self-assembly, stability and conductance of amphotericin B channels: Bridging the gap between structure and function. *Nanoscale* **13**, 3686–3697 (2021).

19. N. Matsumori, Y. Umegawa, T. Oishi, M. Murata, Bioactive fluorinated derivative of amphotericin B. *Bioorg. Med. Chem. Lett.* **15**, 3565–3567 (2005).

20. E. R. deAzevedo, W.-G. Hu, T. J. Bonagamba, K. Schmidt-Rohr, Centerband-only detection of exchange: Efficient analysis of dynamics in solids by NMR. *J. Am. Chem. Soc.* **121**, 8411–8412 (1999).

21. R. Mani, S. D. Cady, M. Tang, A. J. Waring, R. I. Lehrer, M. Hong, Membrane-dependent oligomeric structure and pore formation of a β-hairpin antimicrobial peptide in lipid bilayers from solid-state NMR. *Proc. Natl. Acad. Sci. U.S.A.* **103**, 16242–16247 (2006).

22. C. M. McNamara, S. Box, J. M. Crawforth, B. S. Hickman, T. J. Norwood, B. J. Rawlings, Biosynthesis of amphotericin B. *J. Chem. Soc. Perkin Trans. 1* **1998**, 83–87 (1998).

23. Y. Nakagawa, Y. Umegawa, N. Matsushita, T. Yamamoto, H. Tsuchikawa, S. Hanashima, T. Oishi, N. Matsumori, M. Murata, The structure of the bimolecular complex between amphotericin B and ergosterol in membranes is stabilized by face-to-face van der Waals interaction with their rigid cyclic cores. *Biochemistry* **55**, 3392–3402 (2016).

24. T. M. Anderson, M. C. Clay, A. G. Cioffi, K. A. Diaz, G. S. Hisao, M. D. Tuttle, A. J. Nieuwkoop, G. Comellas, N. Maryum, S. Wang, B. E. Uno, E. L. Wildeman, T. Gonen, C.

M. Rienstra, M. D. Burke, Amphotericin forms an extramembranous and fungicidal sterol sponge. *Nat. Chem. Biol.* **10**, 400–406 (2014).

25. A. Lewandowska, C. P. Soutar, A. I. Greenwood, E. Nimerovsky, A. M. De Lio, J. T. Holler, G. S. Hisao, A. Khandelwal, J. Zhang, A. M. SantaMaria, C. D. Schwieters, T. V. Pogorelov, M. D. Burke, C. M. Rienstra, Fungicidal amphotericin B sponges are assemblies of staggered asymmetric homodimers encasing large void volumes. *Nat. Struc. Mol. Biol.* **28**, 972–981 (2021).
26. T. Yamamoto, Y. Umegawa, H. Tsuchikawa, S. Hanashima, N. Matsumori, K. Funahashi, S. Seo, W. Shinoda, M. Murata, The Amphotericin B-ergosterol complex spans a lipid bilayer as a single-length assembly. *Biochemistry* **58**, 5188–5196 (2019).
27. T. Yamamoto, Y. Umegawa, M. Yamagami, T. Suzuki, H. Tsuchikawa, S. Hanashima, N. Matsumori, M. Murata, The perpendicular orientation of amphotericin B methyl ester in hydrated lipid bilayers supports the barrel-stave model. *Biochemistry* **58**, 2282–2291 (2019).
28. K. N. Jarzembska, D. Kamiński, A. A. Hoser, M. Malińska, B. Senczyna, K. Woźniak, M. Gagoś, Controlled crystallization, structure, and molecular properties of iodoacetylamphotericin B. *Cryst. Growth Des.* **12**, 2336–2345 (2012).
29. N. Matsumori, Y. Sawada, M. Murata, Mycosamine orientation of amphotericin B controlling interaction with ergosterol: Sterol-dependent activity of conformation-restricted derivatives with an amino-carbonyl bridge. *J. Am. Chem. Soc.* **127**, 10667–10675 (2005).
30. R. A. Brutyan, P. McPhie, On the one-sided action of amphotericin B on lipid bilayer membranes. *J. Gen. Phisiol.* **107**, 69–78 (1996).
31. S. Matsuoka, M. Murata, Membrane permeabilizing activity of amphotericin B is affected by chain length of phosphatidylcholine added as minor constituent. *Biochim. Biophys. Acta* **1617,** 109–115 (2003)..
32. P. Van Hoogevest, B. De Kruijff, Effect of amphotericin B on cholesterol-containing liposomes of egg phosphatidylcholine and didocosenoyl phosphatidylcholine. A refinement of the model for the formation of pores by amphotericin B in membranes. *Biochim. Biophys. Acta* **511**, 397–407 (1978).
33. M. E. Kleinberg, A. Finkelstain, Single-length and double-length channels formed by nystatin in lipid bilayer membranes. *J. Membr. Biol.* **80**, 257–269 (1984).
34. T. Ruckwardt, A. Scott, J. Scott, P. Mikulecky, S. C. Hartsel, Lipid and stress dependence of amphotericin B ion selective channels in sterol free membranes, *Biochim. Biophys. Acta* **1372**, 283–288 (1998).

35. C. A. Hitchcock, K. J. Barrett-Bee, N. J. Russell, The lipid composition of azole-sensitive and azole-resistant strains of *Candida albicans*. *J. Gen. Microbiol.* **132**, 2421–2431 (1986).

36. G. Fujii, J. E. Chang, T. Coley, B. Steere, The formation of amphotericin B ion channels in lipid bilayers. *Biochemistry* **36**, 4959–4968 (1997).

37. A. Vertut-Croquin, J. Bolard, M. Chabbert, C. Gary-Bobo, Differences in the interaction of the polyene antibiotic amphotericin B with cholesterol- or ergosterol-containing phospholipid vesicles. A circular dichroism and permeability study. *Biochemistry* **22**, 2939–2944 (1983).

38. H. W. Huang, Molecular mechanism of antimicrobial peptides: The origin of cooperativity. *Biochim. Biophys. Acta* **1758**, 1292–1302 (2006).

39. Y. Hong, P. J. Shaw, B. N. Tattam, C. E. Nath, J. W. Earl, K. R. Stephen, A. J. McLachlan, Plasma protein distribution and its impact on pharmacokinetics of liposomal amphotericin B in paediatric patients with malignant diseases. *Eur. J. Clin. Pharmacol.* **63**, 165–172 (2007).

40. J. Bolard, P. Legrand, F. Heitz, B. Cybulska, One-sided action of amphotericin B on cholesterol-containing membranes is determined by its self-association in the medium. *Biochemistry* **30,** 5707–5715 (1991).

41. H. M. Walker-Caprioglio, J. M. MacKenzie, L. W. Parks, Antibodies to nystatin demonstrate polyene sterol specificity and allow immunolabeling of sterols in *Saccharomyces cerevisiae*. *Antimicrob. Agents Chemother.* **33**, 2092–2095 (1989).

42. M. Chéron, B. Cybulska, J. Mazerski, J. Grzybowska, A. CzerwiŃski, E. Borowski, Quantitative structure-activity relationships in amphotericin B derivatives. *Biochem. Pharmacol.* **37**, 827–836 (1988).

43. S. C. Hartsel, S. K. Benz, W. Ayenew, J. Bolard, Na^+, K^+ and Cl^- selectivity of the permeability pathways induced through sterol-containing membrane vesicles by amphotericin B and other polyene antibiotics. *Eur. Biophys. J.* **23**, 125–132 (1994).

44. K. T. Mueller, Analytic solution for the time evolution of dipolar-dephasing NMR signals. *J. Magn. Reason. Ser. A* **A113**, 81–93 (1995).

45. Y. Umegawa, N. Matsumori, T. Oishi, M. Murata, Ergosterol increases the intermolecular distance of amphotericin B in the membrane-bound assembly as evidenced by solid-state NMR. *Biochemistry* **47,** 13463–13469 (2008).

46. Y. Umegawa, Y. Nakagawa, K. Tahara, H. Tsuchikawa, N. Matsumori, T. Oishi, M. Murata, Head-to-tail interaction between amphotericin B and ergosterol occurs in hydrated phospholipid membrane. *Biochemistry* **51,** 83–89 (2012).

47. S. Jo, J. B. Lim, J. B. Klauda, W. Im, CHARMM-GUI membrane builder for mixed bilayers and its application to yeast membranes. *Biophys. J.* **97,** 50–58 (2009).

48. E. L. Wu, X. Cheng, S. Jo, H. Rui, K. C. Song, E. M. Dávila-Contreras, Y. Qi, J. Lee, V. Monje-Galvan, R. M. Venable, J. B. Klauda, W. Im, CHARMM-GUI membrane builder toward realistic biological membrane simulations. *J. Comput. Chem.* **35,** 1997–2004 (2014).

49. J. Lee, X. Cheng, J. M. Swails, M. S. Yeom, P. K. Eastman, J. A. Lemkul, S. Wei, J. Buckner, J. C. Jeong, Y. Qi, S. Jo, V. S. Pande, D. A. Case, C. L. Brooks, III, A. D. MacKerell, Jr., J. B. Klauda, W. Im, CHARMM-GUI input generator for NAMD, GROMACS, AMBER, OpenMM, and CHARMM/OpenMM simulations using the CHARMM36 additive force field. *J. Chem. Theory Comput.***12,** 405–413 (2016).

50. S. Jo, T. Kim, V. G. Iyer, W. Im, CHARMM-GUI: A web-based graphical user interface for CHARMM. *J. Comput. Chem.* **29,** 1859–1865 (2008).

51. M. J. Abraham, T. Murtola, R. Schulz, S. Páll, J. C. Smith, B. Hess, E. Lindah, Gromacs: High performance molecular simulations through multi-level parallelism from laptops to supercomputers. *SoftwareX* **1–2**, 19–25 (2015).

52. J. B. Klauda, R. M. Venable, J. A. Freites, J. W. O'Connor, D. J. Tobias, C. Mondragon-Ramirez, I. Vorobyov, A. D. MacKerell, R. W. Pastor, Update of the CHARMM all-atom additive force field for lipids: Validation on six lipid types. *J. Phys. Chem.* **114,** 7830–7843 (2010).

53. J. B. Lim, B. Rogaski, J. B. Klauda, Update of the cholesterol force field parameters in CHARMM. *J. Phys. Chem.* **116,** 203–210 (2012).

54. K. Vanommeslaeghe, E. Hatcher, C. Acharya, S. Kundu,S. Zhong, J. Shim, E. Darian, O. Guvench, P. Lopes, I. Vorobyov, A. D. MacKerell Jr., CHARMM general force field: A force field for drug-like molecules compatible with the CHARMM all-atom additive biological force fields. *J. Comput. Chem.* **31,** 671–690 (2010).

55. K. Vanommeslaeghe, A. D. MacKerell Jr., Automation of the CHARMM general force field (CGenFF) I: Bond perception and atom typing. *J. Chem. Inf. Model.* **52,** 3144–3154 (2012).

56. K. Vanommeslaeghe, E. Prabhu Raman, A. D. MacKerell Jr., Automation of the CHARMM general force field (CGenFF)II: Assignment of bonded parameters and partial atomic charges. *J. Chem. Inf. Model.* **52,** 3155–3168 (2012).

57. I. Soteras Gutiérrez, F. Y. Lin, K. Vanommeslaeghe, J. A. Lemkul, K. A. Armacost, C. L. Brooks III, A. D. MacKerell Jr., Parametrization of halogen bonds in the CHARMM general force field: Improved treatment of ligand–protein interactions. *Bioorg. Med. Chem.* **24,** 4812–4825 (2016).

58. W. L. Jorgensen, J. Chandrasekhar, J. D. Madura, R. W. Impey, M. L. Klein, Comparison of simple potential functions for simulating liquid water. *J. Chem. Phys.***79,** 926–935 (1983).

59. S. Nosé, A unified formulation of the constant temperature molecular dynamics methods. *J. Chem. Phys.* **81,** 511–519(1984).

60. W. G. Hoover, Canonical dynamics: Equilibrium phase-space distributions. *Phys. Rev.* **31,** 1695–1697 (1985).

61. M. Parrinello, A. Rahman, Polymorphic transitions in single crystals: A new molecular dynamics method. *J. Appl. Phys.***52,** 7182–7190 (1981).

62. U. Essmann, L. Perera, M. L. Berkowitz, T. Darden, H. Lee, L. G. Pedersen, A smooth particle mesh Ewald method. *J. Chem. Phys.***103,** 8577–8593 (1995).

63. T. Darden, D. York, L. Pedersen, Particle mesh Ewald: An $N\cdot\log(N)$ method for Ewald sums in large systems. *J. Chem. Phys.* **98,** 10089–10092 (1993).

64. B. Hess, H. Bekker, H. J. C. Berendsen, J. G. E. M. Fraaije, LINCS: A linear constraint solver for molecular simulations. *J. Comput. Chem.***18,** 1463–1472 (1997).

65. B. Roux, The membrane potential and its representation by a constant electric field in computer simulations. *Biophys. J.* **95,** 4205–4216 (2008).

66. O. S. Smart, J. G. Neduvelil, X. Wang, B. A. Wallace,M. S. P. Sansom, HOLE: A program for the analysis of the pore dimensions of ion channel structural models. *J. Mol. Graph.***14,** 354–360 (1996).

67. H. Rui, K. I. Lee, R. W. Pastor, W. Im, Molecular dynamics studies of ion permeation in VDAC. *Biophys. J.* **100,** 602–610(2011).

68. D. P. Tieleman, The molecular basis of electroporation. *BMC Biochem.* **5,** 1–12 (2004).

69. R. A. Böckmann, B. L. De Groot, S. Kakorin, E. Neumann, H. Grubmüller, Kinetics, statistics, and energetics of lipid membrane electroporation studied by molecular dynamics simulations. *Biophys. J.* **95,** 1837–1850 (2008).

70. S. Dasa, R. K. Goswami, Total synthesis of marine natural products separacenes A and B. *Org. Biomol. Chem.* **15,** 4842–4850 (2017).

71. L. A. Paquette, D. Pissarnitski, L. Barriault, A modular enantioselective approach to construction of the macrolactone core of polycavernoside A. *J. Org. Chem.* **63,** 7389–7398 (1998).

72. M. Hervé, B. Cybulska, C. M. Gary-Bobo, Cation permeability induced by valinomycin, gramicidin D and amphotericin B in large lipidic unilamellar vesicles studied by ^{31}P-NMR. *Eur. Biophys. J.* **12,** 121–128 (1985).

73. M. Baginski, H. Resat, E. Borowski, Comparative molecular dynamics simulations of amphotericin B–cholesterol/ergosterol membrane channels. *Biochim. Biophys. Acta Biomembr.***1567,** 63–78 (2002).

74. T. Katsu, T. Imamura, K. Komagoe, K. Masuda, T. Mizushima, Simultaneous measurements of K^+ and calcein release from liposomes and the determination of pore size formed in a membrane. *Anal. Sci.* **23,** 517–522 (2007).

75. T. Houdai, S. Matsuoka, N. Matsumori, M. Murata, Membrane-permeabilizing activities of amphidinol 3, polyene-polyhydroxy antifungal from a marine dinoflagellate. *Biochim. Biophys. Acta Biomembr.* **1667,** 91–100 (2004).

76. Y. Nakagawa, Y. Umegawa, K. Nonomura, N. Matsushita, T. Takano, H. Tsuchikawa, S. Hanashima, T. Oishi, N. Matsumori, M. Murata, Axial hydrogen at C7 position and bumpy tetracyclic core markedly reduce sterol's affinity to amphotericin B in membrane. *Biochemistry* **54,** 303–312 (2015).

77. C. Ernst, J. Grange, H. Rinnert, G. Dupont, J. Lematre, Structure of amphotericin B aggregates as revealed by UV and CD spectroscopies. *Biopolymers* **20,** 1575–1588 (1981).

78. J. Milhaud, M. A. Hartmann, J. Bolard, Interaction of the polyene antibiotic amphotericin B with model membranes: Differences between small and large unilamellar vesicles. *Biochimie* **71,** 49–56 (1989).

79. S. Matsuoka, H. Ikeuchi, N. Matsumori, M. Murata, Dominant formation of a single-length channel by amphotericin B in dimyristoylphosphatidylcholine membrane evidenced by ^{13}C-^{31}P rotational echo double resonance. *Biochemistry* **44,** 704–710 (2005).

80. R. Mouri, K. Konoki, N. Matsumori, T. Oishi, M. Murata, Complex formation of amphotericin B in sterol-containing membranes as evidenced by surface plasmon resonance. *Biochemistry* **47,** 7807–7815 (2008).

81. N. Shvinka, G. Caffier, Cation conductance and efflux induced by polyene antibiotics in the membrane of skeletal muscle fiber. *Biophys. J.* **67,** 143–152 (1994).

82. B. Mariusz, J. Mazerski, Molecular modelling of amphotericin B–ergosterol primary complex in water. *Biophys. Chem.* **95**, 125–133 (2002).

83. F. A. Nezil, M. Bloom, Combined influence of cholesterol and synthetic amphiphillic peptides upon bilayer thickness in model membranes. *Biophys. J.* **61,** 1176–1183 (1992)